Chemistry and Fundamental Electron Correlation in Chemically Prepared Lanthanide Nanoparticles

Dissertation
zur Erlangung des Doktorgrades
des Department Physik
der Universität Hamburg

vorgelegt von
Edlira Suljoti
aus Vlora, Albania

Hamburg 2008

Gutachter der Dissertation:	Prof. Dr. Wilfried Wurth
	Prof. Dr. Michael Rübhausen
Gutachter der Disputation:	Prof. Dr. Wilfried Wurth
	Prof. Dr. Günter Huber
Datum der Disputation:	19.12.2008
Vorsitzender des Prüfungsausschusses:	PD Dr. Michael Martins
Vorsitzender des Promotionsausschusses:	Prof. Dr. Joachim Bartels
Dekan der MIN Fakultät:	Prof. Dr. Arno Frühwald

Chemistry and fundamental electron correlation in chemically prepared lanthanide nanoparticles

Abstract

X-ray spectroscopy is a fascinating area of modern physics research that can probe the most basic and fundamental physical questions while addressing issues related to modern technology and specifically the materials which enable this technology. From the other side, nanoscience is a fundamentally exciting and technologically relevant area of research due to the remarkable changes in fundamental electrical, optical and magnetic properties of matter that occur on the nanometer scale. In this thesis X-ray spectroscopy is the method used to determine the electronic and geometric structure of chemically prepared lanthanide orthophosphate nanoparticles.

The local electronic structure and the chemical state of each lanthanide ion within the host nanoparticle is determined with near edge X-ray absorption spectroscopy. Besides, chemical bonding within the phosphate group, its evolution through the lanthanide series, and its interplay with crystal phase and cluster morphology is systematically investigated. A missing local order in the crystal structure accompanied with multiple ion sites in the smaller $\sim$ 2nm nanoparticles was revealed.

In addition, thin film preparation of nanoparticles allowed us to investigate atomic fundamental aspects of lanthanide ions. Thus, many body aspects of the strong electron-electron interaction at the $4d$ thresholds of the lanthanides are investigated with resonant inelastic X-ray scattering spectroscopy. The combined experimental and theoretical studies showed that the strong correlated physical states alter the spectral distribution of oscillator strength giving rise to interference effects and concomitant asymmetrical spectral profiles. Breaking of coherence in some of the radiative decay channels governed by dipole transition is the reason for the different lineshapes observed in fluorescence yield compared to electronic yield.

Chemistry and fundamental electron correlation in chemically prepared lanthanide nanoparticles

Kurzfassung

Spektroskopie mit Röntgenstrahlung ist ein faszinierendes Gebiet der modernen physikalischen Forschung, das sowohl die elementaren und fundamentalen physikalischen Fragestellungen als auch Sachverhalte der modernen Technologie betreffen kann, speziell die dafür notwendigen Materialien. Auf der anderen Seite ist die Nanowissenschaft wegen der grundlegend anderen elektronischen, optischen und magnetischen Eigenschaften von Materie auf der Nanometerskala ein hochinteressantes und technologisch relevantes Forschungsgebiet. In dieser Dissertation wird daher Röntgenspektroskopie als eine Methode benutzt, die elektronische und geometrische Struktur von chemisch präparierten Lanthanidorthophosphat-Nanoteilchen zu bestimmen.

Die lokale elektronische Struktur und der chemische Zustand jedes Lanthanidions in seinem jeweiligen Nanoteilchen wird mit Röntgen Nahkanten Absorptionsspektroskopie (Near Edge X-Ray Absorption Spectroscopy) bestimmt. Dabei werden die chemischen Bindungen innerhalb der Phosphatgruppe, deren Entwicklung durch die Gruppe der Lanthanide und ihre Wechselwirkungen mit der kristallinen Phase und der Clustermorphologie systematisch untersucht. Es wurde eine fehlende lokale Ordnung in der Kristallstruktur aufgedeckt, die mit mehreren möglichen Gitterplätzen der Ionen im kleinen Nanoteilchen einhergeht.

Zusätzlich erlaubte uns die Präparation von dünnen Filmen aus Nanoteilchen, fundamentale atomare Eigenschaften von Lanthanidionen zu untersuchen. Vielteilcheneffekte der starken Elektron-Elektron-Wechselwirkung an den 4d-Kanten der Lanthanide wurden mit resonanter inelastischer Röntgenstreuungsspektroskopie (Resonant Inelastic X-Ray Scattering Spectroscopy) untersucht. Die Kombination von experimentellen und theoretischen Studien zeigte, dass die stark korrelierten physikalischen Zustände die spektrale Verteilung der Oszillatorstärke ändern, so dass Interferenzeffekte und damit einhergehende asymmetrische spektrale Profile auftreten. Die Aufhebung der Kohärenz in einigen der strahlenden Zerfallskanälen, die von Dipolstrahlung bestimmt werden, ist der Grund füür die verschiedenen beobachteten Linienformen bei Fluoreszenz- und Elektronendetektion.

Contents

Abstract 1

1 Introduction **5**

2 Soft X-ray spectroscopy probing atomic core levels **9**

2.1 X-ray photoelectron spectroscopy 10

2.2 X-ray absorption spectroscopy 11

2.3 Auger electron and X-ray emission spectroscopies 12

2.4 X-ray resonant scattering 14

2.5 Experimental aspects 17

3 Computational methods **25**

3.1 Hartree-Fock method 25

3.2 Theoretical aspects of X-ray absorption 31

3.3 Resonant X-ray scattering formalism 42

4 Geometric and electronic structure of lanthanide orthophosphate nanoparticles determined with X-rays **47**

4.1 Introduction 48

4.2 Experiment 50

4.3 Long-range order in the crystallites 53

4.4 Local structural geometry of the crystallites 58

4.5 Conclusions 67

5 Physical states correlation and their influence on the spectral shapes of La **69**

5.1 Experimental 71

5.2 La $N_{4,5}$-edge electron and fluorescence yield 71

5.3 Nonradiative decay processes of the $^3D_1$ and $^3P_1$ resonances . . . 75

5.4 Radiative decay processes of the $^3D_1$ and $^3P_1$ resonances 78

5.5 Conclusion 90

6 Trends in lanthanide systems: from simple to complex 93

6.1 Light Lanthanides 94

6.2 Heavy Lanthanides 99

7 Conclusion and Outlook 109

Comments on my contribution 112

Acknowledgments 113

List of papers 115

Bibliography 117

Chapter 1

Introduction

A subject of fundamental importance in atomic physics is the study of how electronic properties are modified by the atomic environment, as in molecules or in the solid state. At the frontier between atomic physics, molecular physics and the physics of condensed matter new systems have been found to explore this frontier. Thus clusters, containing a small or large numbers of molecules, are new systems whose properties evolve from the free atom limit to that of a solid as a function of size. Nanoscience is devoted to study and understand the changes in fundamental properties of these materials in terms of cluster-size effects, cluster-surface effects and structure effects.

Semiconductor clusters represent a class of heavily studied nanoparticles. In these systems the quantum confinement of free electrons arising as a result of small cluster size is associated with an increase of the band gap between the conduction and valence bands. Thus, the optical transitions across the band gap can be tuned within the visible range as a function of cluster size. This property has made these systems fundamentally interesting and technologically relevant area of research.

Besides the semiconductor clusters, lanthanide insulator clusters are also quite interesting systems. They have optical transitions in the infrared, visible, and ultraviolet spectrum due to the *f to f* forbidden transitions that occur within the insulator band gap. In addition, they display very high lattice energies and high resistance against oxidation and photo corrosion. All these properties make them attractive for industrial interest as useful components in light-emitting diodes (LEDs), displays, optoelectronic devices and as long-lived dyes for biological labeling. Lanthanide clusters are also of academic interest because they provide the rare opportunity to systematically investigate how the synthesis and the properties of a nanomaterial are affected by the ionic radius of its metal ion. In addition,

these systems do not manifest size-effects because of their large band gaps, but they do show surface-effects and structure effects as a function of size and metal ion. These aspects address for a systematic and detailed study of the geometric and electronic structure of the lanthanide series of nanoparticles.

In order to deal with monodisperse nanoparticles of narrow size and shape distribution as well as good crystallinity and solubility, colloidal chemistry is used as a method of particle synthesization. The size and shape of the nanoparticles were deduced by a variety of methods; Transmission Electron Microscopy (TEM), Scanning Electron Microscopy (SEM), Dynamic Light Scattering (DLS) and X-Ray Diffraction (XRD). In addition, the crystal structure of the nanoparticles was determined via X-ray powder diffraction.

The method of choice to investigate these systems was not in solution. Very thin films of nanoparticles consisting of less than one monolayer were prepared on cleaned, surface polished and passivated silicon substrates. Thin film preparation made possible the simultaneous use of different spectroscopic methods, like electron and fluorescence yield, to investigate fundamental electronic properties of lanthanide clusters. Besides, thin film preparation overwhelmed the difficulties on electron yield measurements because of charging effects inherent to wide band gap insulators.

The common approach to investigate the electronic structure of the nanoparticles is the use of X-ray spectroscopic methods. Thus, element specific information is available from resonant X-ray excitation which allows to create excited states at selected atomic centers and to even gain selectivity to the local chemical environment of an atom. The high brilliance and tunability of synchrotron radiation sources facilitates these investigations. In this framework, the local electronic structure and the chemical state of each lanthanide ion in its host nanoparticle was determined with near edge X-ray absorption spectroscopy (NEXAFS) measured at the $M_{4,5}$-edge of lanthanides. Chemical bonding within the phosphate group, its evolution through the lanthanide series, and its interplay with the crystal phase and crystal dimension was studied by oxygen K-edge NEXAFS.

Rare earth ions consist a class of highly correlated electron materials. They are characterized by localized unoccupied valence states that are fully screened from the outer filled $5p$ and $6s$ shells. This makes it possible to investigate fundamental atomic aspects of lanthanide ions despite the fact that they are embedded in nanocrystals. An ideal technique to study electron correlation in lanthanides was chosen resonant inelastic X-ray scattering (RIXS) because it provides an additional level of the transition selectivity due to element specificity

and dipole selection rule. In a model system of lanthanum we have investigated physical state correlations on the core excited intermediate states and ionic final states and their influence on the spectral profiles. Theoretical calculations are used to elucidate the different aspects of electron correlations.

Thus, this thesis has the following structure: Chapter 2 gives the general framework and briefly summarizes the field of X-ray spectroscopy as a probe of atom specific electronic structure. The purpose here is to address in a coherent manner all aspects relevant to the work presented in the following chapters without fully reviewing this vast field. Chapter 3 gives some basic theoretical aspects of X-ray absorption and resonant scattering as well as the models used in this work to calculate the measured XAS and RIXS cross sections in lanthanides. The original work is presented in Chapters 4, 5 and 6, where each chapter is either published in a peer review journal or in manuscript form. The focus of chapter 4 lies in the characterization of nanoparticles and in the investigations of electronic structure as a function of surface-effects (high surface to volume ratio). In Chapter 5 the electron correlation effects due to the physical state symmetry mixing and to the large lifetime broadening of the giant resonance are thoroughly investigated in the simple system model of lanthanum case. Chapter 6 consists of an overview of RIXS experimental data measured at different lanthanides. Correlation trend within the series is evoked in the framework of La model.

Chapter 2

Soft X-ray spectroscopy probing atomic core levels

Spectroscopy is defined as the study of interaction between light (photons) and matter. This interaction often results in the release of an energy carrier, for instance, a photon, an electron or an ion. Detection of any of these particles provides the basics of many modern spectroscopic techniques, such as diffraction, resonant and non-resonant scattering, photoelectron and Auger spectroscopy. Some of these techniques have been developed that utilize not only the original visible (VIS) light, but many other forms of radiation: infrared (IR), ultraviolet (UV), vacuum ultraviolet (VUV), X-rays and hard X-rays. They differ from each other due to the kind of excitation that they produce: IR radiation produces rotational-vibrational excitations, UV/VIS light produces valence band excitations where an electron is promoted from the valence band to an empty state in the conduction band as depicted in Fig. 2.1 (a). Whereas, X-rays produce core level excitations where an electron from a core state is excited to an empty state, depicted in Fig. 2.1 (b) and (c). The spatial localization of core levels to one specific atom leads to the essential feature of all core level spectroscopies: probing "local" or "atom specific" properties in polyatomic systems.

Core level spectroscopies can be distinguished into spectroscopies that involve the excitation of the core electrons such as X-ray photoionization and X-ray absorption and the ones that monitor the decay of core hole states such as Auger, X-ray emission and resonant X-ray scattering. In this chapter I will give an overview of the core level spectroscopies used in my studies and the experimental aspects of these techniques.

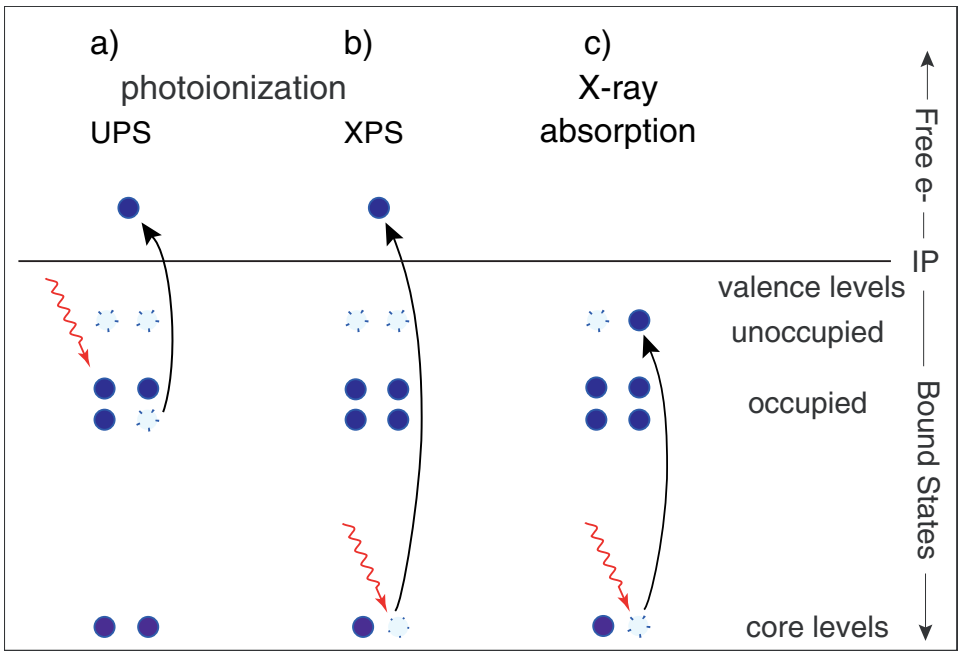

Figure 2.1: Photoionization of valence (a) and core (b) electrons to unbound final states leading the atom to an ionized final state. In the X-ray absorption (c) the electron is excited to a resonant bound state and the final state is a neutral core excited state.

2.1 X-ray photoelectron spectroscopy

In the X-ray photoemission process (Fig. 2.1-b) an electron is excited out into the continuum. To remove the electron from the atom, the photon energy has to be well above the core ionization threshold or Ionization Potential (IP). Thus, the kinetic energy of the outgoing photoelectron is related to the incoming photon energy $h\nu$ and the sample work function Φ by

$$E_B = h\nu - E_{Kin} - \Phi \tag{2.1}$$

Here, the binding energy E_B reflects the energy of the electronic state from which the electron has been ejected with respect to the Fermi level [1].

Within the sudden approximation [2], the electron binding energy is equal to the electron orbital energy (Koopman's theorem), where all the other orbitals are frozen during the core ionization process. Because each chemical element has a specific electronic configuration that is accompanied with a specific pattern of core level binding energies, it is the fundamental property of X-ray photoemission

spectroscopy (XPS) to identify the chemical elements in a molecule or a solid [3]. In addition, the detailed core level position of the excited electron depends on the chemical state and local coordination of the probed atoms (chemical shifts[4]) thus, XPS is used to probe local chemical states of individual atoms embedded in molecules, nanoparticles, bulk and interfaces. Here, the chemical shift in the core-level binding energy is used as a local element-specific probe, reflecting the different chemical environments surrounding the photoionized atom. Therefore, XPS is also termed as electron spectroscopy for chemical analysis (ESCA) [5–7] Besides, XPS is sensitive to the charge transfer effects within atoms in a molecule, caused by the presence of the core hole potential, and thus, it is used to investigate the final state molecular hybridization of molecules and solids [8].

2.2 X-ray absorption spectroscopy

X-Ray absorption spectroscopy (XAS) provides a method to study the electronic properties and the local atomic structure of the materials. Due to the core-hole localization, X-Ray absorption process (Fig. 2.1-c) as a function of photon energy is a measure of the "atom specific" unoccupied states.

X-ray absorption spectroscopy is referred to as NEXAFS (near edge X-ray absorption fine structure) or as XANES (X-ray absorption near edge structure) for photon energies close to the core-ionization threshold up to 50 eV above the edge, and as EXAFS (extended X-ray absorption fine structure) for photon energies far from the threshold; starting from 50 eV up to 1000 eV above the absorption edge.

NEXAFS method probes the excitation of core electrons to unoccupied valence states, and thus it provides a direct information about the nature of the empty molecular orbitals. Because NEXAFS is a charge conserving process (the electron does not leave the atom), it is accompanied with small modifications of the molecular hybridization, and hence it probes, at a good approximation, the ground state unoccupied density of states in molecules and solids. This is different from the XPS spectra, where the presence of core hole will modify the hybridization state. In addition, NEXAFS spectra are used as "fingerprints" for identifying different molecular species within a solid because the empty molecular orbitals and their energy positions are characteristic for different classes of chemical species. Besides, NEXAFS spectra can provide information about the local symmetry of the molecules in its ground state because it involves transitions from well defined initial and final states governed by the dipole selection rule.

Differently from NEXAFS, EXAFS is based on the fact that the absorption coefficient above a core edge shows a slowly oscillating behavior. These oscillations are due to scattering of the excited electron by the neighboring atoms in the lattice. Thus, the pattern is sensitive to the detailed distribution of nearest neighbors, in terms of distances to the probed atom, to the coordination numbers and fluctuations in bond distances. In this way EXAFS is a useful probe of the local atomic structure of materials, i.e., of the short-range-order in molecules and solids.

In this work, I am focused on NEXAFS technique investigating the fine structure close to the absorption edge of different core thresholds and some theoretical aspects of this method will be discussed in chapter 3.

2.3 Auger electron and X-ray emission spectroscopies

The core ionized state in Fig. 2.2-a is far from energy equilibrium. Its energy is usually much larger than that of any state involving valence vacancies. This energy difference between the core ionized state and the valence hole states is the driving force for the decay of the core hole, which has typically an average lifetime of a few femtoseconds. Thus, the core ionized state will decay via two processes, non-radiative (Fig.2.2-b) and radiative (Fig. 2.2-c) decays. In the non-radiative decay, the energy released by filling the core hole with a valence electron is carried away by an electron and the process is known as Auger decay [9]. In the radiative decay instead, a photon is emitted and the process is known as X-ray emission. The analysis of the emitted electrons or photons is the basis of Auger electron spectroscopy (AES) or X-ray emission spectroscopy (XES). The Auger decay has a two-hole (2h) final state and the Auger electron is found at fixed kinetic energies, because the core-ionized state has a fixed energy independent from the photon energy [1]. The radiative decay has a one-hole (1h) final state, and the emitted photon has also fixed energy. The obtained valence electron information, in both AES and XES, corresponds to a projection of the valence electron structure on the core hole site. This implies that both methods can probe atom specific valence states without overlapping contribution from the other atoms in the system. The advantage of XES toward AES is that the radiative decay is governed by dipole

[1]The photon energy in excess of the energy needed to create the core hole is carried away from the photoelectron.

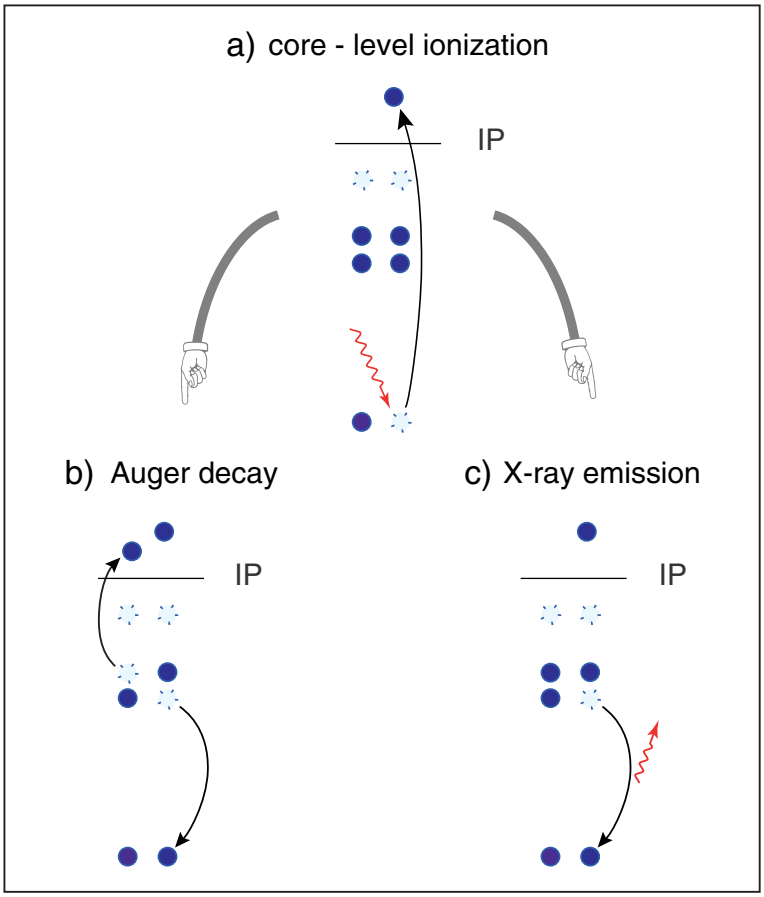

Figure 2.2: Schematic of radiative and nonradiative decay channels following the photoionization process. The nonradiative decay reaches a (2h) final state and is called Auger decay. The radiative decay reaches (1h) final state and is called X-ray emission.

selection rule and thus XES is sensitive to the various final state symmetries in the valence region. This implies that the core hole projects out local components of the occupied valence states in the same way as in XAS.

The Auger process dominates for the light elements and shallow core levels, whereas for heavier elements and for deeper core holes, the decay is instead dominated by the radiative X-ray emission channel. In the soft X-ray energy region, the radiative decay is generally very low, typically about 0.1 percent of the total core hole decay rate. Because of the large escape depth of the photons, XES is normally considered as bulk sensitive technique compared to the surface sensitive - AES. The method may, however, be surface sensitive by impinging the photons on the sample at grazing incidence.

2.4 X-ray resonant scattering

When a core electron is photoexcited resonantly to near threshold bound states, the system remains charge neutral within the core hole lifetime. [2] The intermediate core excited states can fragment to a variety of final states through radiative and nonradiative transitions. Projection onto a specific final state is dictated by the intermediate core excited states. Hence, both radiative and nonradiative decays of the near threshold excitations are coherent second order processes where excitation and deexcitation processes are coherently correlated by the second-order quantum formula, the so called Kramers-Heisenberg formalism. Both processes are refereed to as resonant X-ray scattering (RXS) processes. Since the intermediate states of resonant scattering processes are the same final states of the first order optical process XAS, the information obtained from RXS is greater than XAS. Thus, RXS is a potential spectroscopic technique that provides us with information about both X-ray absorption and emission processes and their correlation.

Both radiative and nonradiative scattering processes can be distinguished in spectator or participator type, by the presence or not of the initially excited electron in the final RXS state. Both type of processes are depicted in Fig. 2.3.

In the nonradiative scattering, guided by the Coulomb interaction, one electron makes a transition to fill the core hole, and a second electron, which takes up the excess energy, is ejected. The first decay channel is characterized by the involvement of the excited electron and leaves the system with a single valence vacancy and a charge of +1, known as the participator channel. The final state is energetically the equivalent of valence PES, but the core-hole-assisted path generally has a much larger cross section at the resonant threshold. For this reason this decay channel is often refereed to as resonant PES (RPES) or participator autoionization spectroscopy. In the second decay channel, also shown in Fig. 2.3 (b), the electron remains in the normally unoccupied levels in the final state, and two valence electrons are removed in an Auger-like transition. This channel, often refereed to as resonant Auger or spectator autoionization, also leaves the system in a +1 charge state, but is a valence excited state (reminiscent of shakeup in PES), i.e., a two-hole one-electron (2h, 1e) final state.

The participator radiative decay of the core excited state is termed resonant elastic X-ray scattering (REXS) and brings the scatterer into the electronic

[2] The core hole lifetimes range from a few femtoseconds down to the timescale of electronic transitions themselves.

ground state. Whereas, the radiative spectator decay of the core excited state is termed resonant inelastic X-ray scattering (RIXS) process and leaves the scatterer to valence excited one-hole one-electron (1h, 1e) final states.

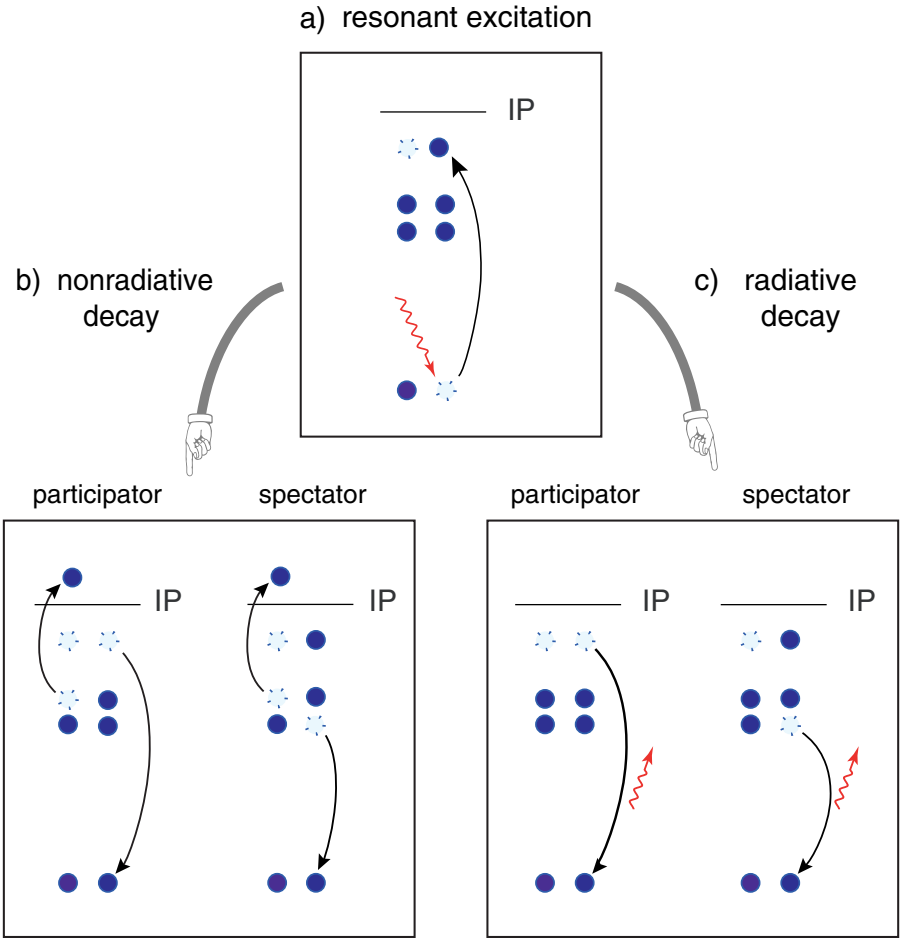

Figure 2.3: Schematic of radiative and nonradiative decay channels upon resonant core excitation. The nonradiative scattering b) reaches in the participator channel a valence hole final state, and in the spectator channel a two hole valence excited (2h, 1e) final state. The radiative scattering c) reaches in the participator channel as the final state the electronic ground state, and in the spectator channel a valence excited (1h, 1e) final state.

The resonant X-ray scattering process is very sensitive to the valence environment and the resonant threshold studies are a very useful probe of the local screening environment and of the localized final states [10]. Contrary to the nonradiative RXS, the radiative RXS process is governed by electromagnetic type

of interaction; the dipole operator, and the symmetry selection will act by strict rules. Thus, RIXS provides a local probe of the valence states, in which the dipole selection rule governing the process provides a means to extract information about the partial atomic density of states. In addition, the low energy electronic excitations probed by RIXS can be of particular importance in electron correlated materials such as $3d$ transition metals [11] and rare earths [12] because they can have great consequences in terms of the electronic and/or magnetic properties of these materials. Whereas, symmetry selection in nonradiative RXS is ineffective because of the Coulomb interaction, and their spectral profiles consist of many overlapping lines which makes the interpretation of the spectra difficult. On the other hand, the cross section of nonradiative RXS in the soft X-ray energy range is considerably larger than the radiative RXS cross section, since the Coulomb interaction, responsible for the Auger decay, is stronger than the electromagnetic interaction.

The theory used to describe radiative and nonradiative decays upon the core threshold excitation is known as scattering formalism, and will be briefly reviewed in section 3.3.

2.5 Experimental aspects

Experimental physics crucially depends on the quality and sophistication of the experimental setup used. Thus, I will focus here in the general experimental aspects and requirements. The specific experimental setup and sample geometry is described in detail in connection with the corresponding studies.

2.5.1 Experimental Setup

The presented experiments require an intense X-ray photon flux concentrated in a small spot size. The reason is that the fluorescence yield of shallow core holes is very low, and in addition we detect the emitted photon light in a small solid angle. Furthermore, we require narrow bandwidth excitation below the natural lifetime broadening of the investigated core excited states. Thus, the high brilliance synchrotron radiation facilities as BESSY II and Hasylab were used.

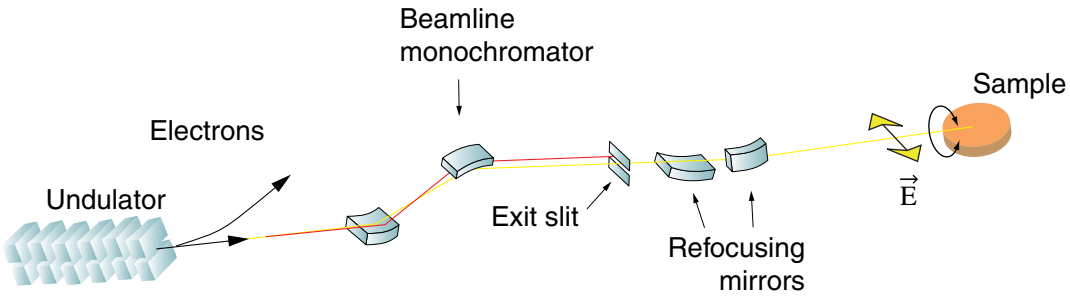

Figure 2.4: Schematic drawing of a beamline

The schematic picture of a typical beamline used in our experiments is shown in Fig. 2.4. It consists of an undulator insertion device, where the bunched electron beam is moving on a periodic trajectory matching the periodic magnetic field of the undulator. The radiation emitted from the accelerated electrons from each undulator-bend is superposed coherently [3] giving sharp maxima, that are the undulator harmonics. Intensity of 'odd' harmonics is observed on the optical axis of the undulator, whereas the 'even' harmonics radiate off-axis. The energy

[3] In an undulator the distance between the magnets is such that the light emitted when an electron passes one magnet is in phase with the light emitted when it passes all the other magnets.

of these maxima in the undulator spectrum is determined by the strength of the magnetic field in the undulator; in practice this is done by changing the gap between the two arrays of magnets.

The undulator radiation is dispersed in a plane grating monochromator and the monochromatic radiation ($\frac{E}{\Delta E} \leq 8000$) is focused horizontally and vertically by (usually) the gold coated mirrors into the sample. The typical beam spot size at the sample is less than $100x100\ \mu m^2$, depending on exit slit width. During spectroscopic measurements, the photon flux is simultaneously monitored through the photo-current (I_0), measured either on the surface of the last refocusing mirror or on a metallic grid inserted behind the refocusing optics. The I_0 is used to normalize experimental spectra for intensity variations in the photon source.

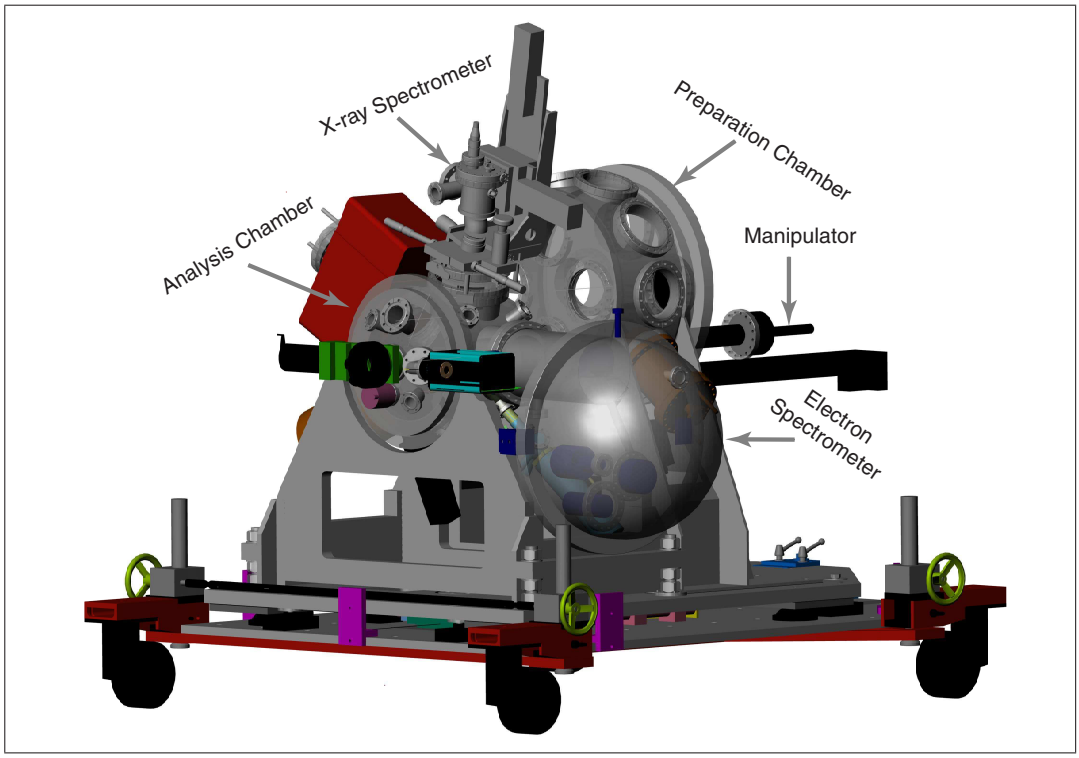

Figure 2.5: Hamburg Inelastic X-Ray scattering Station (HIXSS)

All the experiments have been performed in our transportable ultra high vacuum (UHV) experimental station called Hamburg Inelastic X-ray Scattering Station (HIXSS). It consists of two UHV chambers with a base pressure of $5x10^{-11}$ mbar. The preparation chamber contains equipment for sample preparation and characterization: an ion-sputter gun, gas inlet system, evaporators, a mass spectrometer and a LEED (low energy electron diffraction) system. In addition, a

load lock sample exchange system at a base pressure 1x10^{-8} mbar is connected to the preparation chamber. It was designed and constructed exclusively for the nanoparticle's project, with my substantial contribution, to keep the nanoparticles in a good vacuum before transferring into the UHV station.

The analysis chamber houses an electron analyzer (Scienta SES 2002), a grazing incidence X-ray spectrometer, a home built partial electron yield detector, and an electron- as well as a X-ray-gun for routine sample characterization in laboratory conditions. The electron and X-ray spectrometers are confocal, with their optical axis perpendicular to the incoming photon beam, which impinges onto the sample surface in grazing incidence at $7 \pm 2°$. In addition, a manipulator that is connected to the preparation chamber, holds and moves the samples along both chambers. Both the sample manipulator and the analysis chamber are rotatable independently around the optical axis of the incoming beam. This allow us to vary the orientation of the polarization vector onto the sample surface, as well as to vary the detection angle in the electron and X-ray analyzers.

The Scienta SES 2002 electron spectrometer consists of a hemispherical analyzer and an accelerating-retarding multielement electrostatic lenses, that allows to operate the analyzer at constant pass energies (E_p) between 1 and 500 eV.

The XES spectrometer is used in all the fluorescence and RIXS experiments described in this thesis. It consists of the slit assembly, three spherical gratings and the detector. The slit, grating and the detector are positioned in a Rowland circle, i.e., a circle with a diameter that is the same as the grating radius. The so called Rowland geometry, depicted in Fig. 2.6, insures that the image of the slit is focused on the detector surface. The entrance slit is continuously variable from 0 μm to 100 μm. The three gratings are mounted at fixed angles of grazing incidence and are gold coated to increase the overall reflectivity. They have different groove densities of 1200 $\frac{l}{mm}$, 400 $\frac{l}{mm}$ and 300 $\frac{l}{mm}$, and cover a total energy range of about 50 eV to 1000 eV. The detector consist of a two dimensional multichannel plates, where the first plate is cesium iodide coated in order to increase the converting efficiency of photons into electrons. In the following multichannel plates the electrons are highly amplified into an electron cascade. They are back converted to photons in a fluorescent screen and detected by a CCD (charge-coupled device) camera.

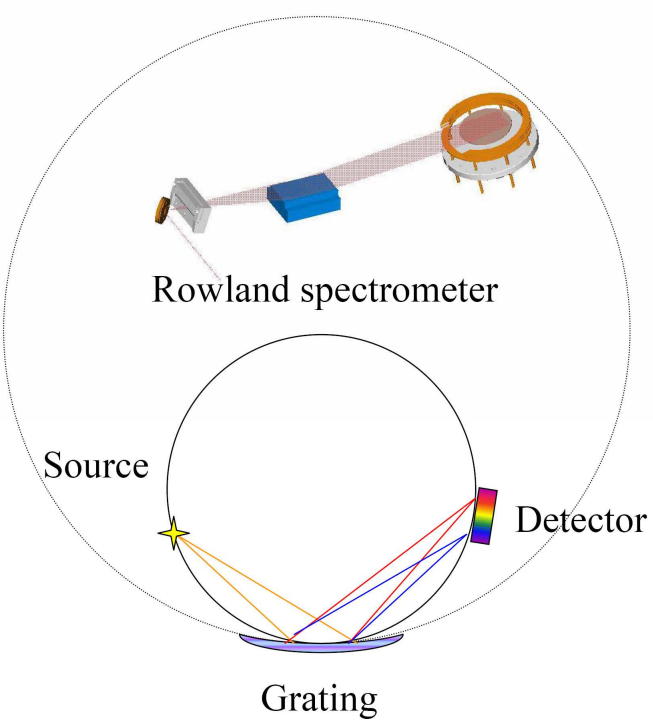

Figure 2.6: The soft X-ray spectrometer and the Rowland geometry. The radiation from a point like source on the Rowland circle is diffracted by the grating and is focussed on the detector placed as well on the circle.

2.5.2 XAS measurements

The measurement of XAS is nowadays a routine experiment for electronic structure characterization. The review article of J. Kawai [13] highlights different techniques used to measure XAS,: X-ray excited optical luminescence (XEOL), X-ray fluorescence, X-ray transmission, total reflection XAS, total electron yield TEY and secondary yield methods (Auger electron yield, the ion yield method).

In our experiments, we have measured the photoabsorption spectrum by scanning the incident photon energy monitoring the TEY by recording the electron current flowing in the sample. Although, our samples were insulators, we could record very nice TEY spectra owing to the very thin monolayer of insulator nanoparticles spin coated in Silicon wafers. In addition, we monitored simultaneously the Auger electron yield and the total fluorescence yield (TFY). The first one was recorded in our Scienta spectrometer, monitoring the Auger processes of the resonant threshold at a fixed energy window. The later one was recorded in the XES spectrometer, monitoring the zero order emitted light.

2.5.3 Synthesis of the nanoparticles

The whole series of Lanthanide orthophosphate nanoparticles is chemically prepared in a liquid-phase synthesis [14–16] in high-boiling coordinating solvents. The particles are capped by organic ligands which are responsible for their high colloidal solubility and low tendency to form agglomerates. In the following the synthesis procedure is described.

Precursors:

3.74 gr Metallic salt ($LnCl_3x7H_2O$)

10 ml Methanol (CH_3OH)

10.9 ml (40 mmol) Tributilphosphate is the complex builder ($[C_4H_9]_3PO_4$)

30 ml Diphenyl ether is the high-boiling solvent ($C_6H_5OC_6H_5$)

13.5 ml (40 mmol) Trihexylamin is the capping ligand ($[C_6H_{13}]_3N$)

6.57 ml (14 mmol) Phosphoric acid is the anion source (H_3PO_4)

Lanthanides are highly reactive metals that can be found only in crystalline compounds. Thus, as a source for Ln^{3+} ions is taken $LnCl_3x7H_2O$ metallic salt. Because all the precursors of the synthesis (the complex builder, the high boiling solvent and the surfactants) are non-polar solutions, methanol is added in order to dissolve the salt in anions and cations (La^{3+}; Cl^-; OH^-; H^+). The solution is stirred in a magnetic stirrer until the salt is dissolved completely and a clear solution is formed. Then, the Tributylphosphate is added to the solution, which is used as a stabilizer, a complex builder and as a phosphate source. The solution is set in an rotary evaporator and is heated up to 40° C and is continuously pumped from 200 mbar till 120 mbar. This process assures that the evaporated methanol is pumped out of the solution. When methanol is completely removed, the solution is taken out of the evaporator. Diphenyl ether is used as "high boiling solvent" in the reaction that does not allow the evaporation process to take place during the reaction. Diphenyl ether is a solid crystal (frozen) at room temperature and it is warmed up until it liquifies and then is added to the solution.

The solution is put in a reaction vessel, depicted in Fig. 2.7 and is heated up till 50° C and is continuously pumped up in order to remove the rest of methanol that may be still present in the solution. Then, the solution is heated up slowly till 105° C in order to degas the water from the solution. (The water comes from the metallic salt that was the chlorine hydrate.) During the heating process water bubbles are formed which are pumped up with the oil pump. During the pumping

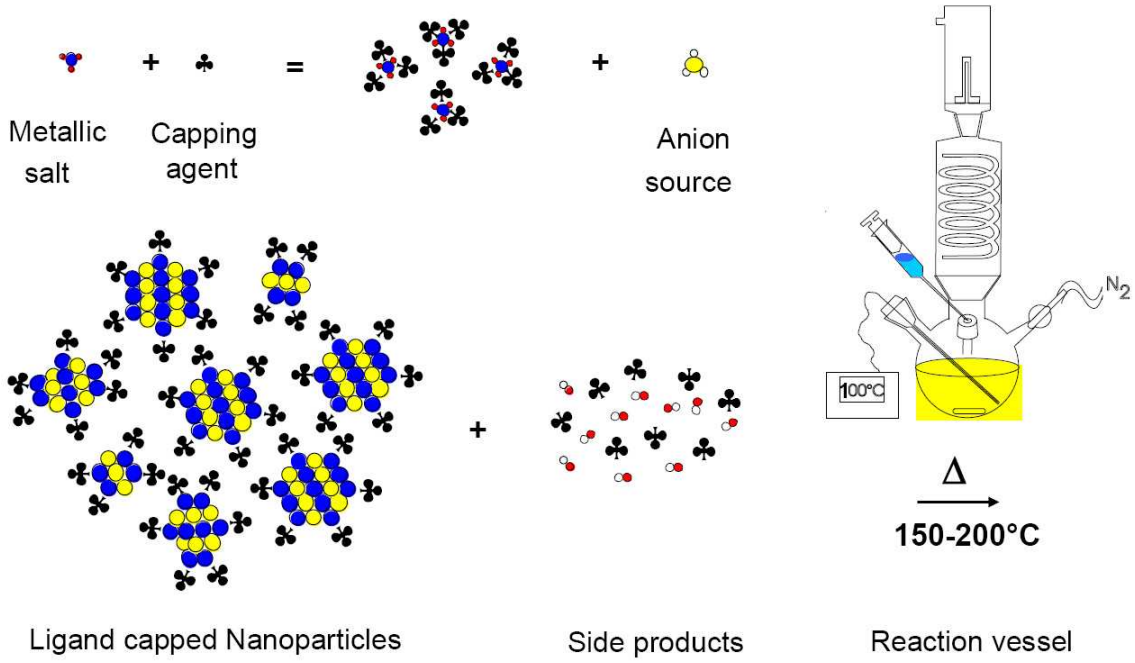

Figure 2.7: Schematic of the chemical synthesis of Lanthanide nanoparticles

process the temperature of the solution it falls down. Then, the pumping process is stopped till the solution is heated up and bubbles are formed again. Then the solution is pumped up again. The procedure is repeated till no more bubbles are formed. Then, the solution is cooled down at a temperature of 50° C. The ligand source (trihexylamine) is added to the reaction vessel and right away the phosphate source (phosphoric acid). At this point the solution is floated with a noble gas (argon or nitrogen N_2) which prohibits the formation of carbon dioxide (CO_2) which kills the reaction. Here is repeated again the pumping and bubbling process till no more bubbles are created.

The solution is heated up to 200° C under argon atmosphere. Thus, the chemical reaction and nanoparticle formation starts. After 2 h, heating was stopped and the reaction mixture was allowed to cool. Clear colloids of lanthanide phosphate nanoparticles were obtained. The precipitates were washed out with methanol and the nanoparticles were size selected in a diafiltration cell equipped with a 5000-Da filter (millipore). After repeating this procedure five times, the nanoparticles were isolated from the purified colloid by removing the methanol with a rotary evaporator.

2.5.4 Sample preparation

The lanthanide nanoparticles were dissolved in methanol solutions at 0.25% and 1% weight concentrations and then spin-coated on silicon wafers. The substrates were mirror-polished silicon single crystals of (100) orientation, of 12mm^2 size and 525μm thickness. They were of p-type (doped with Boron) with a resistivity of $\sim$5Ωcm. Prior to the spin-coating procedure a surface cleaning and passivation procedure was applied to the silicon wafers.

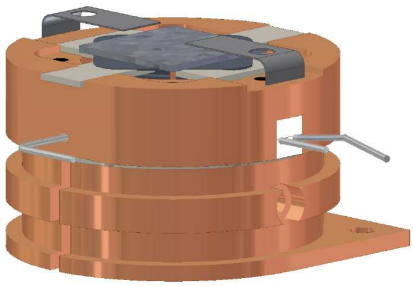

Figure 2.8: The sample holder and the silicon wafer clipped with tantalum wires.

The silicon substrates were cleaned ultrasonically in acetone, in isopropanol and then in deionized water for 10 minutes, respectively. Afterwards, they were chemical etched in solution of 10% hydrofluoric acids (HF) : 50% ethanol : 40% water for 10 min, a recipe given by [17]. The chemical HF etching of silicon wafers removes the surface oxide and terminates the silicon surface with atomic hydrogen. The hydrogen termination retards the silicon surface oxidation and protect the surface from chemical attack. In order to remove the physisorbed chemicals on the surface such as SiF_4, NH_4OH, HF and other molecules, the wafers were rinsed briefly with deionized water [18] subsequently after the chemical etching. Ultimately, a drop of lanthanide phosphate-solution was spin-coated on the cleaned and hydrogen-passivated surface for 1 sec at 1000 rpm, 11 sec at 4000 rpm and 19 sec at 8000 rpm. The samples were clipped on the sample holder with tantalum wires and were mounted on the transfer arm of the load lock system where they were pumped down to 1x10^{-8} mbar. Later they were transferred to the sample manipulator and were brought to the analysis chamber.

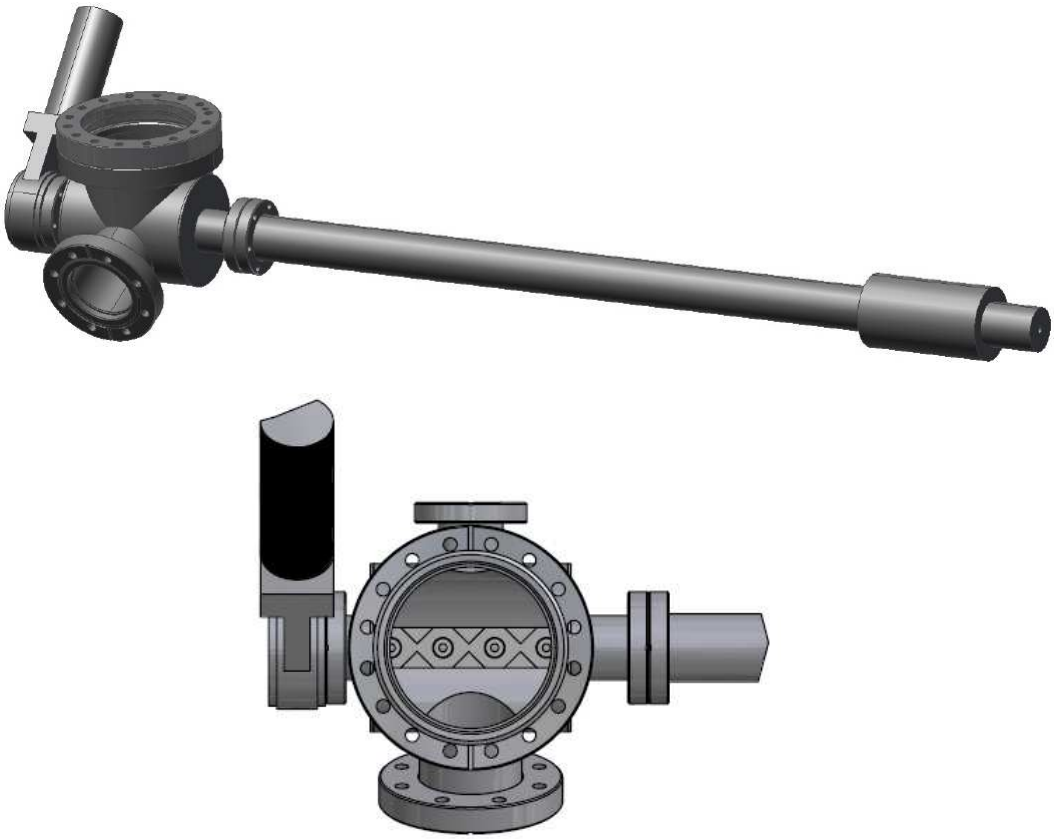

Figure 2.9: The load lock sample exchange system constructed for a easy transfer of the samples into the UHV chamber.

Chapter 3

Computational methods

Throughout this thesis we will deal with the problems of calculating the energy of the ground state configuration, excited state configurations, X-ray absorption transition cross section and the X-ray resonant Raman scattering cross section. In this framework, some of the basic aspects of X-ray absorption and resonant scattering theory will be here introduced. Within the studies of this work, the electronic structure calculation of lanthanide ions based on Hartree-Fock (self consistent field method) is employed. These calculations are based on solving the time-independent Schrödinger equation for the atomic Hamiltonian using the Cowan's atomic code [19]. Thus, a short introduction of the Hartree-Fock approximation will be given.

3.1 Hartree-Fock method

3.1.1 Born-Oppenheimer approximation

The vibrational motion of a nucleus in an atom is relatively slow in comparison to the surrounding electrons due to the very large difference in mass. This means that the electrons respond very quickly to any perturbation of the atomic system, whereas the nucleus remain virtually fixed (stationary) on the time scale of electron motion. This provides the basis for a separation between the electronic and nuclear degrees of freedom in the co-called Born-Oppenheimer approximation. Thus, the total wavefunction (ψ_{tot}) of an atom containing N electrons and a nucleus can be separated into a product of an electronic (ψ_e) and nuclear (ψ_n) part

$$\psi_{tot} = \psi_e \cdot \psi_n \tag{3.1}$$

3.1.2 Atomic Hamiltonian

Within the Born-Oppenheimer approximation, the Hamiltonian of an atom containing N electrons is given by summing the one-electron Hamiltonian over all N electrons, and adding a term for the electrostatic Coulomb electron-electron interaction ($H_{elec-elec}$). In units of Bohr radius and Rydberg energies the Hamiltonian is,

$$H = H_{kin} + H_{elec-nucl} + H_{s-o} + H_{elec-elec}$$

$$= -\sum_i \nabla_i^2 - \sum_i \frac{2Z}{r_i} + \sum_i \xi_i(r_i)(l_i \cdot s_i) + \sum_{i>j} \sum \frac{2}{r_{ij}} \tag{3.2}$$

H_{s-o} is the spin-orbit interaction term of each electron obtained by a consideration of relativistic Dirac's correction to the non-relativistic Hamiltonian, $r_i = |r_i|$ is the distance of the i^{th} electron from the nucleus, $r_{ij} = |r_i - r_j|$ is the distance between the i^{th} and j^{th} electrons, and the summation $i > j$ is over all pairs of electrons. Thus, we need to solve the Schrödinger equation,

$$H\psi^k = E^k\psi^k \tag{3.3}$$

in order to obtain the energy E^k and the wavefunction ψ^k of the atom for every quantum state k.

3.1.3 Central field approximation

To produce a solvable Schrödinger equation the Hartree-Fock method uses the central-field approach, in which it approximates the potential energy of the electrons in the atom to the energy of their average interaction. Thus, in the central-field model is assumed that any given electron i moves independently of the other $(N-1)$ electrons in the electrostatic (assumed stationary) field of the nucleus and the other electrons. The electrostatic field of the electrons is assumed to be time-averaged over the motion of $(N-1)$ electrons, and therefore is considered to be spherically symmetric. This leads to a set of one-electron equations, called the Hartree-Fock equations

$$[-\nabla_i^2 + V_i(r_i)]\varphi_i(r_i) = \varepsilon_i \varphi_i(r_i) \tag{3.4}$$

where $V_i(r_i)$ is the average potential energy due to the interaction of one electron with all the other electrons and the nuclei in the molecule. In this central field, the probability distribution of electron i it is described by a one-electron wavefunction:

$$\varphi_i(r_i) = \frac{1}{r} P_{n_i l_i j_i}(r_i) \cdot Y_{l_i m_{l_i}}(\theta_i, \varphi_i) \cdot \sigma_{m_{s_i}}(S_{z_i}) \tag{3.5}$$

where the radial and angular parts are separated, implying that the radial and angular matrix elements can be calculated separately.

Neglecting any correlation between the position of the i^{th} electron and the other $(N-1)$ electrons, we can construct a basis function ψ for the entire atom given as a product of each $\varphi_i(r_i)$ one-electron wavefunction

$$\psi = \prod_i^N \varphi_i(r_i)$$

From the fact that the electrons are physically indistinguishable, it follows a fundamental postulate of quantum mechanics that the total wavefunction ψ is antisymmetric upon interchange of two electrons. Thus, the antisymmetrized wavefunction of the atom it can be written in the form of a determinant and is referred as a Slater determinant [19]. It follows that the use of antisymmetrized wavefunction in the N-body problem of the atom, brings the Pauli exclusion principle "*No two electrons can occupy the same spin-orbital*". In practice, the Pauli principle imposes restriction to the possible values of orbital- m_{l_i} and spin- m_{s_i} quantum numbers for equivalent electrons (electrons that have the same values of $n_i l_i$ quantum numbers). Hence, the coupling of the basis wavefunctions predicted by the vector model has to satisfy the Pauli exclusion principle.

3.1.4 Configuration-average energies

The energy of the spherically averaged atom E_{av} is given by

$$E_{av} = \frac{\sum_b \langle \psi_b | H | \psi_b \rangle}{n_{bf}} \tag{3.6}$$

where the sum is over all basis functions belonging to the electron configuration and the Hamiltonian operator is given by equation (3.2). According to Unsöld's

theorem [19], such an average is equivalent to performing a spherically symmetrized average over the angular distribution of the electrons in the atom, that is consistent with the central-field model of the atom. The average total energy of the atom

$$E_{av} = \sum_i E_k^i + \sum_i E_n^i + \sum_{i>j} \sum E^{ij} \tag{3.7}$$

is the sum of all configuration-average kinetic and electron-nuclear energies of all electrons plus the averaged electron-electron Coulomb interactions summed over all electron pairs. The sum of all diagonal matrix elements of the spin-orbit term in the Hamiltonian is equal to zero

$$\langle \psi_b | \sum_i \xi_i (l_i \cdot s_i) | \psi_b \rangle_{av} = 0$$

because each two matrix elements will have the same magnitude but different signs ($m_{s_i} = \pm\frac{1}{2}$).

The averaged kinetic energy of an electron is given by

$$E_k^i \equiv \int_0^\infty P^*_{n_i l_i}(r)[-\frac{d^2}{dr^2} + \frac{l_i(l_i+1)}{r^2}]P_{n_i l_i}(r)dr \tag{3.8}$$

and the averaged electron-nuclear energy of an electron is given by

$$E_n^i \equiv \int_0^\infty (-\frac{2Z}{r})|P_i(r)|^2 dr \tag{3.9}$$

The configuration-average electron-electron Coulomb energy is obtained by expanding the $\frac{2}{r_{ij}}$ term in the Legendre polynomials and separating the radial part from the angular part. It contains two terms, the "direct" term and the "exchange" term in which the spin-orbitals of two electrons have been changed,

$$E^{ij} \equiv \langle \psi^i \psi^j | \frac{2}{r_{ij}} | \psi^i \psi^j \rangle_{av} - \langle \psi^i \psi^j | \frac{2}{r_{ij}} | \psi^j \psi^i \rangle_{av}$$

The direct term represents the positive energy of mutual electrostatic repulsion for an uncorrelated spatial distribution of the electrons. The exchange term is a consequence of having used an antisymmetrized wavefunction to reflect the quantum-mechanical indistinguishability of electrons, and it represents the decrease in the mutual electrostatic repulsion when the positional correlation of parallel-spin electrons is included.

The averaged electron-electron Coulomb energy is

$$E^{ij} = F^0(ij) - \frac{1}{2}\sum_k \begin{pmatrix} l_i & k & l_j \\ 0 & 0 & 0 \end{pmatrix} G^k(ij) \tag{3.10}$$

where

$$F^k(ij) = \int_0^\infty \int_0^\infty \frac{2r_<^k}{r_>^{k+1}} |P_i(r_1)|^2 |P_j(r_2)|^2 dr_1 dr_2 \tag{3.11}$$

$$G^k(ij) = \int_0^\infty \int_0^\infty \frac{2r_<^k}{r_>^{k+1}} P_i^*(r_1)||P_j^*(r_2)P_j(r_1)||P_i(r_2)dr_1 dr_2 \tag{3.12}$$

The radial integrals F^k and G^k are frequently referred to as Slater integrals, and k is the k-th power of the Legendre polynomials determined by the triangle conditions [19]. For the direct Coulomb interaction $F^k(ij)$; k=0,2,4, ... $\min(2l_i, 2l_j)$ and for the exchange Coulomb interaction $G^k(1,j)$; $k = |l_i - l_j|$, $|l_i - l_j| + 2$, ... $l_i + l_j$.

The expressions of averaged kinetic (3.8), electron-nuclear (3.9), and electron-electron Coulomb (3.10) energies are substituted into (3.4) and the set of Hartree-Fock equations is solved numerically by an iterative procedure. The variational principle is applied so that for any set of small variations of the radial wavefunction $\delta P_i(r)$, the configuration-average energy is minimized and the output wavefunctions are self consistent with the trial input wavefunctions. This is the reason why the Hartee-Fock method is refereed in literature also as self consistent field method (SCF). Because the solution of the Hartree-Fock equations depends on the variational principle, the Hartree-Fock energy of an electronic configuration is higher than the true energy.

3.1.5 Electron correlation

The Hartree-Fock method relies on the independent electron approximation and does not take correctly into account electron correlation, leading to a total electronic energy higher from the exact solution of the non-relativistic Schrödinger equation. This energy difference is called correlation energy. Hartree-Fock approximation considers only a certain amount of electron correlation, which is due to the spatial correlation of two-parallel spin electrons, found in the exchange term. However, the Coulomb correlation between the spatial positions of electrons with opposite spin due to their Coulomb repulsion is not considered in the model. A method correcting for the correlation energy is the configuration interaction (CI) method. In this method one assumes that the ground state is not single

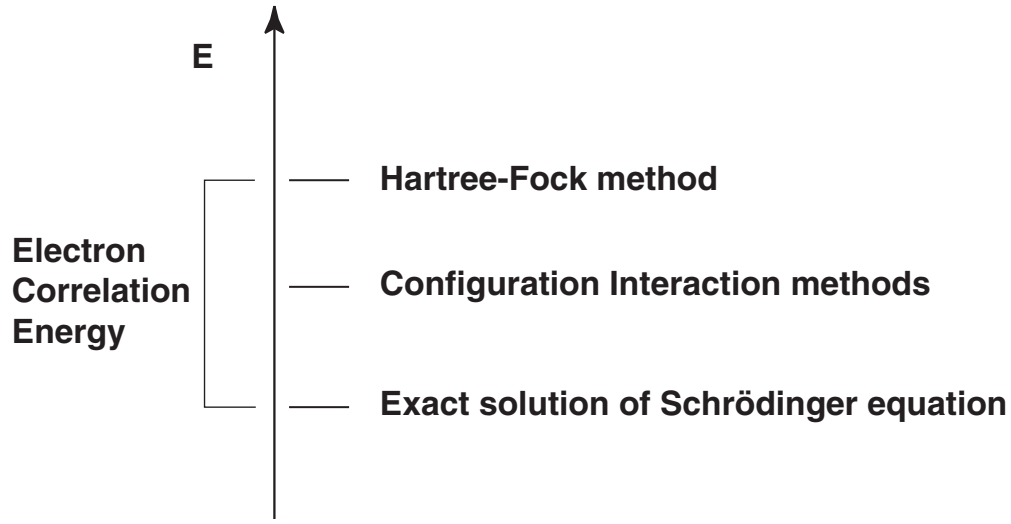

Figure 3.1: Electron correlation energy in terms of different theories for solving the Schrödinger equation

configurational but contains an admixture of a series of configurations. Thus, the calculation scheme is extended by including excited configurations to the ground configuration and the variation principle is used to minimize the energy in the Schrödinger equation with respect to the complete electronic Hamiltonian. In this case the basis set includes functions from the excited configurations and the ground configuration, and each computed eigenfunction ψ will be a mixture of basis functions from all configurations. However, the CI method is not favorable for calculations of large atoms because it is very time-consuming.

It has been found that the reduction of HF-values of the Slater integrals to 80% corrects for configuration interaction [19, 20], and gives good agreement with the experiment [21]. In our calculations throughout this thesis i have used HF single-configuration approximation with the semi-empirical correction to the Slater integrals.

3.2 Theoretical aspects of X-ray absorption

3.2.1 Electric dipole approximation

Absorption spectroscopy is the method that investigates the absorption of electromagnetic radiation by an atom, molecule or solid. The intensity of an X-ray absorption spectrum is proportional to the transition rate given by Fermi golden rule that states that the transition probability W between a system in its initial state ψ_i and final state ψ_f is given by

$$W_{fi} = \frac{2\pi}{\hbar}|\langle\psi_f|T|\rangle\psi_i|^2\delta(E_i - E_f + \hbar\omega) \tag{3.13}$$

The delta function takes care of the energy conservation and a transition takes place if the energy of the final state equals the energy of the initial state plus the energy of the X-ray photon. The squared matrix elements gives the transition rates, and the transition operator T is the perturbation term describing the dominant interaction between the electromagnetic field and the electrons in the atom

$$T = \frac{e}{mc}\mathbf{A}(\mathbf{r}) \cdot \mathbf{p}$$

$\mathbf{p} = \sum \mathbf{p_i}$ is the sum of linear momentum operators of the electrons in the atom, and $\mathbf{A}(\mathbf{r})$ is the vector potential of the incident electromagnetic field that is given by

$$\mathbf{A}(\mathbf{r}) = \sum_q \hat{\mathbf{e}}_\mathbf{q} A_0 e^{i\mathbf{k}\cdot\mathbf{r}}$$

The summation is over its different polarizations q.

Thus, the intensity of an X-ray absorption spectrum (I_{XAS}) is proportional to

$$I_{XAS} \propto \sum_q \sum_f |\langle\psi_f|A_0 e^{i\mathbf{k}\cdot\mathbf{r}}\hat{\mathbf{e}}_\mathbf{q} \cdot \mathbf{p}|\psi_i\rangle|^2\delta(E_i - E_f + \hbar\omega) \tag{3.14}$$

The wavefunctions ψ_i and ψ_f refer, respectively, to the initial and final eigenstates of the full N-electron Hamiltanians H for the initial state and H' for the final state, with energies E_i and E_f, respectively. It is assumed that the initial state is a single configuration ground state and the summation in the final state is over all different f core-excited final states.

For core-excitations in the soft X-ray region, the spatial dependence of the vector potential $\mathbf{A}(\mathbf{r})$ can in a good approximation be neglected, because the wavelength is much larger than the core excited electron wavefunction, i.e., $\mathbf{k} \ll \mathbf{r}$, and from the Taylor expansion $e^{i\mathbf{k}\cdot\mathbf{r}} = 1+i\mathbf{k}\cdot\mathbf{r}+...$, only the first term is retained. This important approximation is known as electric dipole approximation. The momentum operator $\mathbf{p}$ of the electrons can be replaced by the position operator $\mathbf{r}$, using the commutator $[H, \mathbf{r}] = \mathbf{p}/m$. (This replacement is exact only if the same Hamiltonian is used in the initial and final state [22].) Thus, the momentum form of the dipole operator can be replaced by the position form,

$$\hat{\mathbf{e}} \cdot \nabla \leftrightarrow \frac{\hbar\omega}{m}\hat{\mathbf{e}} \cdot \mathbf{r}$$

In the case of a linearly-polarized radiation field $\hat{\mathbf{e}} \perp \mathbf{k}$ the intensity of the X-ray absorption spectrum in the dipole approximation reads,

$$I_{XAS} \propto \sum_f |\langle\psi_f|\hat{\mathbf{e}} \cdot \mathbf{r}|\psi_i\rangle|^2 \delta(E_i - E_f + \hbar\omega) \tag{3.15}$$

3.2.2 Single electron approximation

In the single electron approximation is assumed that the electron from the core orbital is excited to the empty valence orbital, while all the other electrons do not participate in the X-ray induced transition. This approximation makes it possible to write the initial state wavefunction as a product of the core and $N-1$ electron wavefunctions $|\psi_i\rangle = |\varphi_c\rangle|\Phi_{N-1}\rangle$, and the final state wavefunction as a product of the core hole, the photoelectron and the $N-1$ "passive" electrons wavefunctions $|\psi_f\rangle = |\varphi_{\underline{c}}\varphi_\varepsilon\rangle|\Phi_{N-1}\rangle$.

In this frozen-structure approximation the remaining electrons are described by the same wavefunction as in the initial state [23]. Hereby, the absorption coefficient is governed by a single electron matrix element, which often is constant or slowly varying in energy [24]

$$\langle\psi_f|\hat{\mathbf{e}} \cdot \mathbf{r}|\psi_i\rangle|^2 = |\langle\varphi_{\underline{c}}\varphi_\varepsilon|\langle\Phi_{N-1}|\hat{\mathbf{e}} \cdot \mathbf{r}|\varphi_c\rangle|\Phi_{N-1}\rangle|^2 \approx |\langle\varphi_\varepsilon|\hat{\mathbf{e}} \cdot \mathbf{r}|\varphi_c\rangle|^2 \tag{3.16}$$

The core hole is localized and has a well-defined energy, and the summation over all final states implies that the delta function can be reformulated with the empty orbitals or unoccupied density of states ρ. This yields that in the single electron approximation the intensity of the X-ray absorption is given by

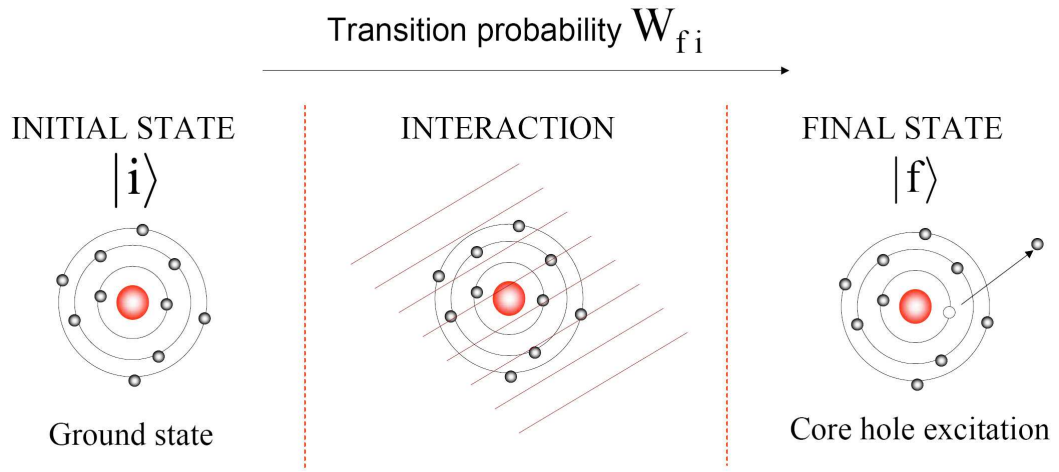

Figure 3.2: Schematic of single electron approximation

$$I_{XAS} \propto |\langle\varphi_\varepsilon|\hat{\mathbf{e}}\cdot\mathbf{r}|\varphi_c\rangle|^2\rho \tag{3.17}$$

From this equation it follows the initial state rule which states that the integrated intensity of the XAS relates to the number of holes in the initial state. Indeed, integrating equation 3.17 over the complete edge and assuming that the core state is 100% occupied in the initial state one finds that the integrated XAS spectrum gives the number of vacant holes in the valence band.

The frozen approximation works well in case of metals, where the core hole is screened from the free valence electrons and the excited photoelectron will feel the same potential as the one in the initial state. However, in atoms and ionic compounds the presence of the core hole in the excited state will cause a redistribution of the density of states. To account for the presence of the core hole in the excited state, one substitute the unoccupied initial state (unperturbed) density of states ρ in 3.17 with the final state density of states ρ'. This approximation is known as the final state rule [25] which states that within the single-particle approach the transition matrix elements are calculated from wavefunctions obtained in the potential of the final state of the absorption process,

$$\langle\psi_f|\hat{\mathbf{e}}\cdot\mathbf{r}|\psi_i\rangle|^2 \approx |\langle\varphi_\varepsilon|\hat{\mathbf{e}}\cdot\mathbf{r}|\varphi_c\rangle\langle\Phi_{N-1}|\Phi'_{N-1}\rangle|^2 = M^2 \tag{3.18}$$

where $|\Phi'_{N-1}\rangle$ are the wavefunctions of the $N-1$ fully relaxed electrons. This approximation is valid in the adiabatic excitation limit [2] in which the physical

picture of the XAS process is that the excited electron is either trapped in a bound state or leaves the atom or molecule slowly and the excited atom lowers its energy by slowly adjusting to the effective atomic potential. Thus, the final state rule implies that the XAS spectral shape is determined by the final state density of states

$$I_{XAS} \propto M^2 \rho' \tag{3.19}$$

The final state DOS is calculated within the local density approximation of density functional theory (DFT) [26, 27]. Within DFT, there are different approximations for treating the fully relaxed hole state. The so-called "$Z+1$ approximation", replaces the excited atom for the next one in the periodic table partially imitating the compression of the electron orbitals due to the core hole potential, but neglecting the difference between, e.g., a core hole in the K and L shells. A more sophisticated approach directly introduces the frozen hole in the inner orbital and puts the excess charge as an extra electron in the valence band or smears the charge uniformly over space. In some cases, the $Z+1$ and the core excited calculations will fail to reproduce the experimental spectra, as in the case of Cu^{II} systems [28]. In these cases, a half core hole is introduced in the calculations (i.e., the core state is half occupied with an electron), which is consistent with the Slater' transition state theory [2] that treats the relaxation effects by second order perturbation theory. The half core hole calculation reproduces more accurately core electrons binding energies and XAS spectra.

Within the single electron approximation, the many-body effects that are due to the finite lifetime of the core hole state are excluded from the calculations. Through the uncertainty principle, the core hole state with a finite lifetime does not have a sharp (or delta-function-like) energy level, but is better thought as having a finite width. Thus the calculated density of states are convoluted with a Lorenzian.

3.2.3 Selection rules

In the electric dipole approximation the dipole operator $\hat{\mathbf{e}} \cdot \mathbf{r}$ is of odd parity and this corresponds physically to the absorbed photon carrying off one unit of angular momentum. From the conservation of angular momentum it follows that

$$\Delta l_i = \pm 1$$

the angular momentum of the excited electron differs by one from the core hole state. Because, the electric dipole operator involves only the orbital and not the spin coordinates, which physically corresponds to the X-rays carrying no spin, the conservation of spin gives:

$$\Delta s_i = 0$$

Given these restrictions, the selection rule for the overall momentum quantum number is:

$$\Delta J = 0, \pm 1 \quad (J = J' = 0 \quad \text{isexcluded})$$

For extended final states (the Bloch-like wavefunctions in density functional method) J is not a good quantum number and the only selection rules are $\Delta l_i = \pm 1$ and $\Delta s_i = 0$.

3.2.4 $1s$ edge X-ray absorption

The single electron approximation within the density functional theory works well for the calculation of $1s$ edge X-ray absorption spectra. In this framework, there exist various methods based on band structure (reciprocal space) and multiple scattering (real space) techniques to calculate accurately the measured spectra.

In the case of K-edge, absorption process involves the excitation of of an $1s$ (l=0) electron. According to the dipole selection rule, the final states will have contributions from p-type orbitals (l=1). Because the $1s$ core hole bears no angular momentum, there are no multipole interactions of the core hole with the valence electrons. Thus, the K-edge absorption spectra can be envisioned, in a good approximation, as an image of the p-projected unoccupied density of states. In my work I have used the oxygen K-edge NEXAFS as a method to investigate oxygen-lanthanide ion covalency within the lanthanide orthophosphate series and the surface influence on the unoccupied density of states of the nanoparticles.

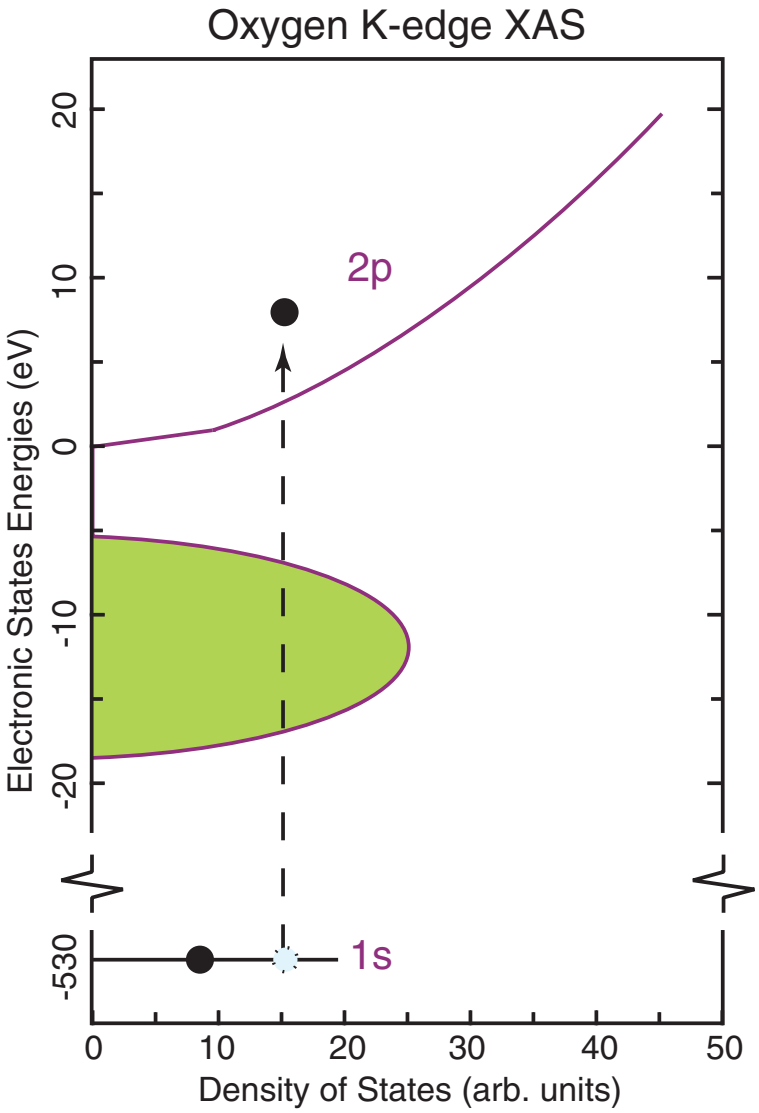

Figure 3.3: Schematic of the p-projected unoccupied density of states revealed from the Oxygen K-edge absorption spectra

3.2.5 Atomic multiplet theory

In the case of $M_{4,5}$ and $N_{4,5}$ X-ray absorption edges of lanthanide metals the breakdown of the single electron approximation occurs. This is due to the fact that the core holes posses an angular momentum different from zero ($l = 2$) which give rise to a spin-orbit interaction of the core hole and to a strong Coulomb interaction of the core hole with valence electrons. The later process is significantly strong due to the localization of the $4f$ valence orbitals that give rise to a strong overlap of the core hole and the valence wavefunctions. As a consequence, the quantum mechanical state of these systems is described, according to the vector coupling, by coupled wavefunctions. On the basis of the symmetry properties of the coupled wavefunctions and the ground state wavefunctions, the dipole transition of the X-ray absorption process, will put restrictions on the core excited final states. As a result, from the X-ray absorption spectra of these systems one does not observe anymore the unoccupied density of states. However, in order to obtain an accurate description of the NEXAFS spectra these multiplet effects, that occur due to the strong local interaction, have to be considered. A successful method to analyze the NEXAFS spectral shape in these systems is based on atomic multiplet model [20, 24, 29] and here i will briefly introduce it.

Atomic multiplet theory is used to describe the electronic correlated states in the partially filled atomic shells. In this case, the Hamiltonian operator is calculated by separating the spherical part of the fully filled atomic shells (H_{sph}) from the non-spherical part of the partially filled shell. In addition, the averaged kinetic and electron-nuclear energies of the partially filled shell are added to the spherical part and the sum of the two contributions defines the average energy (H_{av}) of the open atomic shell. Further, the energy of the spin-orbit interaction and the Coulomb electron-electron repulsion of the electrons in the outer shell is added to the averaged energy. Thus, in the case of lanthanide (3+) ions with a partly filled $4f$ shell, and a $4f^N$ ground state electronic configuration, the Hamiltonian is given by

$$H_i = H_{4f-av} + H_{4f-el} + H_{4f-ls} \tag{3.20}$$

In the final state of the XAS process, the energy of the core-excited state, its Coulomb interaction with the 4f electrons, and its spin-orbit interaction should be added.

$$H_f = H_{4f-av} + H_{4f-el} + H_{4f-ls} + H_c + H_{c-el} + H_{c-ls} \tag{3.21}$$

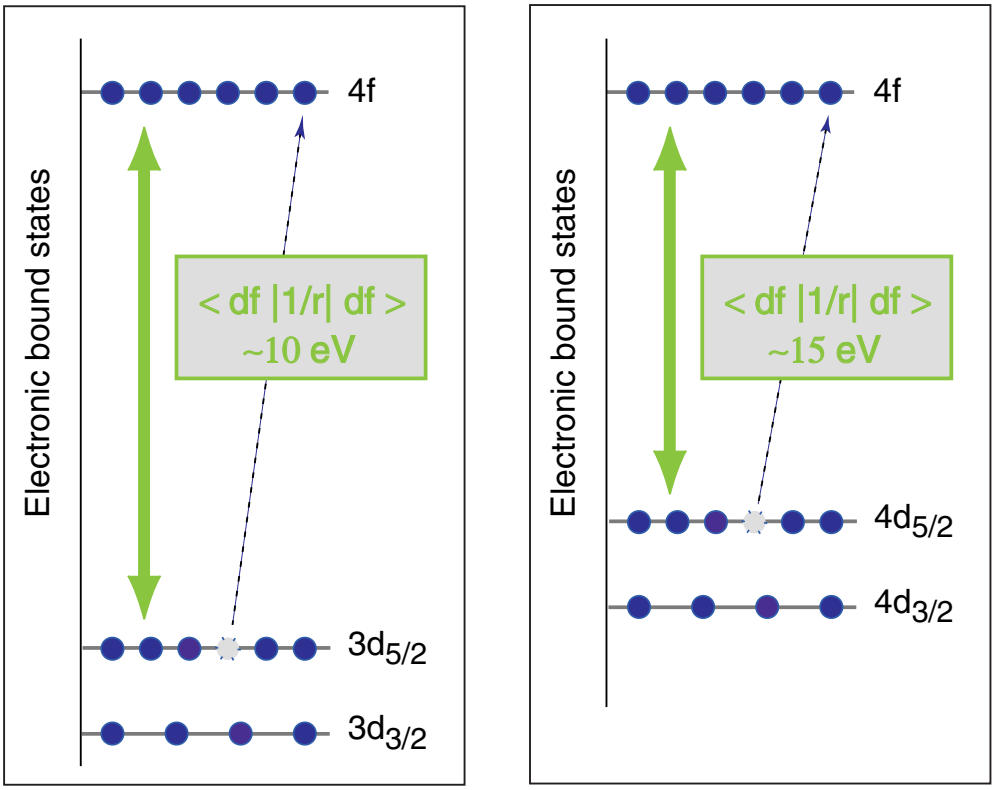

Figure 3.4: Schematic of the $3d \Leftrightarrow 4f$ and $4d \Leftrightarrow 4f$ Coulomb interaction in the lanthanides. The strong overlap of $3d$ (or $4d$) core and $4f$ valence wavefunctions causes the break down of single electron approximation.

For the $M_{4,5}$-edge X-ray absorption the transition matrix elements to be calculated are:

$$I_{XAS} \propto \langle 4f^N | \hat{\mathbf{e}} \cdot \mathbf{r} | 3d^9 4f^{N+1} \rangle^2 \tag{3.22}$$

Because, the X-ray absorption process is a dipole transition, the dipole selection rule will put restrictions to the excited final states. From the symmetry aspects, electronic configurations are indicated with their orbital angular momentum L, spin angular momentum S and total angular momentum J. Together, these three quantum numbers specify a term symbol ${}^{2S+1}L_J$ that indicate a certain state with its specific energy. In the initial state the spin-orbit interaction of the electrons in the $4f$ shell is small and the vector coupling scheme is that of LS coupling. The ground state symmetry of a partially filled $4f$ shell is given by the empirical Hund's rules (the term with highest S which has the highest L, and for

Table 3.1: The calculated Slater-Condon parameters and spin-orbit coupling of Tm^{3+} $4f^{12}$ ground state, and $3d^9 4f^{13}$ and $4d^9 4f^{13}$ excited states.

	Slater-Condon parameters (eV)						Spin-Orbit coupling (eV)	
	G_1	G_3	G_5	F_2	F_4	F_6	$(l \cdot s)_{core}$	$(l \cdot s)_{4f}$
$4f^{12}$	-	-	-	13.175	8.264	5.945	-	0.333
$3d^9 4f^{13}$	6.682	3.921	2.71	9.09	4.308	-	18.048	0.338
$4d^9 4f^{13}$	17.338	10.922	7.733	14.771	9.44	-	2.293	0.338

Table 3.2: The calculated Energies and Intensities of Tm^{3+} $4f^{12}$ ground state, and $3d^9 4f^{13}$ and $4d^9 4f^{13}$ excited states electronic symmetries

Electronic Configuration	Electronic Symmetry	$E_{av}(eV)$	Energy (eV)	Transition Energy (eV)	Transition Intensity
$4f^{12}$	$^3H_6$	0	-2.24	-	-
$3d^9 4f^{13}$		1482.67	-	-	-
	$^3H_6$	-	1462.38	1464.623	0.5135
	$^3G_5$	-	1464.44	1466.683	6.473
	$^1H_5$	-	1466.89	1469.134	0.102
	$^3H_5$	-	1510.33	1512.57	0.018
$4d^9 4f^{13}$		181.72	-	-	-
	$^3H_6$	-	172.701	174.94	0.512
	$^3H_5$	-	176.279	178.52	0.11
	$^3G_5$	-	181.304	183.54	7.025
	$^1H_5$	-	193.129	195.37	2.55^{-4}

the less than half filled shell with the lowest J). In the case of Tm^{3+} ion of $4f^{12}$ electronic configuration, the symmetry of the ground state is ${}^3H_6$. In the final state the dominant interaction is the core hole spin-orbit interaction, that obeys the jj coupling scheme. Thus, the overall coupling scheme of the final state is an intermediate coupling that consists of a mixture of jj and LS coupling. The electronic configuration is $3d^9 4f^{13}$ and according to the Pauli principle (for the LS coupling scheme[1]), the core excited state can have the following symmetries: ${}^3P_{2,1,0}$, ${}^3D_{3,2,1}$, ${}^3F_{4,3,2}$, ${}^3G_{5,4,3}$, ${}^3H_{6,5,4}$, ${}^1P_1$, ${}^1D_2$, ${}^1F_3$, ${}^1G_4$, and ${}^1H_5$. The dipole selection rule (discussed in section 3.2.3) decreases the number of reached states to only four: ${}^3H_6$, ${}^3H_5$, ${}^3G_5$ and ${}^1H_5$. Thus, from the symmetry aspects the transition matrix elements to be calculated are:

$$I_{XAS} \propto \langle {}^3H_6 | {}^1P_1 | {}^3H_6, {}^3H_5, {}^3G_5, {}^1H_5 \rangle^2 \tag{3.23}$$

where ${}^1P_1$ is the symmetry of the dipole operator.

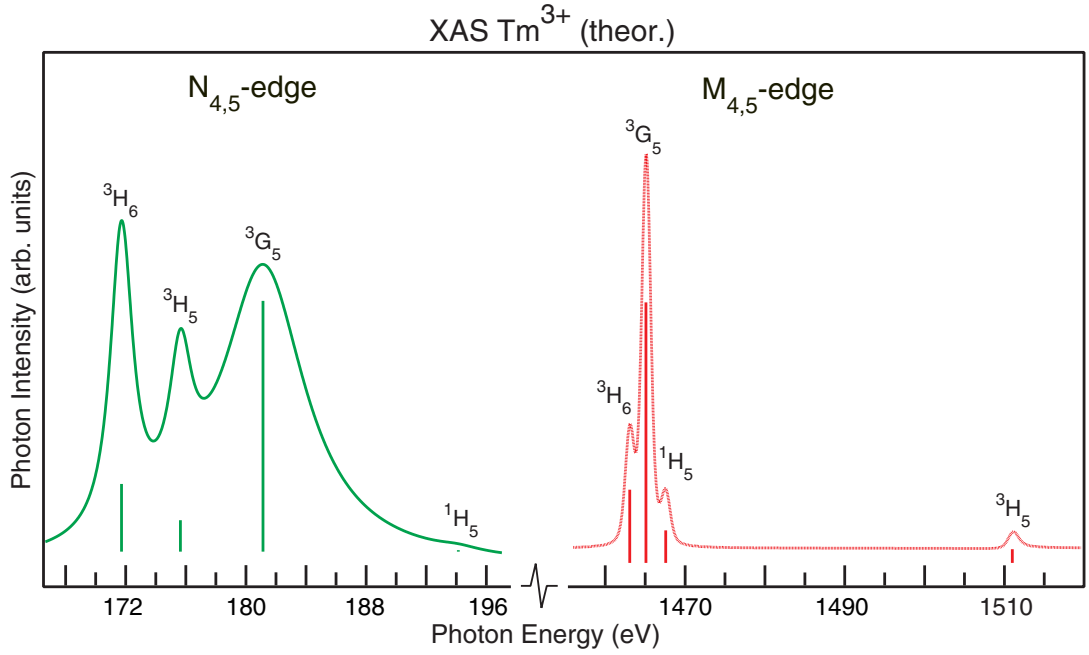

Figure 3.5: The calculated X-ray absorption spectra of Tm^{3+} $4d^{10}4f^{12} \rightarrow 4d^9 4f^{13}$ and $3d^{10}4f^{12} \rightarrow 3d^9 4f^{13}$ transitions. The different relative strength of electron-electron to spin-orbit interactions lead to different energetic spacing and intensities of the four final state symmetries.

[1]The energies of the various LS terms in the intermediate coupling will differ from the pure LS terms.

The problem of calculating the $3d$ XAS in Tm is reduced in solving the 3×3 energy matrix of the final states with $J = 5$ and the 1×1 energy matrix of the final state with $J = 6$.

The matrix elements of the Coulomb electron-electron interaction, are given by the diagonal elements[2]

$$\langle {}^{2S+1}L_J | \frac{e^2}{r_{1j}} | {}^{2S+1}L_J \rangle = \sum_k f_k F^k + \sum_k g_g G^k \tag{3.24}$$

and are expressed in terms of Slater-Condon parameters; f_k, F^k are, respectively, the angular and radial part of the direct Coulomb interaction and g_k, G^k are, respectively, the angular and radial part of the Coulomb exchange interaction [29].

The relative strength of the core hole spin-orbit interaction to the Slater-Condon parameters will influence the spectral shape of the X-ray absorption transition (Fig. 3.5). The deeper $3d$ core levels have a stronger spin-orbit interaction than the Coulomb interaction (please refer to the calculated parameters in Table 3.1), and this gives rise to the splitting of the final states into two group of lines $3d_{5/2}(M_5)$ and $3d_{3/2}(M_4)$ (Fig. 3.5). Contrary, in the case of $N_{4,5}$ X-ray absorption, the $4d$ core levels have a small spin-orbit interaction, but a large direct and exchange Coulomb interaction (Table 3.1). Hence, the coupling scheme is closer to the LS and the relative intensities and the energetic separations of the four final state symmetries are different from the $M_{4,5}$ X-ray absorption spectrum (Table 3.2, Fig. 3.5).

[2]The off-diagonal elements are zero because the electron-electron interaction commutes with L^2, S^2, L_z and S_z

3.3 Resonant X-ray scattering formalism

Resonant X-ray scattering process is described in the framework of second order perturbation theory. The amplitude of the RXS process is given by the so called Kramers-Heisenberg formula:

$$A_{f0} = \sum_f \left(\underbrace{\langle f|V_r|0\rangle}_{\mathrm{A_{direct}}} + \sum_i \underbrace{\frac{\langle f|V|i\rangle\langle i|V_r|0\rangle}{E_0 + \hbar\omega - E_i + \frac{i\Gamma_i}{2}}}_{\mathrm{A_{core\ hole\ assisted}}} \right) \tag{3.25}$$

consisting of the first order term with amplitude $\mathrm{A_{direct}}$ and the second order term with amplitude $\mathrm{A_{core\,hole\,assisted}}$. The initial state $|0\rangle$ and final state $|f\rangle$ wavefunctions contain the incoming photon and outgoing photon or electron, respectively. The summation is over all $|f\rangle$ final states. The intermediate $|i\rangle$ core excited state reached via the dipole transition (V_r) has a lifetime broadening Γ_i which is proportional to the decay rate of state $|i\rangle$ into any other final state. The $|f\rangle$ final state is reached either via Coulomb interaction (V_c) (an electron is emitted) or via dipole interaction (V_r) (a photon is emitted). Thus, operator V in equation 3.25 stands for Coulomb V_c or dipole V_r operator.

The cross section of a resonant scattering process at a given incident photon energy $\hbar\omega$ is given by squaring the total amplitude and invoking total energy conservation[3], i.e., $E_0 + \hbar\omega = E_f$

$$W_{f0}(\omega) = 2\pi \sum_f \left| \underbrace{\langle f|V_r|0\rangle}_{\mathrm{A_{direct}}} + \sum_i \underbrace{\frac{\langle f|V|i\rangle\langle i|V_r|0\rangle}{E_0 + \hbar\omega - E_i + \frac{i\Gamma_i}{2}}}_{\mathrm{A_{core\ hole\ assisted}}} \right|^2 \cdot \delta(E_0 + \hbar\omega - E_f) \tag{3.26}$$

E_f is the energy of the system in its final state, that constitutes of the energy ε_f of the excited final state and the energy ε of the emitted particles (photon energy or kinetic energy of the electron). Thus it follows that:

$$\varepsilon = \hbar\omega - \varepsilon_f$$

the energy of the emitted particle exhibits a linear dispersion with regard to the incident photon energy.

The δ function in the equation 3.26 ensures energy conservation within the entire process. In addition, the final ionic state can decay further within its final

[3]RXS is a coherent process in which the photon absorption and the subsequent decay can not considered as two independent steps. Therefore the energy does not have to be conserved in each step separately but only in the entire process.

lifetime which introduces a Lorentzian statistical distribution of the final state energies of width Γ_f. An ensemble average then replaces the delta function with a lorentzian [10]:

$$W_{f0}(\omega) \propto \left|A_{f0}(\omega)\right|^2 \cdot \frac{1}{|E_0 + \hbar\omega - E_f|^2 + \frac{\Gamma_f^2}{4}} \tag{3.27}$$

It follows that the inherent lineshape of the resonant scattered line it is a Lorentzian (in the presence of channel interference, that will be discussed in section 3.3.1, the lineshape may be distorted) of width Γ_f with a center energy that exhibits linear dispersion with incident photon energy. Hence, the position and width of resonant scattered line are features determined by the final ionic state. On the contrary, the intensity of emitted line it is governed by the intermediate states. This follows from equation 3.26: The $\langle i|V_r|0\rangle$ term involves correlation in both ground and intermediate states, but however this term is common to all final states. The relative intensity between different resonant scattered lines is determined by the term $\langle f|V|i\rangle$ which gives the decay rate of an intermediate state to the different final states.

Resonant photoemission

In the situation that the scatterer is left by an electron the process is named resonant photoemission and equation 3.26 reads as follows

$$W_{f0}(\omega) = 2\pi \sum_f \left| \underbrace{\langle f|V_r|0\rangle}_{\mathrm{A_{Photoemission}}} + \sum_i \underbrace{\frac{\langle f|V_c|i\rangle\langle i|V_r|0\rangle}{E_0 + \hbar\omega - E_i + \frac{i\Gamma_i}{2}}}_{\mathrm{A_{Res.\ Photoemiss.}}} \right|^2 \cdot \delta(E_0 + \hbar\omega - E_f) \tag{3.28}$$

where the decay of the intermediate state is governed by the V_c Coulomb operator.

Resonant Inelastic X-ray scattering

In the situation that the scatterer is left by a photon the process is called resonant inelastic X-ray scattering and equation 3.26 reads as follows

$$W_{f0}(\omega) = 2\pi \sum_f \left| \underbrace{\langle f|0\rangle}_{\mathrm{A_{Thomson}}} + \sum_i \underbrace{\frac{\langle f|V_r|i\rangle\langle i|V_r|0\rangle}{E_0 + \hbar\omega - E_i + \frac{i\Gamma_i}{2}}}_{\mathrm{A_{RIXS}}} \right|^2 \cdot \delta(E_0 + \hbar\omega - E_f) \tag{3.29}$$

where the decay of the intermediate state is governed by the V_r dipole operator. In this case the direct term collapses to purely elastic scattering of the incident light from the free electrons, thus the emitted photon energy equals the incident photon energy.

3.3.1 Channel interference

Equation 3.25 reveals that the physical scattering amplitude of a final state $|f\rangle$ is given as the coherent sum of all scattering processes, and the intensity of the scattered line is given as the square of the sum of different scattering amplitudes:

$$\begin{aligned} W_{f0} &\propto \left| A_{\text{direct}} + \sum_i A_{\text{core hole assisted}}(i) \right|^2 = \\ &\propto \left|A_{\text{direct}}\right|^2 + \sum_i \left|A_{\text{core hole assisted}}(i)\right|^2 + \text{interference terms} \end{aligned}$$

The mixed terms between the direct and core hole assisted channels and between the various core hole assisted channels are termed interference terms. Their presence is responsible for a distortion of the profiles [30–32] of the measured spectra. The stronger the asymmetry of the spectral profile is, the stronger the interference between the two channels is, meaning similar amplitudes of the interfering channels. It is obvious that for the two channels to interfere, not only energy coherence (scattering to the same final state through different channels) is needed, but also time coherence.

Interference between direct and core hole assisted channels

In the nonradiative scattering process the same final state can be reached via a direct process (photoemission) and the core hole assisted process (resonant photoemission). If the two processes are coherent in time, they will interfere. This is typically the case when the core excited intermediate state lie above this core ionization threshold. Thus, it is said that the discrete core excited state is coupled to the continuum states through configuration interaction [30, 33]. The strength of this coupling determines the asymmetry parameter q of the spectral profiles. The square of the asymmetry parameter is equal to the ratio of the transition probability of the perturbed discrete core excited states to the unperturbed continuum states multiplied with the half width of the core hole state. High q values mean weak direct transition and hence symmetric lineshapes

since the interference is minimized. In addition, the interference between the two channels will shift the energetic position of the resonance line with respect to the energy of the core excited state to a new value termed ϵ. Thus, the line shape of such resonances is given by

$$W'_{f0} = \frac{(q+\epsilon)^2}{\epsilon^2+1}$$

known as Fano resonance profile [30]. A family of Fano curves for different q value is shown in Fig. 3.6. For $q \simeq 1$ an asymmetric valley peak profile is found and for large $q \geq 10$ a Lorentzian profile is found.

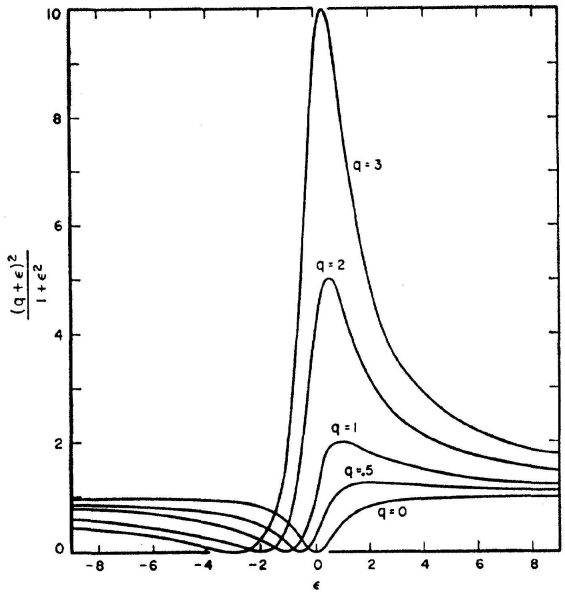

Figure 3.6: A family of Fano resonance profiles for different asymmetry parameter q value. Fano *et. al* [30]

Interference between different core hole assisted channels

The second type of interference comes from the core hole assisted intermediate states referred to as intermediate state lifetime interference. If the same final state is reached by scattering of the incident photon through two (or more) core excited states, the interference between the scattering channels will take place. This condition can be fulfilled only when the energetic spacing between the core hole intermediate states is equal or smaller than the half of the core hole lifetime

broadening $\frac{\Gamma}{2}$. Thus, without loss of generality we define as a detuning Ω from a core hole excited state:

$$\Omega = \hbar\omega - E_j$$

The resonant core hole assisted term of Eqn. 3.26 reads:

$$W_{f0}(\omega) = \left| \sum_i \frac{\langle f|V|i\rangle\langle i|V_r|0\rangle}{\Omega + (E_j - E_i) + \frac{i\Gamma_i}{2}} \right|^2 \cdot \delta(E_0 + \hbar\omega - E_f) \tag{3.30}$$

For resonant excitation $\Omega \approx 0$ the denominator remains close to the value of the core hole natural line width Γ_i. If the energetic spacing between different core hole intermediate states is comparable or smaller than the core hole lifetime broadening:

$$E_j - E_i \leq \frac{\Gamma_i}{2}$$

both scattering processes become coherent and will interfere. This can give rise again to asymmetrical spectral profiles. Both types of interference; interference of the direct and core hole assisted channels and interference between different core hole assisted channels will be subject of investigation in this thesis.

Chapter 4

Geometric and electronic structure of lanthanide orthophosphate nanoparticles determined with X-rays

Abstract[1]

The evolution of the geometric and electronic structure within the entire series of lanthanide orthophosphate nanoparticles ($\sim$ 2– $\sim$ 5nm) has been determined experimentally with X-ray diffraction and near edge X-ray absorption fine structure spectroscopy. In particular, the interplay between electronic structure, crystal morphology and crystal phase has been systematically studied. A missing local order in the crystal structure accompanied with multiple ion sites in the nanoparticles was revealed to be due to the small crystal size and large surface contribution. All lanthanide ions were found to be in "3+" configuration and accommodated in three different crystallization states: the larger lanthanide ions (La, Ce, Pr, Nd, Sm) in the monoclinic phase, the smaller ones (Er, Tm, Yb, Lu) in the tetragonal phase, and the intermediate lanthanide ions (Eu, Gd, Tb, Dy, Ho) in a "mixed phase" between monoclinic and tetragonal phases.

[1]Peer reviewed paper. This section has been published: Suljoti, Nagasono, Pietzsch, Hickmann, Trots, Haase, Wurth and Föhlisch, J. Chem. Phys. **128**, 134706 (2008).

4.1 Introduction

Nanoscience holds the promise to tailor the physical, chemical and biological properties of matter [34], evolving from "infinitely extended" solids towards nanometer-scale solids consisting of a defined cluster of atoms. In semiconductors, this evolution in size is accompanied by quantum confinement of mobile charge carriers. As a consequence, the band gap, optical properties, melting temperature and radiative lifetime of the lowest allowed optical transition can be varied in semiconductors as a function of crystal size [35]. In wide band-gap insulators, size related changes lead to changes in the electronic and geometric structures i.e., the oxidation state, the crystal phase, or unit cell distortions.

Lanthanide phosphate nanoparticles are an interesting class of wide band-gap insulators because of their optical properties. Their colloidal solutions emit infrared, visible, and ultra-violet light [15, 36–39] and, therefore, they can be used as components in lighting, displays, optoelectronic devices, lasers, and in long-lived dyes for biological labeling [37]. The lanthanide orthophosphates also display very high lattice energies and high resistance against oxidation and radiation damages, making bulk crystals of these materials a medium feasible even for nuclear-waste storage [40]. Thus, it is essential to understand how dimensionality influences the properties of lanthanide orthophosphates.

Recent studies [38, 39, 41, 42] have provided some insights on how crystal structure and kinetic factors determine the shape and size of these materials. However, an important issue to be addressed is the question of how morphology and geometric structure influence the electronic structure of these materials. Most of the reported studies are focused on their optical properties and have revealed the luminescence quantum efficiency to be very small compared to bulk materials. The intrinsic emission of pure $LaPO_4$ nanoparticles was reported to be ten times smaller in intensity than the microsized particles [43]. The luminescence quantum yield efficiencies of $CePO_4$:Tb and $LaPO_4$:Eu colloidal solutions were reported to be 16% and 10%, respectively [15], and for the $LaPO_4$ doped with different lanthanides: Pr, Nd, Er, and Yb (3+) ions was reported to be less than 15% [37].

The measured decay curves of the optical transitions in the nanoparticles showed shorter mean lifetimes (range from 1.6 up to 2.3 ms) compared to their bulk crystals [37, 44]. An additional reported aspect is the shift toward lower energies of the excitonic emission band in pure $LaPO_4$ nanoparticles [43] and of the 5d-4f transition band in CePO4 nanoparticles [45] compared to their bulk crystals. Besides, the intensity and the splitting of Eu optical transitions was shown to depend on the morphology and the crystal structure of the host lat-

tice [38]. All these aspects of the optical properties address for a systematic and detailed study of the electronic structure of the whole series of lanthanide orthophosphate nanoparticles. As a structural probe we have used the variation of the oxygen-lanthanide chemical bond length because it can be probed for the entire lanthanide orthophosphate series.

The nanoparticles of lanthanide orthophosphate series show to adopt different crystal phases and different morphologies depending on the synthetic method being used. The reason for this is that bulk lanthanide orthophosphates have several polymorphic forms; hexagonal, tetragonal and monoclinic phases. Yan *et al.* [38] have reported the fabrication of the whole orthophosphate series in the nanosize ranges based on the same hydrothermal method. In the case of larger lanthanide ions (La, Ce, and Nd), they reported the orthophosphates to adopt the monoclinic structure and rodlike morphologies with widths of 20–30nm and lengths up to 1μm. The lanthanide ions of intermediate size (Pr–Tb) preferred a partly hydrated hexagonal phase and highly anisotropic rodlike morphologies with widths of 10–100nm and lengths of 0.3–3μm, while for the smaller Ln ions (Dy–Lu, and Y), the lanthanide phosphates were obtained in the tetragonal phase and spherelike smaller morphologies which showed a reduced tendency to grow along a certain direction. Based on hydrothermal method but at slightly higher temperature and with different monomer sources, Zhang *et al.* [42] have reported the fabrication of lanthanide orthophosphates of slightly different phase structures and morphologies. They fabricated the larger lanthanide ions (La–Gd) in orthophosphates of monoclinic structure and nanorod shapes of width of 10–100nm and length of 1–10μm. The smaller lanthanide ions (Dy–Lu and Y) were fabricated in the tetragonal phase spherelike morphologies with diameter of 20–150nm, and only the Tb ions were obtained in the hydrated form $TbPO_4 \cdot 0.5H_2O$ that adopted the hexagonal structure and nanorod morphologies with width 20–150nm and length of 0.5–2μm. Lehmann *et al.* [16] have reported the fabrication of lanthanide orthophosphate series employing the solution-precipitation method. In contrast to the previous results, they reported sphere-like morphologies for the whole series with diameters in the range of 2.6–7nm. Additionally, the orthophosphates accommodating the intermediate lanthanide ions (Eu–Ho) adopted a mixed phase between that of monoclinic and tetragonal, and showed very small particle sizes with mean particle diameter of 2.6nm that lead to a high surface-to-volume ratio.

In order to investigate the influence of crystal structure and morphology in the electronic properties of the lanthanide phosphates nanoparticles, we chose for

investigation the one synthesized by the method of Lehmann *et al.* [16] for the reason that these systems are highly monodisperse. In this work, we present our experimental findings on the geometric and electronic structures of these systems. We deposited monolayer cluster films on crystalline silicon substrates and characterized them with scanning electron microcopy (SEM). We determined with X-ray powder diffraction the geometric structure of these systems. In addition, we determined the local electronic structure and the oxidation state of the lanthanide ions with near-edge X-ray absorption fine structure (NEXAFS) at the $M_{4,5}$-edge of each lanthanide. Finally, chemical bonding within the phosphate group in the nanoparticles and its interplay with the crystal phase and crystal dimension has been studied by oxygen K-edge NEXAFS.

4.2 Experiment

4.2.1 Colloidal chemistry and synthesis

Colloidal chemistry has been used extensively to synthesize monodisperse soluble particles of the nanometer scale. The working principle of this method is that in a supersaturated solid solution, where the system is kinetically overdriven by a high monomer concentration, diffusion effects bring about the formation of grains of a new phase [46]. Further, the temperature controlled nucleation in the presence of coordinating surfactants follows controlled steady growth of the existing nuclei [47]. The surfactants passivate the particles surface i.e., the dangling bonds are terminated with an organic addend that reduces significantly the chemical reactivity of the clusters. Based on this method [15, 16], the whole series of lanthanide orthophosphate nanoparticles has been synthesized. The particles surface is coordinated by amine chains that are responsible for their colloidal solubility and stability with respect to agglomeration. The crystallinity of the particles is investigated using the X-ray powder diffraction technique. The size distribution and the shape of the nanoparticles are examined by making use of the different methods: dynamic light scattering (DLS), X-ray diffraction (XRD), and transmission electron microscopy (TEM).

4.2.2 Thin film preparation

The lanthanide nanocrystals were dissolved in methanol solutions at 0.25% and 1% weight concentrations and then spin coated on silicon wafers. The substrates of 12 mm^2 size and 525μm thickness were mirror-polished silicon single

crystals of the (100) orientation. They were of p-type (doped with Boron) with a resistivity of ~ 5 Ωcm. Prior to the spin coating procedure a surface cleaning and passivation procedure was applied to the silicon wafers.

The silicon substrates were cleaned ultrasonically in acetone, in isopropanol and then in deionized water for 10 min, respectively. Afterward, they were chemically etched in solution of 10% hydrofluoric acids (HF) : 50% ethanol : 40% water for 10 min, a recipe given by [17]. The chemical HF etching of silicon wafers removes the surface oxide and terminates the silicon surface with atomic hydrogen. The hydrogen termination retards the silicon surface oxidation and protects the surface from chemical attack. In order to remove the physisorbed chemicals on the surface such as SiF_4, NH_4OH, HF and other molecules, the wafers were rinsed briefly with de-ionized water [18] subsequently after the chemical etching. Ultimately, a drop of lanthanide phosphate solution was spin coated on the cleaned and hydrogen-passivated surface for 1 sec at 1000 rpm, 11 sec at 4000 rpm and 19 sec at 8000 rpm. The morphology of the thin film was investigated by (SEM) which showed a uniform distribution of the nanocrystals on the silicon surface. In the case of 0.25% concentration solutions, the surface coverage was less than one monolayer for all the lanthanide nanoparticles where the particle-packing ratio differed slightly from one lanthanide ion to the other. In the Fig. 4.1 we show as an example the SEM images of the $ErPO_4$ and $YbPO_4$ nanoparticles of 0.25% concentration solution.

4.2.3 X-ray spectroscopy and diffraction

X-ray spectroscopy experiments were performed at the synchrotron radiation facilities Bessy II in Berlin and Hasylab in Hamburg at the beamlines U41 PGM and BW3. The spectroscopic investigations were performed on the Hamburg inelastic X-ray scattering system (HIXSS) that is equipped with a load-lock chamber, the preparation chamber and the spectroscopy chamber. The samples were brought into the load-lock chamber and were pumped for few minutes at a pressure of $1 \cdot 10^{-7}$ mbar; then, they were transferred through a transfer system into the UHV spectroscopy chamber equipped with a hemispherical photoelectron analyzer and a soft X-ray emission spectrometer. The synchrotron beam hit the sample under an angle of 7° with respect to the surface plane. The photons were linearly polarized with polarization vector parallel to the sample surface. The resolving power $E/\Delta E$ of the photon beam was 2400 at the BW3 beamline for the oxygen K-edge and 3500 at the U41 PGM beamline for the $M_{4,5}$-edges of the lanthanides. The NEXAFS spectra were measured in the total electron

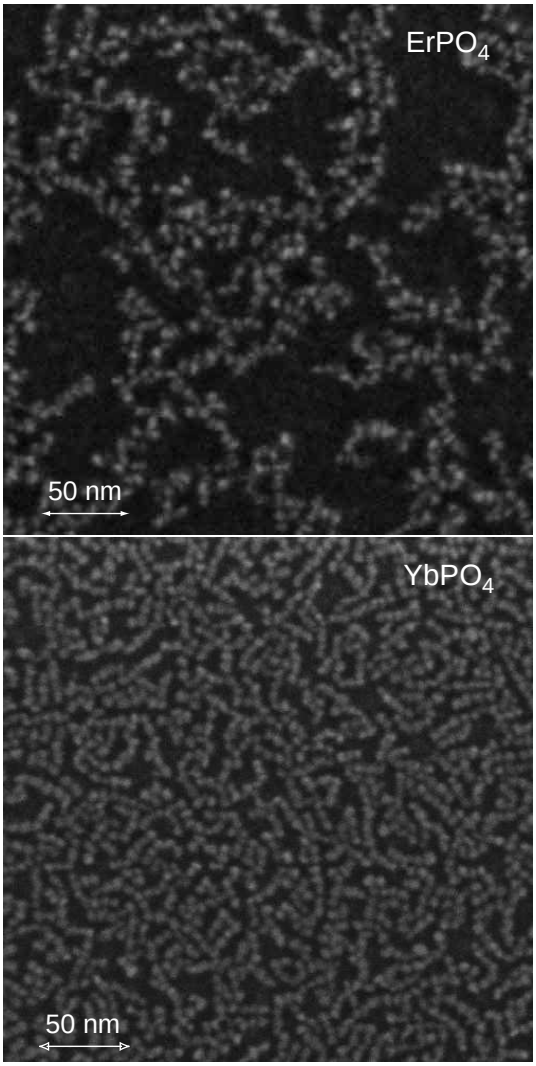

Figure 4.1: Scanning electron micrographs: top panel $ErPO_4$ (300 x 300nm^2) and bottom panel $YbPO_4$ (294 x 294nm^2) submonolayers spin coated on cleaned and hydrogen passivated silicon (100) surfaces. They show a uniform distribution of the nanoparticles at slightly different particle-packing ratio for Er and Yb.

yield (TEY) mode by monitoring the sample current and in the constant emission energy mode by monitoring the Auger lines at a fixed energy window with the electron analyzer. The electron analyzer was collecting the electrons from the sample at the magic angle with respect to the linear polarization of the incident radiation.

X-ray diffraction experiments were performed at B2 beamline at the Hasylab synchrotron radiation facility in Hamburg equipped with a powder diffractometer and a image plate detector [48]. The diffraction patterns of powder nanoparticles were collected from flat-sample transmission geometry with X-ray photons of energy 26.26 keV (wavelength λ=0.472 Å).

4.3 Long-range order in the crystallites

The crystal structure of lanthanide orthophosphate nanoparticles has been identified by X-ray powder diffraction analysis. In Fig. 4.2, we show their diffractograms. All diffraction patterns are characterized by considerably broad reflection peaks owing to the small crystallite size of the nanoparticles. In the case of intermediate lanthanide ions (Eu, Gd, Tb, Dy, Ho), the diffraction patterns are extremely broad, indicating a smaller crystallite size. The analysis of the diffraction patterns was done by full-profile Rietveld refinements [49] that revealed the structures to be isotropic with no preferred direction. The mean particle size was roughly determined from the broadening of the reflection peaks using the Sherrer formula [50, 51]. The calculated diffraction patterns of the nanoparticles using the Rietveld structural refinement showed that the larger lanthanide ions (La, Ce, Pr, Nd, Sm) adopted the same monoclinic phase of monazite as their respective bulk crystals and the smaller ones (Er, Tm, Yb) adopted the same tetragonal structure of xenotime as their respective bulk crystals. In Fig. 4.3, we have shown the crystallographic calculations compared with the measured diffraction patterns for $LaPO_4$ and $LuPO_4$ nanoparticles.

An exception are the lanthanide nanoparticles from the middle of the series (Eu, Gd, Tb, Dy, Ho). In accordance with the previously reported results [16] these nanoparticles do not show the crystal phase of the respective bulks. Their diffractograms exhibit a crystal phase that is neither monoclinic nor tetragonal, but a “mixed phase” of monoclinic and tetragonal. In addition, our measurements revealed a slight phase transition from monoclinic to tetragonal, where Eu showed a crystal phase more similar to monoclinic and Ho showed a crystal phase more similar to tetragonal.

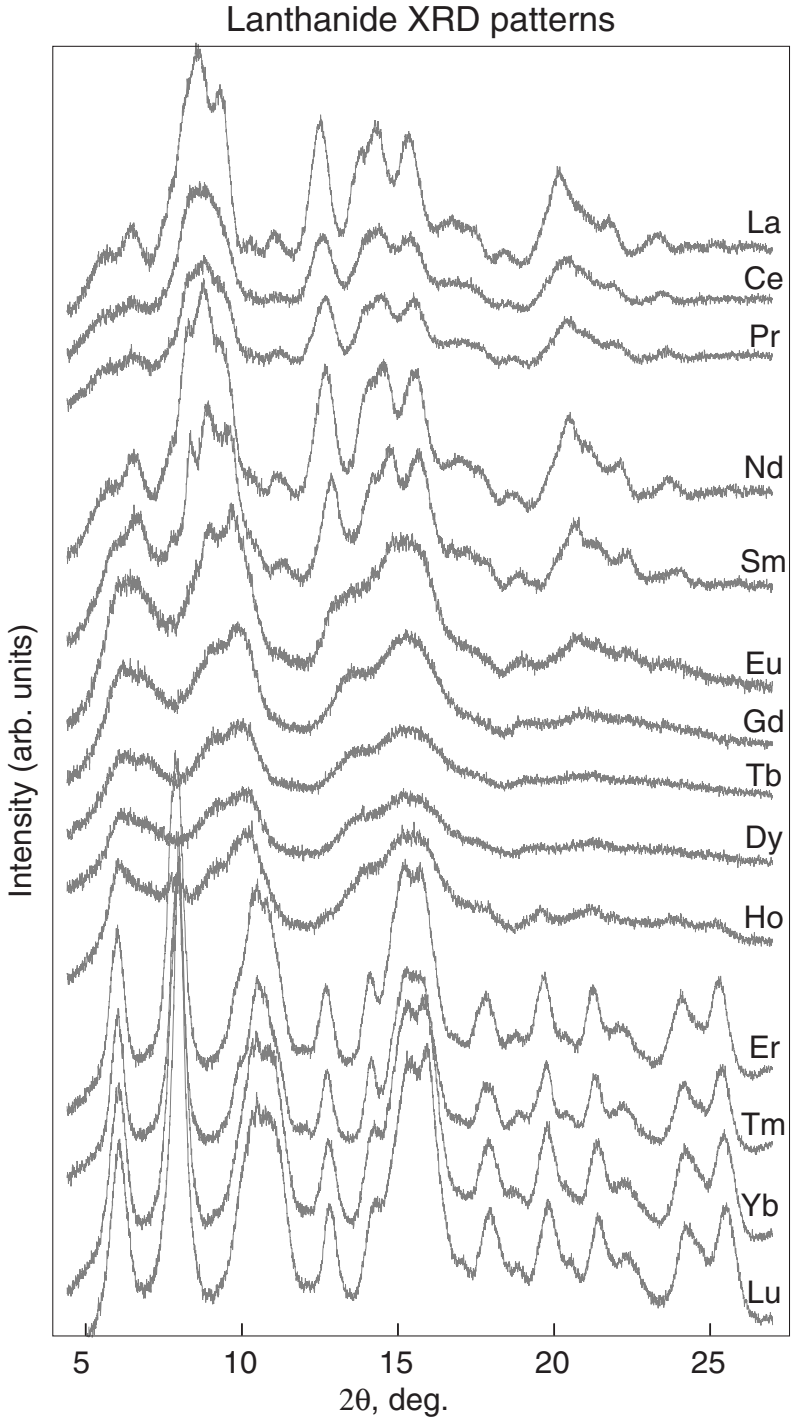

Figure 4.2: X-ray powder diffraction patterns of lanthanide phosphate nanoparticles. Broad diffraction peaks indicate the small crystal size of 2–5 nm. La–Sm crystals are in monoclinic phase, Er–Lu crystals are in tetragonal phase, and Eu–Ho crystals are in "mixed phase" between monoclinic and tetragonal phase and are even smaller in size as seen from the peak width.

At large scattering angles (above 20 degree), the diffraction patterns of the intermediate lanthanides are characterized by very broad peaks due to diffraction from atomic planes at small interatomic distances of 1.5 Å to 2 Å. The blurred diffraction patterns are a fingerprint for a missing short-range order of the atomic arrangements in these nanoparticles.

Inquiring into the reasons of the blurred patterns, we analyzed the morphologies and sizes of the nanoparticles. Highly resolved TEM images, and particle-mean size calculations from the diffraction peak broadening, revealed the very small particles of spherical shapes. In Fig. 4.4, high-resolution TEM images of $PrPO_4$ and $YbPO_4$ nanoparticles are shown. The particle size within the lanthanide series exhibited the same trend as the crystal phase. The larger lanthanide ions (La, Ce, Pr, Nd, Sm) and the smaller ones (Er, Tm, Yb, Lu) showed to have a particle size of $\sim$ 3–5nm diameter. The intermediate lanthanide ions (Eu, Gd, Tb, Dy, Ho) showed very small particle sizes of about $\sim$ 2nm, that is accompanied with a high surface contribution in these particles.

This trend of the crystal-phase and the crystal-size evolution through the lanthanide series was reported in [16] to be closely related to the decreasing effective cation radii with increasing the atomic number, known as "lanthanide contraction". For a detailed discussion, we are considering here the crystallographic studies of lanthanide orthophosphate bulk crystals [52]. Ni *et al.* have shown that distinct similarities exist between the monoclinic and tetragonal structures. Both atomic arrangements are based on [001] chains of intervening phosphate tetrahedra and lanthanide (Ln) polyhedra. As the structure "transforms" from monoclinic to tetragonal, the lanthanide polyhedron transforms from LnO_9 to LnO_8. Projected along the [001] direction, the tetrahedra-polyhedra chains exist in the (100) planes, with two planes per unit cell in both structures. In the monoclinic phase, the planes are offset by 2.2 Å along [010] relative to those in the tetragonal phase, in order to accommodate the larger lanthanide atoms. The shift of the planes in the monoclinic phase allows the Ln atom to bond to an additional oxygen atom to complete the $LnPO_9$ polyhedron. Additionally, Ni *et al.* showed that the unit cell of $TbPO_4$ tetragonal is larger than that of $GdPO_4$ monoclinic, despite the fact that Tb is smaller than Gd. This fact demonstrates that the void space in the tetragonal phase is larger compared to that in the monoclinic phase, thus, creating an energetically unfavorable situation. As the intermediate lanthanide particles have a very small size of $\leq$ 3nm, which corresponds to a surface to volume contribution of $\sim$ 70%, a rearrangement of the atomic positions occurs so that the total energy of the system is minimized. Furthermore,

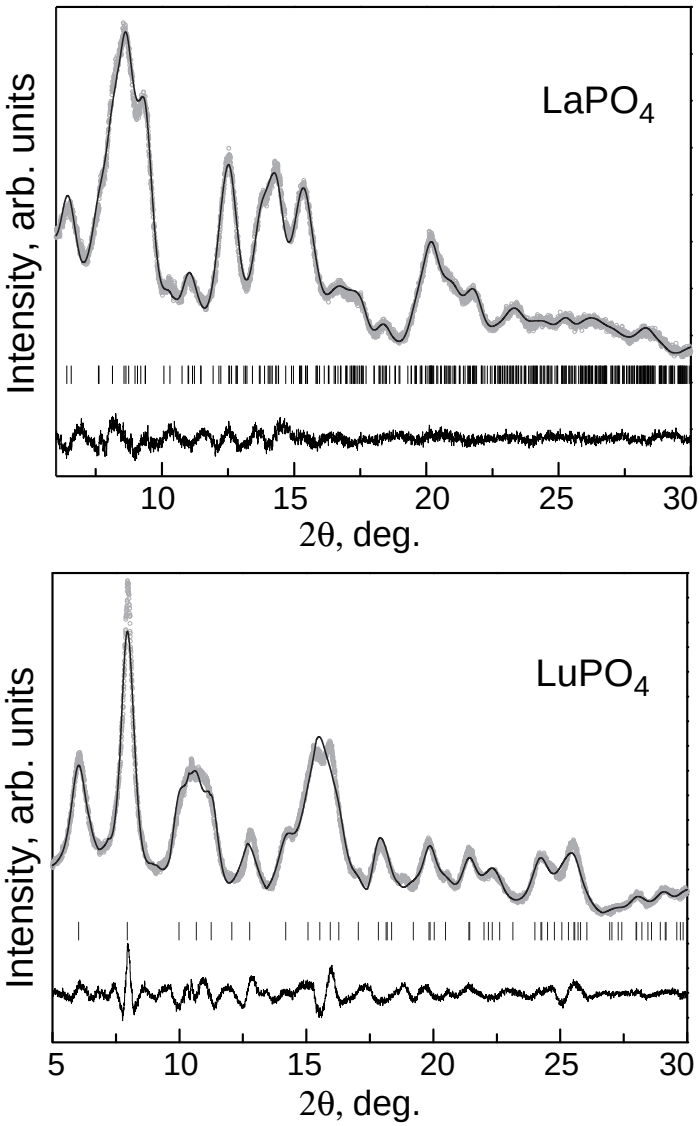

Figure 4.3: Measured and calculated powder diffraction patterns for $LaPO_4$ and $LuPO_4$ nanoparticles. Crystallographic calculations were based on the monazite and xenotime structures[52] for $LaPO_4$ and $LuPO_4$, respectively. Experimental data (circles), calculated profiles (solid line through the circles) are presented together with the calculated Bragg positions (vertical ticks). The difference curve between the measured and calculated profiles is presented as a solid line below.

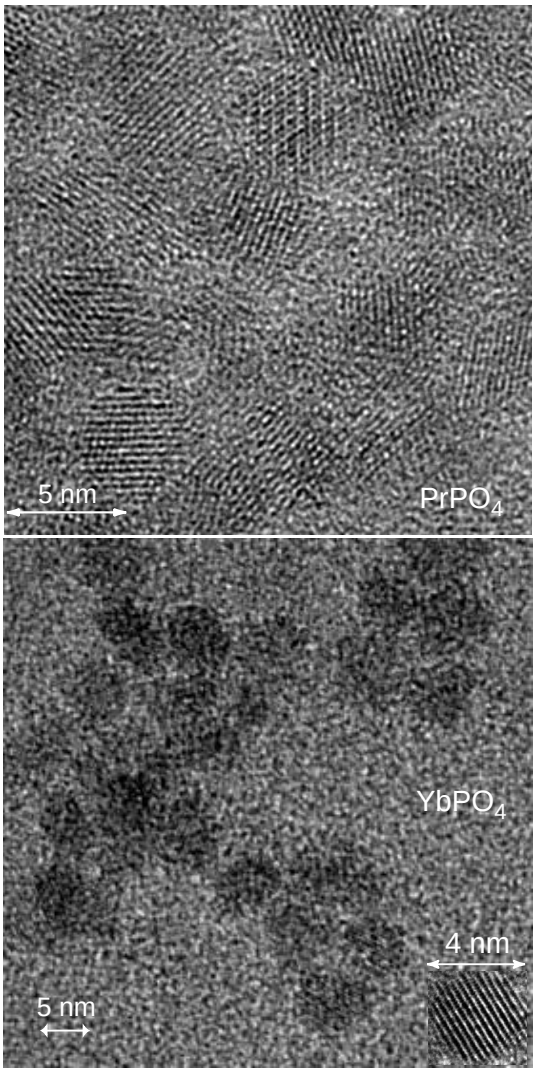

Figure 4.4: High-resolution transmission electron micrographs: top panel of $PrPO_4$ (22 x 22nm^2), bottom panel of $YbPO_4$ (38 x 38nm^2) colloidal solutions. The inset shows an individual $YbPO_4$ nanoparticle. The particles have spherelike morphology and sizes of 3–5 nm.

because the lattice energies of the monoclinic and tetragonal phases close to the phase transition point are very similar, the atoms may occupy surface sites which are in between the monoclinic and tetragonal phases. This leads to a missing short-range order of the atomic arrangements that is fingerprinted in the very broad diffraction peaks. In the last section, we will discuss further the influence of the geometric structure and the "mixed phase" in the electronic structure of the lanthanide orthophosphate nanoparticles.

4.4 Local structural geometry of the crystallites

4.4.1 $4f$ occupancy of the lanthanide ions

$M_{4,5}$-edge X-ray absorption spectroscopy applied on lanthanide ions is reported to be a useful method for studying the ground state $4f$ electron occupancy and $4f$ hybridization state, thus revealing the (mean) valence state of the lanthanide ion [54]. Therefore, we have measured the $M_{4,5}$-edge absorption spectra of lanthanide ions by monitoring the lanthanide MNN Auger lines in a fixed energy window. The results are shown in Fig. 4.5. The absorption spectra originate from the $3d^{10}4f^n \rightarrow 3d^9 4f^{n+1}$ lanthanide transitions. Due to sufficiently deep $3d$ shell, the spin-orbit interaction of the $3d^9$ hole in the final state is much larger than the $3d^9 4f^{n+1}$ exchange interaction. Thus, the final states are split into two group of lines: $3d_{5/2}(M_5)$ and $3d_{3/2}(M_4)$.

The $4f$ electrons in the lanthanides are highly localized (lanthanide contraction) and are shielded from the interatomic interactions by the filled $5s$ and $5p$ outer electronic shells. In the presence of the core hole potential the $4f$ orbitals become stronger localized through the centrifugal barrier. As a consequence, the contribution from the higher empty nf states ($n \geq 5$) in the absorption spectra is suppressed, while the contribution from the higher np empty states is weak due to the low density of these states below the conduction band [53]. Thus, the $M_{4,5}$-edge absorption spectra are due to $3d^{10}4f^n \rightarrow 3d^9 4f^{n+1}$ electronic transitions.

Each individual M_4 and M_5 absorption line shows a considerable multiplet structure. This fine structure is governed by the Coulomb and exchange interaction between the $3d^9$ core hole and the $4f$ electrons (which is strong due to the strong $4f$ shell localization) and the spin-orbit coupling of the core hole and $4f$ electrons (j-j coupling), i.e., the fine structure is due to the intermediate coupling of the $3d^9$ hole and $4f$ electrons in the lanthanide ions. The fine structure

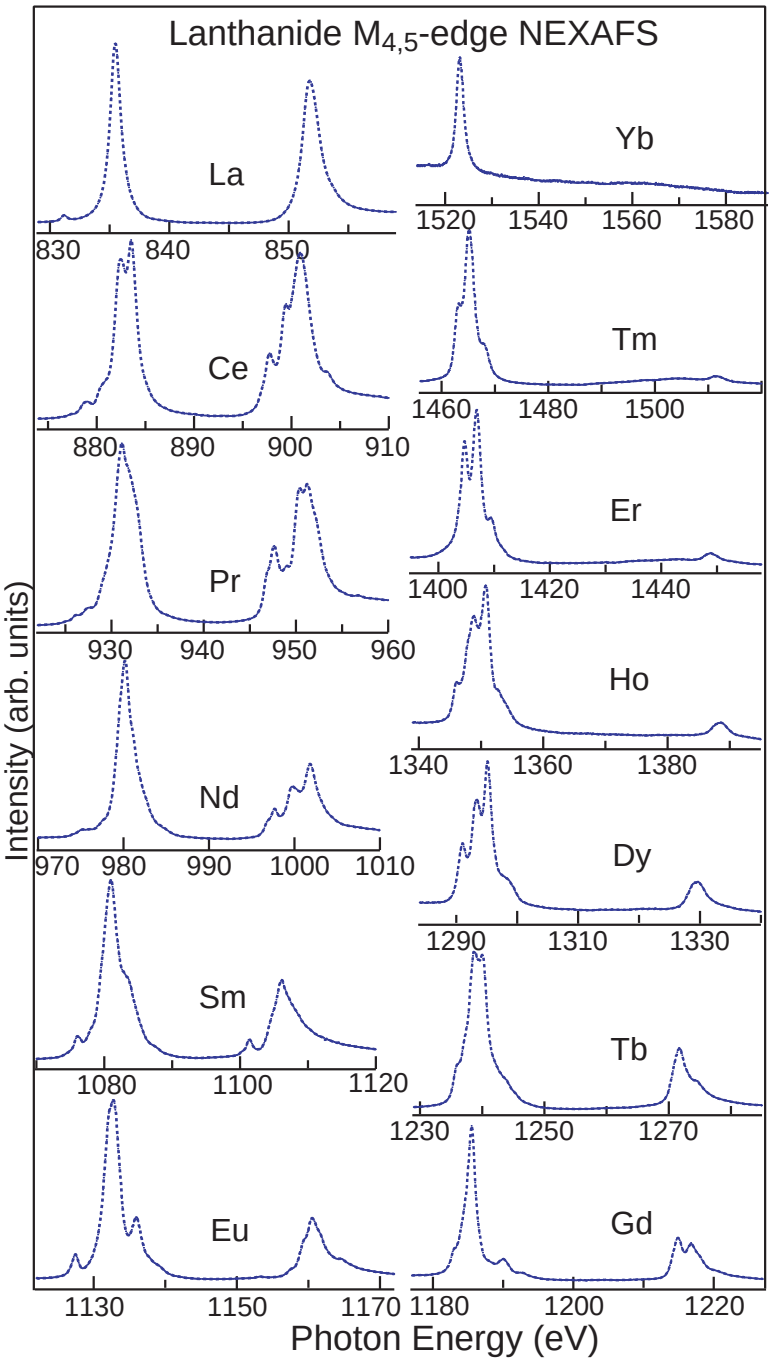

Figure 4.5: $M_{4,5}$-edge NEXAFS spectra of lanthanide ions measured by monitoring MNN Auger lines. Comparison of the characteristic multiplet structure of the spectra to the calculated one by Thole [53] reveal that all rare earth ions are in a triply ionized ground state.

depends on the number of electrons in the $4f$ shell because the spin-orbit interaction between the $4f$ electrons and the exchange interaction between the $3d$ hole and $4f$ electrons will vary as a function of the number of electrons in the $4f$ shell. This will lead to a different fine structure and different intensity ratios between the multiplets. Thus, the fine structure pattern of the $M_{4,5}$-edge absorption spectra is a trace of the electronic configuration of the $4f$ subshell and it reveals the (mean) valence state of the lanthanide ion.

We have compared the fine structure of our lanthanide X-ray absorption spectra with the one reported by Thole *et al.* [53]. They had performed Cowan's atomic multiplet Hartree–Fock calculations with relativistic corrections [19] in the intermediate coupling, i.e., including all the states of the $4f^n$ configuration for the ground state and $3d^9 4f^{n+1}$ final state, for all the lanthanide ions and for all ionization states known in the solid state. The comparisons show that all lanthanide ions in the orthophosphate nanoparticles are in the triply ionized ground state, establishing a $4f$ occupancy in the ground state of $4f^0$ for La till $4f^{13}$ for Yb. In Fig. 4.6 and Fig. 4.7 we have simulated the same calculations performed by Thole *et al.* for cerium and thulium ions.

The calculated spectra are compared with our measured NEXAFS curves. In the case of cerium, an electronic ground state configuration of $4f^1$ is revealed, while for thulium ions an electronic ground state configuration of $4f^{12}$ is revealed. In both cases, theoretical results state a valence of III of cerium and thulium ions in the orthophosphate nanoparticles.

Because our $M_{4,5}$ NEXAFS spectra were recorded in the electron yield mode that allows observation of surface induced valence changes due to its moderate surface sensitivity, we state no surface induced valence changes in the nanoparticles due to their small crystal size.

The total integrated intensity of the M_4 and M_5 absorption lines decreases going from light lanthanides towards the heavier ones because the summed cross section of the two spin-orbit absorption bands is proportional to the number of valence holes [55] and this number reduces going from lighter to the heavier lanthanides. However, the branching ratio of the two spin-orbit split lines $I(M_5)/I(M_4) + I(M_5)$ it is not given by its statistical value $6/4 + 6 = 0.4$. There are two effects that cause the change in the branching ratio [56]. The first effect, is the presence of spin-orbit coupling in the initial state (due to the strong $4f$ localization), that splits the $4f$ valence electrons into bands of different values of the total atomic angular momentum quantum number J (j-j coupling limit), and further the J selection rules set preferences on the transitions to the two different

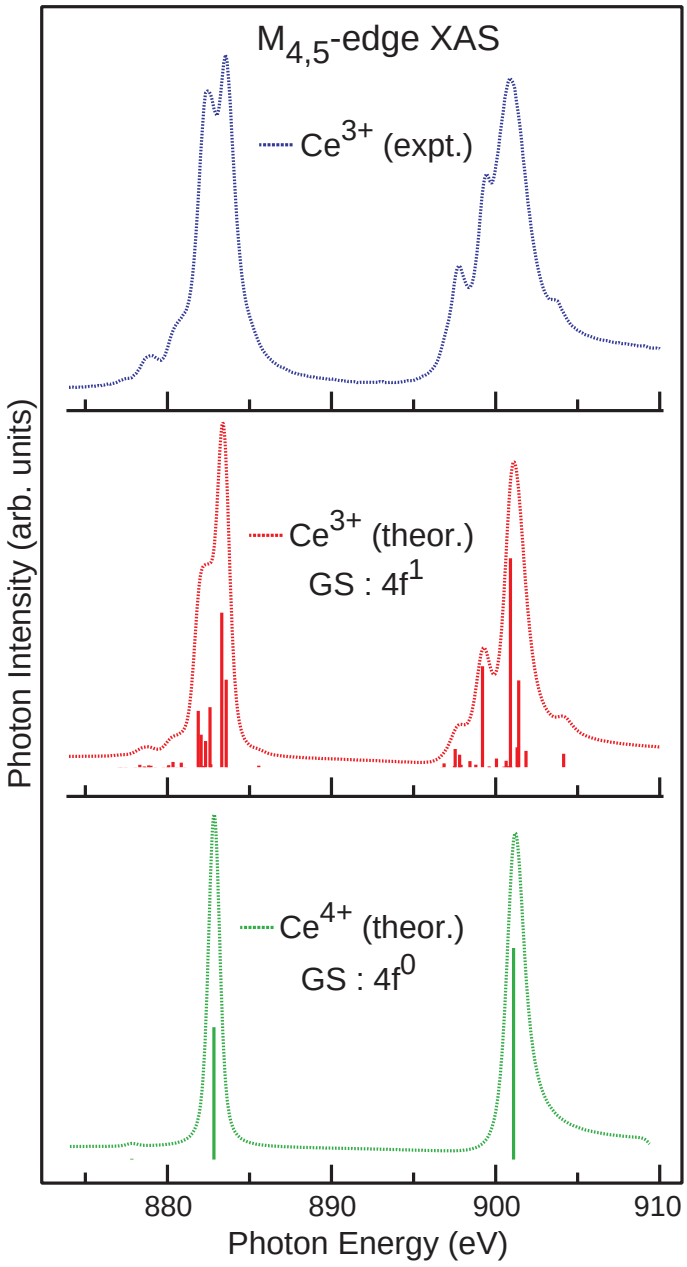

Figure 4.6: Experimental and theoretical spectra of Cerium $M_{4,5}$-edge NEXAFS. Top panel: experimental NEXAFS curve. Bottom panels: atomic Hartree-Fock calculated spectra for ground state configuration $4f^1$ and $4f^0$, respectively.

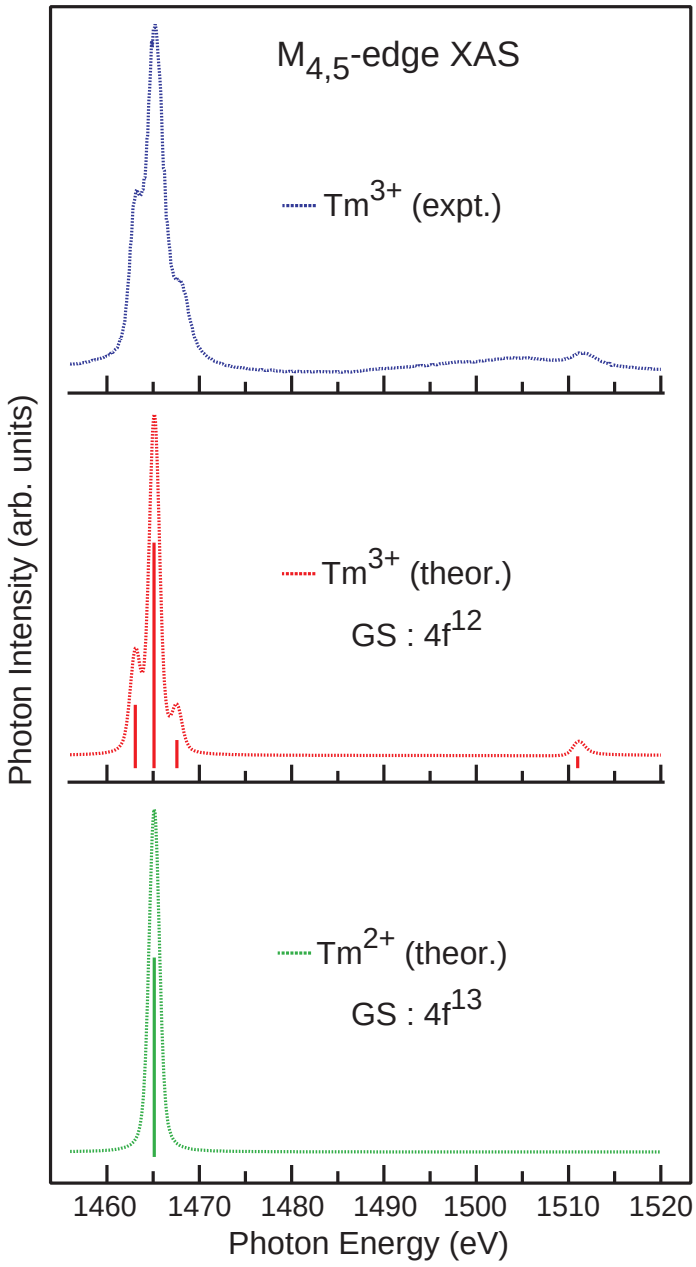

Figure 4.7: Experimental and theoretical spectra of Thulium $M_{4,5}$-edge NEXAFS. Top panel: experimental NEXAFS curve. Bottom panels: atomic Hartree-Fock calculated spectra for ground state configuration $4f^{12}$ and $4f^{13}$, respectively.

manifolds. For this reason, Yb^{3+} absorption spectrum shows only one line, which is due to the fact that the only empty hole in the ground state is in the $^2F_{7/2}$ state so that only the $3d_{5/2} \rightarrow 4f_{7/2}$ transition is allowed. The second effect is the presence of the $3d$ hole-$4f$ electrons electrostatic interactions (L-S coupling) in the final state that couple the core hole to the valence holes differently for the two manifolds [56]. (In the L-S coupling limit, the spin selection rule will play a role in the transitions to the two different manifolds.)

Apart of the different branching ratio between the M_4 and M_5 absorption lines, also a life-time broadening of the M_4 absorption line in comparison to the M_5 line is present, which is due to the Coster-Kronig decay. The M_4 XAS line is considered to be a superposition of the $3d_{3/2} \rightarrow 4f$ transitions and of the weak and continuous XAS due to the $3d_{5/2} \rightarrow$ to conduction band excitations, and the two processes are coupled each other by the Coster-Kronig transitions. The asymmetrical shape of the M_4 absorption line is due to the Fano resonance [30].

4.4.2 Lanthanide - Oxygen covalency within the series

In the following section, we will discuss the unoccupied valence electronic structure of the nanoparticles and examine its interplay with the particle's crystal size and crystal phase. For this purpose, the oxygen K-edge NEXAFS of all lanthanide nanoparticles is investigated, which is sensitive to the geometrical arrangement in the vicinity of the oxygen atom, and it gives information on the chemical bonding and the effective charge density around the oxygen atom. The oxygen K-edge NEXAFS spectra of the whole lanthanide phosphate series (with exception of Ho) are shown in Fig. 4.8. The spectra are corrected for the background signal by subtracting the clean silicon substrate spectrum. NEXAFS signal correction in the case of $EuPO_4$ sample is shown in Fig. 4.9.

After background subtraction, all the spectra are normalized to the intensity at about $40eV$ above the absorption edge. The spectra consist of several peaks: the strong and broad peak located at 538eV denoted as A, followed by the weak feature as B, and the very broad shape resonance peak as C.

In order to discuss the origin of the different spectral features, we need to inquire into the band structure of lanthanide phosphates. In both monoclinic and tetragonal structures, the oxygen ions coordinate to two lanthanide ions and one phosphor ion. The oxygen-phosphor bonding is reported to be strongly covalent in the PO_4 units and their conduction band consists of broad O $2p$ projected density of states hybridized with P $3p$ projected density of states [57–59].

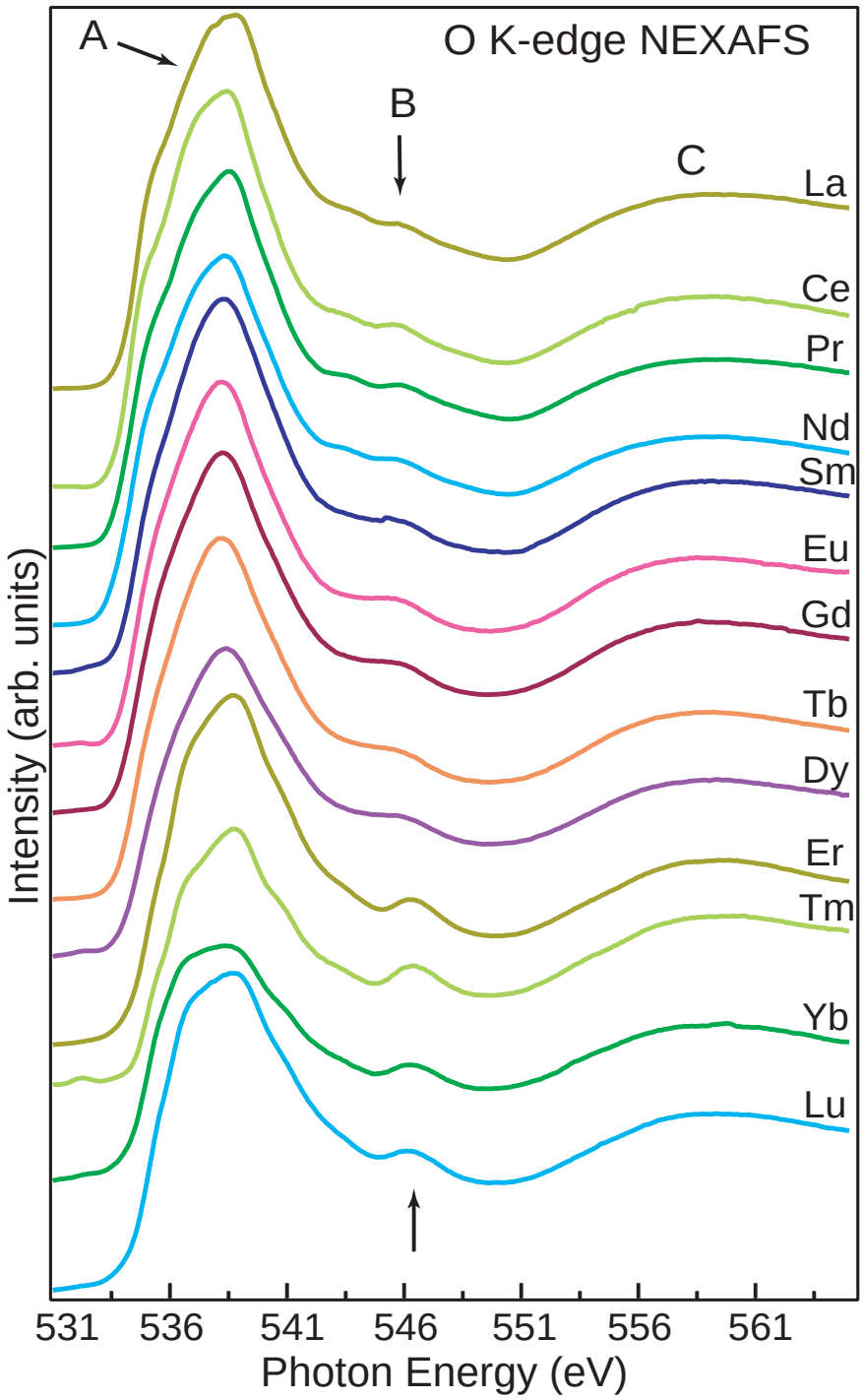

Figure 4.8: Oxygen K-edge NEXAFS spectra of lanthanide phosphate nanoparticles. Peaks A and B are due to Ln-O covalent bonding. The difference in their spectral shapes across the series is due to different geometric structure, coordination number and particle morphology. Peak B shifts towards higher energies and strengthens across the series indicating stronger covalency.

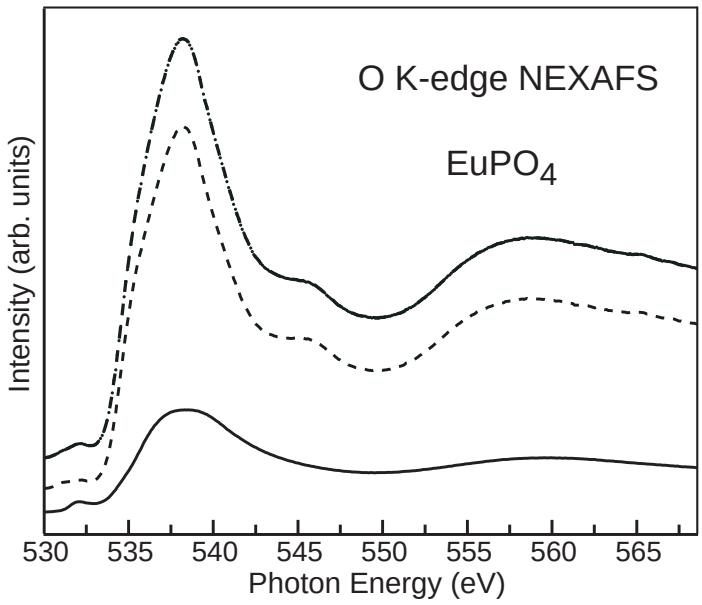

Figure 4.9: O K-edge NEXAFS spectra of: Si substrate – the solid line, $EuPO_4$ nanoparticles on the Si substrate – the dashed circle line, and the $EuPO_4$ nanoparticles subtracted the Si substrate signal – the dotted line.

In the case of the lanthanides, the $4f$ orbitals are strongly localized inside the atom and surrounded by the filled $5s$ and $5p$ orbitals that have larger radial extension. As a consequence, the $4f$ orbitals do not take part in the bonding. Thus, the lowest unoccupied density of states in the lanthanide ions consist of $5d$ character with $6s$ and $6p$ contribution [53]. Hence, the strong broad peak A can be assigned to transitions from O $1s$ to empty O $2p$ projected density of states hybridized with Ln $5d$ and P $3p$ projected density of states. Based on molecular-orbital theory, Grioni *et al.* and de Groot *et al.* [60, 61] calculated the O $2p$ orbitals to be spread over a high energy range above the Fermi level (up to 20 eV) in the transition metal oxides. They concluded that the pre-edge absorbtion peak is due to the hybridization of the antibonding $2p$ orbitals with metal $3d$ orbitals, and the absorption features located 5-10eV above the oxygen threshold have $2p$ character hybridized with metal $4s$ and $4p$ orbitals. Proceeding under this assumption, we attribute the next peak B to the hybridization of O $2p$ density of states with the upper-lying unoccupied density of states of Ln and P. In the case of lanthanide ions, the next upper-lying unoccupied density of states are $6s$ and $6p$ states [53, 62]. Thus, the spectral feature B in the NEXAFS spectra

is due to O 1s to 2p projected density of states hybridized with the Ln 6s and 6p and P 3p density of states.

The same conclusions on the oxygen peak assignment were reached by Wu *et al.* based on *ab initio* one-electron full multiple-scattering (MS) calculations, i.e., considering the scattering of the outgoing photoelectron wave from the charge density close to the photoabsorber oxygen ion. They have performed calculations of the O K-edge NEXAFS spectra of Ba_2TiO_4 [62] that has monoclinic symmetry and of rutile TiO_2 [63] crystal that has a tetragonal symmetry.

In the following, we would like to discuss the spectral shape variation of peaks A and B within the lanthanide series. The spectral shape difference of the peak A in the monoclinic and tetragonal nanoparticles can be attributed to their different crystal structures [61] and coordination numbers. Bearing in mind the geometric structure discussion of the previous section, in the monoclinic structure one lanthanide ion is coordinated to nine oxygen ions, while in the tetragonal structure, it is coordinated to eight ions. Due to the less regular LnO_9 polyhedra, the oxygen atoms accommodate in four different sites and show nine unique Ln-O atomic distances in the monoclinic structure compared to only one oxygen site and four unique Ln-O atomic distances in the tetragonal structure. Exact assignment of each subfeature would require detailed band structure calculations and is out of the scope of this paper.

The spectral feature B becomes more intense and locates at relatively higher energies going from $LaPO_4$ nanoparticles of the monoclinic phase toward the $LuPO_4$ nanoparticles. These facts reveal that the hybridization of O 2p unoccupied density of states with Ln 6s and 6p unoccupied density of states is stronger in the tetragonal phase, thus, displaying stronger covalency between oxygen and lanthanide atoms in the tetragonal phase. Indeed, covalency reduces the number of filled states with O 2p character so that the strength of the oxygen K-edge signal in the NEXAFS spectra is related to the degree of covalency. This conclusion is in agreement with the crystallographic data [52] stating that the interatomic distance between lanthanide and oxygen atoms decreases going from monoclinic to tetragonal phase.

Finally, we want to discuss the width evolution of the spectral features A and B across the series. It can be seen from Fig. 4.8 that the spectral shapes of features A and B broaden at the intermediate lanthanide ions. For explaining this behavior, we recall here the discussion about the particles size and their short-range order of the previous section. We mentioned that the particles of the monoclinic and tetragonal phase exhibit a mean-crystal size of 3–5nm, with

a surface to bulk contribution of ∼50%. This causes a degree of disorder in the nanoparticle structure and respectively in the oxygen and lanthanide sites that results in broadening of the spectral shapes. The lanthanide nanoparticles from the middle of the series crystallize in even smaller size (∼2nm) and have a more distorted geometry that results in the "mixed phase" of these nanoparticles. This increases the degree of disorder, and consequently, the number of oxygen and lanthanide sites in the nanoparticles and therefore the spectral shape of features A and B broadens further.

4.5 Conclusions

The evolution and interplay of the geometrical and electronic structures of lanthanide orthophosphate nanoparticles have been determined across the lanthanide series. The larger (La, Ce, Pr, Nd, Sm) and smaller (Er, Tm, Yb, Lu) lanthanide ions crystallize in the monoclinic and tetragonal phases, respectively, as their bulk crystals and exhibit particle sizes of ∼3–∼5nm. The intermediate lanthanide ions (Eu, Gd, Tb, Dy, Ho) show a very small particle size of ∼2nm and crystallize in a "mixed phase" between monoclinic and tetragonal phases, induced by their large surface contribution and their ionic radii. The $M_{4,5}$-edge NEXAFS measurements established that all the lanthanide ions in the lanthanide phosphate nanocrystals are in a "3+" configuration state. From the oxygen K-edge NEXAFS, we accessed the covalent bond involving the phosphate oxygen atoms towards the lanthanide ions. We tracked this covalency as a function of lanthanide ion, its coordination number to oxygen, and site symmetry. We showed that there is a stronger covalency between oxygen and lanthanide ions in the tetragonal phase compared to the monoclinic phase. The increased surface contribution and the missing of short-range order in the intermediate lanthanide nanoparticles was accompanied by broad spectral shapes in oxygen K-edge NEXAFS and concomitant multiple oxygen and lanthanide sites. [2]

[2] **Acknowledgments**

We owe special thanks to Frank de Groot for helpful discussions. We greatly acknowledge the contributions of Kerstin Rücker on synthesizing and characterizing the nanoparticles, of Andrea Kornowski on SEM investigations, and of Karsten Kömpe on TEM investigations of the nanostructures. We thank the scientific and technical staff of Bessy II and Hasylab for assistance.

This work was supported by the Graduiertenkolleg project: "Spektroskopie an lokalisierten atomaren Systemen, Felder und lokalisierte Atome–Atome und lokalisierte Felder" and the

DFG Sonderforschungsbereich 508 “Quantenmaterialien–laterale Strukturen, hybride Systeme und Cluster.

Chapter 5

Physical states correlation and their influence on the spectral shapes of La

[1] In the Hartree-Fock model of calculating the ground and final excited states energies (elaborated in section 3.1) the independent electron approximation with the partial account for the electron spin-orbital correlation leads to a correlation energy. Additionally, in the final states of the XAS and RIXS processes, the core excited final state and the valence hole ionic final state, respectively, can lead to a modification of the other orbitals in the atom. This perturbation is not considered within the single electron approximation and will give rise again to a correlation energy of the final states. If the correlation effects are too strong, the single configuration Hartree-Fock calculation does not adequately calculate the energies of the final states. This implies that a number of resonance states of different configurations can lie close in energy or overlap with each other, giving rise to configuration mixing or configuration interaction (CI) [30]. In the X-ray absorption process mixing of the configurations is accompanied with the coherent populations of different physical states (that lie at the same energy) which give rise to the so called "interference effects" and Fano spectral profiles [30].

The most fundamental correlation phenomenon is the autoionization process that occurs for all many electron atoms in highly excited configurations which lie above the first ionization threshold [30, 33, 64]. This gives rise to discrete excitations embedded in the continuum states and consequently to the interference of

[1] Paper in manuscript. This section is intended for publication to PRL: Suljoti, Föhlisch, de Groot, Nagasono, Glatzel, Hennies, Deppe, Pietzsch, and Wurth.

the discrete autoionized state with the direct photoexcitation into the continuum state.

Another aspect of many body problem is the correlation in the final continuum states, giving rise to photoionization interchannel coupling [65]. This phenomenon is particularly important in the photoionization process near the threshold regions [66], but recently it has been understood that interchannel coupling is significant even at intermediate and high photoelectron energies as well [67, 68]. In addition, it has recently been found that the weak spin orbit interaction activates interchannel coupling of the doublet states which not only induces new structures in the photoionization cross section [69] but also produces significant changes in the photoelectron angular distribution as well [70].

A different aspect of correlation effects arises in the case of tight bound core excited states where the interaction of the core hole with the excited electron is strong. This is particularly significant for core hole states in the outer shells and implies that the physical states involve a degree of correlation. A weak spin orbit interaction can mix core excited states of different symmetries and hence, decay processes from the correlated core excited states lead to interference effects and asymmetrical spectral profiles. In addition, the large lifetime broadening of the excited states can entangle further the spectral profiles by an addition mixing of the close-lying physical states through the intermediate state coherence (lifetime interference). This is exactly the case of lanthanide 4d resonances. Due to the localization of 4f unoccupied valence states, the Coulomb interaction of the core hole with 4f electrons is very strong and results in strong multiplet effects. Thus, the absorption spectra consist of many sharp pre-resonances followed by the giant resonance. These pre-resonances are all mixed symmetry states due to the small spin orbit interaction of the 4d core hole. In addition, these states are mixed with the broad giant resonance state ($\sim$ 9eV). Thus, the complete understanding of the spectral profiles is a very demanding task.

A model ideally suited to disentangle these phenomena is La 4d XAS spectrum. Lanthanum has no electron in the 4f shell, so its 4d XAS consists of only two pre-resonances and the giant resonance. This simplifies the problem tremendously. Thus, in this chapter in the model system of La, the influence of the correlated intermediate states and lifetime interference on the absorption spectra is studied. The spectral profile difference between total electron yield and total fluorescence yield will be investigated as well. The resonant inelastic X-ray measurement and theoretical calculations will emphasize the role of electron cor-

relation in the final ionic states and the symmetry aspects of radiative decay in the fluorescence profiles.

5.1 Experimental

Lanthanum phosphate nanoparticles, capped by organic ligands were chemically prepared in liquid-phase synthesis [16]. They had a mean-size of 3-5nm and high crystallinity [71]. From solution of $LaPO_4$ nanoclusters, thin films on hydrogen-passivated Si(100) surfaces were prepared. Details on thin film preparation and characterization are given in our previous work [71]. Experiments were performed on our UHV Hamburg Inelastic X-ray Scattering (HIXS) experimental station that is equipped with a hemispherical photoelectron analyzer and a soft X-ray emission spectrometer (XES), using the synchrotron radiation beam at the Bessy II (Berlin), UE52-PGM beamline. XAS spectra were measured in TEY mode by monitoring the sample current and in TFY mode by monitoring zero order light in the XES spectrometer. The synchrotron beam was incident at an angle of 7° to the surface plane. The photons were linearly polarized with their polarization vector perpendicular to the sample plane. The XES-spectrometer detected radiative RXS signal 7° off the electric field vector of the incident radiation. Resolving power $E/\Delta E$ of the incoming photon beam was 2000 at 140eV, and of the scattered beam in XES spectrometer was 715 at 100eV.

5.2 La $N_{4,5}$-edge electron and fluorescence yield

The $N_{4,5}$ edge X-ray absorption spectrum of triply ionized La ions in $LaPO_4$ nanoparticles is shown in Fig. 5.1. It consists of two weak and sharp $^3P_1$ and $^3D_1$ pre-resonances, and the strong and broad $^1P_1$ giant resonance.

In the ground state La^{3+} ions are in the $4d^{10}5s^25p^64f^0$ electronic configuration of $^1S_0$ symmetry, and the resonances arise from exciting a $4d$ electron in the empty $4f$ shell through the $4d^{10} \rightarrow 4d^94f^1$ electronic transition. According to the dipole selection rules the radiative transition will populate the excited state of $^1P_1$ symmetry;

$$\mathbf{^1S_0} \overset{V_r}{\Longrightarrow} \mathbf{^1P_1}$$

where, V_r stands for the dipole transition. The large radial overlap of the $4d$ and $4f$ wavefunctions (please refer to the calculated Slater-Condon parameters in Table 5.1), results in large transfer of oscillator strength to the fully allowed

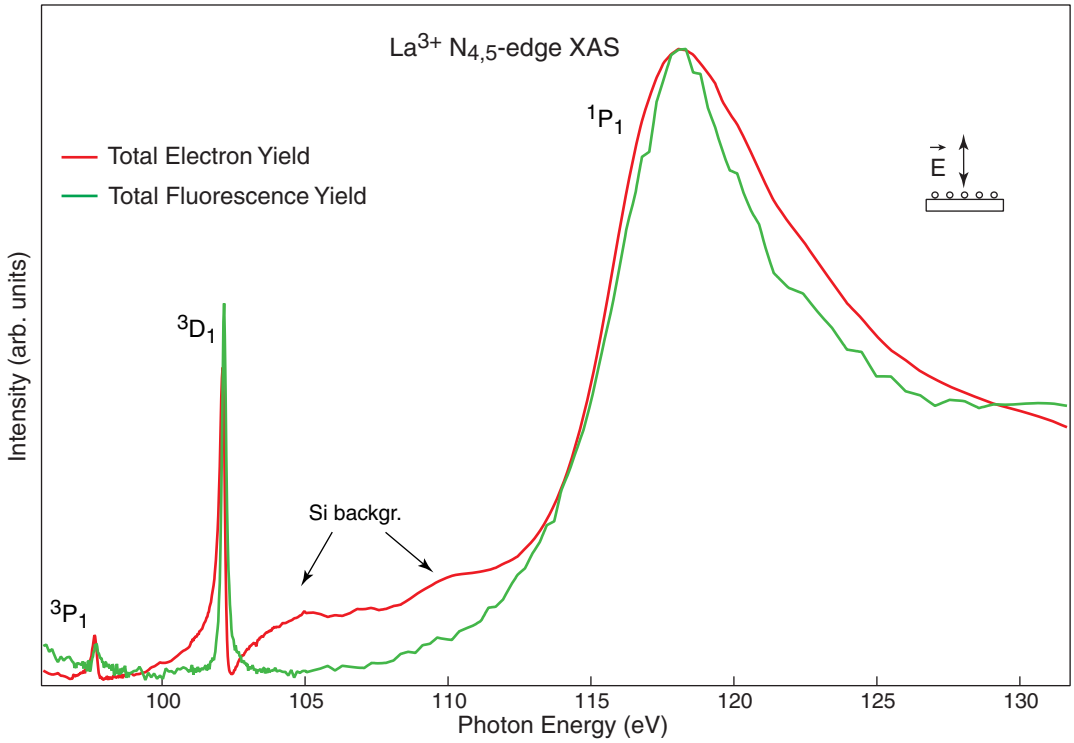

Figure 5.1: The measured La $N_{4,5}$ XAS spectra of $LaPO_4$ nanoparticles of 3-5 nm diameter spin coated as thin films on Si substrates. Sample geometry: The synchrotron beam was incident at an angle of 7° to the surface plane. The photons were linearly polarized with their polarization vector perpendicular to the sample plane.

singlet $^1P_1$ state. This is the reason why this state has a large cross section (please refer to the calculated transition intensities in Table 5.2) and exhibit itself in the experimental measurements in a very strong spectral peak.

Table 5.1: The calculated Slater-Condon parameters and spin-orbit coupling of La^{3+} $4f^0$ ground state, and $4d^9 4f^1$ excited state.

	Slater-Condon parameters (eV)					Spin-Orbit coupling (eV)	
	G_1	G_3	G_5	F_2	F_4	$(l \cdot s)_{4d}$	$(l \cdot s)_{4f}$
$4f^0$	0	0	0	0	0	0	0
$4d^9 4f^1$	12.418	7.735	5.454	10.454	6.660	1.117	0.077

Table 5.2: The calculated energies, purities, and the intensities of the La^{3+} $4d^{10}4f^0 \rightarrow 4d^9 4f^1$ transition states.

Eigenvector	Purity in LS scheme	Eigenvalue (eV)	Intensity
$^3P_1$	0.95	98.748	0.00065
$^3D_1$	0.95	102.942	0.00577
$^1P_1$	0.99	124.472	1.99359

In addition, the weak spin orbit interaction of the $4d$ core hole mixes the pure $^3P_1$ and $^3D_1$ states (of total angular momentum $J = 1$) with the strong $^1P_1$ state, and the spin forbidden transitions;

$$\mathbf{^1S_0} \xrightarrow{V_r} \mathbf{^3P_1}, \mathbf{^3D_1}$$

become partially allowed and give rise to the weak and sharp $^3P_1$ and $^3D_1$ pre-resonances observed in the experimental absorption spectrum. The $^3P_1$, $^3D_1$ and $^1P_1$ states do not indicate pure $^{2S+1}L_J$ states, but refer to states that are a linear combination of these three $J = 1$ states. The two small $^3P_1$ and $^3D_1$ pre-resonances are both 95% pure, and 5% of their intensity is given by the other symmetries. For the $^3P_1$ state, the $^1P_1$ symmetry contribution is 1.5%, and for the $^3D_1$ state is 4.3%. The percentage $^1P_1$ symmetry character determines

the intensity of the pre-resonances. Because the $^3P_1$ state has less $^1P_1$ symmetry contribution, its spectral peak evidenced very small intensity in the measured XAS spectra. In addition, the strong direct and exchange Coulomb interaction of the $4d$ core hole with the excited $4f$ electron give rise to strong multiplet effects that push the $^1P_1$ state (located at 118.5 eV) above the $4d$ ionization threshold (at 110 eV with respect to the bottom of conduction band). While, spin forbidden $^3P_1$ and $^3D_1$ states are located below the $4d$ ionization threshold, at 97.7 eV and 102.17 eV, respectively.

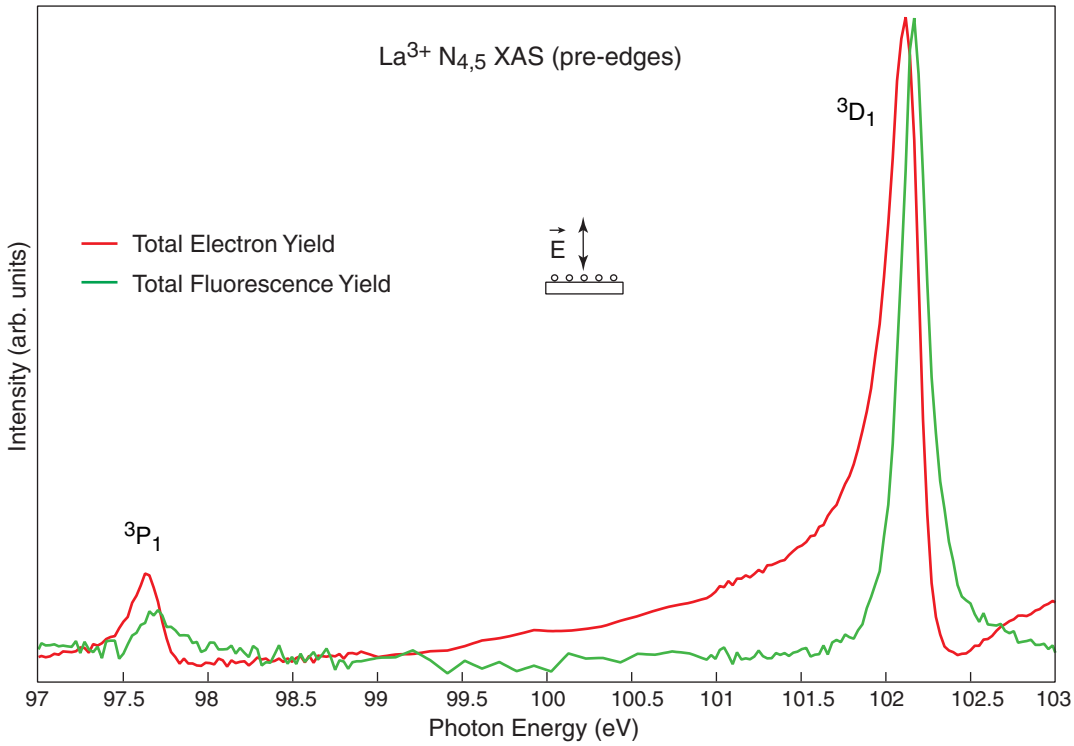

Figure 5.2: $^3P_1$ and $^3D_1$ resonances of La $N_{4,5}$ XAS spectrum measured in $LaPO_4$ nanoparticles of 3-5 nm size. TEY spectrum reveals asymmetric line profiles of both resonances, compared to symmetric profiles of the TFY.

In Fig. 5.2 the pre-edge region of the experimental XAS spectrum is shown. One distinguishes the very asymmetrical profile of $^3D_1$ electron yield spectrum, with a long tail on the low energy flank, toward the symmetric Lorentzian fluorescence profile. Besides, the $^3D_1$ electron yield resonance is shifted toward lower energies compared to the fluorescence yield resonance. In the case of the $^3P_1$ res-

onance, the asymmetrical spectral profile is still visible, but it is less pronounced than $^3D_1$ due to its smaller intensity.

The spectral shape asymmetries and the energetic shift of the resonance's maximum are "fingerprints" for interference effects in the nonradiative decay channels and in the following section we will discuss them.

5.3 Nonradiative decay processes of the $^3D_1$ and $^3P_1$ resonances

The nonradiative Raman scattering experiments performed at the $^3P_1$ and $^3D_1$ resonances [72–74] report for these states to decay through the participator process (also referred as resonant photoemission process). The participator decay occurs mainly because the excited $4f$ electron is quite localized at the $^3P_1$ and $^3D_1$ states and it interacts strongly with the $4d$ core hole and hence it decays by direct recombination (involving the excited electron and the core hole) and giving the excess energy to a $5s$ or $5p$ electron:

$$4d^{10}4f^0 \xrightarrow{V_r} 4d^9 5p^6 5s^2 4f^1 \xrightarrow{V_c} \begin{cases} 4d^{10}5p^5 5s^2 4f^0 \varepsilon_{s,d} \\ 4d^{10}5p^6 5s^1 4f^0 \varepsilon_p \end{cases} \tag{5.1}$$

In addition to the resonant photoemission process also the direct photoionization of the $5p$ and $5s$ electrons occurs:

$$4d^{10}5p^6 5s^2 4f^0 \xrightarrow{V_r} \begin{cases} 4d^{10}5p^5 5s^2 \varepsilon_{s,d} \\ 4d^{10}5p^6 5s^1 4f^0 \varepsilon_p \end{cases} \tag{5.2}$$

Both processes, the direct and resonant photoemission reach the same final states;

$$\mathbf{^1S_0} \xrightarrow{V_r} \mathbf{^3P_1, {}^3D_1} \xrightarrow{V_c} \begin{cases} \mathbf{^2P_{1/2}, {}^2P_{3/2}} \\ \mathbf{^2S_{1/2}} \end{cases} ; \qquad \mathbf{^1S_0} \xrightarrow{V_r} \begin{cases} \mathbf{^2P_{1/2}, {}^2P_{3/2}} \\ \mathbf{^2S_{1/2}} \end{cases}$$

going through two different paths as depicted in Fig. 5.3. The interference of these two processes would lead to the so-called Fano resonances [30] characterized by asymmetrical lineshapes. This would explain the spectral profile difference between the electron and fluorescence yields, because in the later one the direct channel is missing.

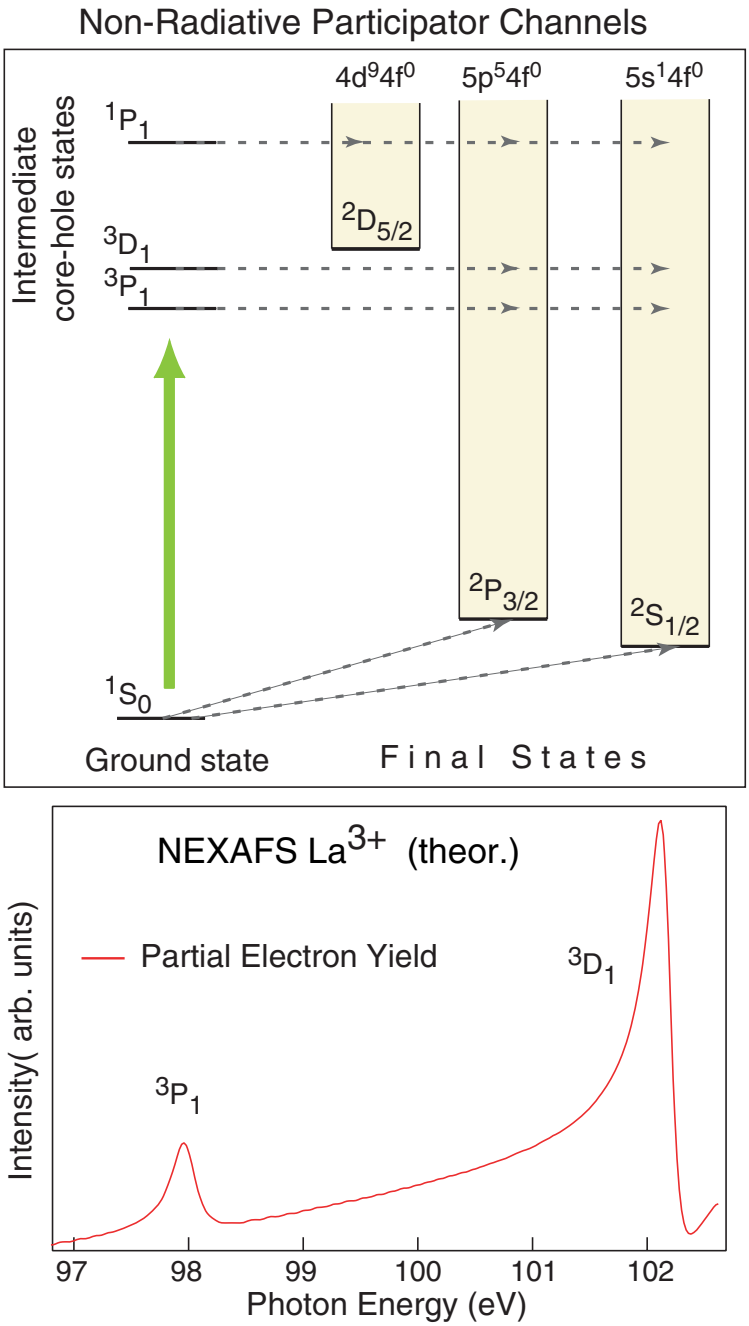

Figure 5.3: Top: The sketch of nonradiative decay channels of the resonantly excited $^3P_1$, $^3D_1$, and $^1P_1$ states. The $^3P_1$ and $^3D_1$ states interact with $5p^5\varepsilon$ and $5s^1\varepsilon$ continua and decay through the participator process. In addition, the direct $5p$ and $5s$ photoemission process also occurs. Bottom: Calculated resonant $5p$ photoemission yield spectrum at $^3P_1$ and $^3D_1$ resonances.

To confirm the above idea we calculated the intensity of nonradiative Raman scattering process using Kramers-Heisenberg formulation:

$$w_{f0} = 2\pi \sum_f \left| \langle f|V_r|0\rangle + \sum_i \frac{\langle f|V_c|i\rangle\langle i|V_r|0\rangle}{E_0 + \hbar\omega - E_i + \frac{i\Gamma_i}{2}} \right|^2 \cdot \delta(E_0 + \hbar\omega - E_f) \qquad (5.3)$$

The first part of the matrix element represents the direct photoemission and the second part represents core hole assisted channels (excitation-deexcitation channels). The initial state (0) and final state (f) wavefunctions contain the incoming photon and outgoing electron, respectively, while (i) denotes the intermediate core excited states, that in our case are $^3P_1$ and $^3D_1$ states. The radial wavefunctions and energies of the initial state, core excited intermediate states and the final electron states were calculated using Cowan's relativistic Hartree-Fock code [19]. All atomic parameters were scaled to 80% to include the effects of configuration interaction. The details of Hartree-Fock method are given in chapter 3. The energy scale of the calculated spectra were shifted with -1.26 eV to correspond with the measured spectra. V_r and V_c stand for radiative and Coulomb operators, respectively. Γ_i is the spectral broadening due to the core hole lifetime of the intermediate state i. In our calculations, we used $\Gamma_i = 0.14$ eV for both $^3P_1$ and $^3D_1$ states, that were deduced from the full width at half maximum (FWHM) of the experimental electron yield spectra. The δ function ensures energy conservation. In addition, the spectra were convoluted with a Gaussian of 70 meV FWHM, that was the width of the incident photon energy.

The calculated spectra exhibited the Fano anti-resonance behavior with the long tail on the lower energy flank of both resonances and resembled very well the measured spectra. Besides, we found out that if we disregard the direct photoemission process in the calculations i.e., consider only the resonant photoemission process, the asymmetry of the spectral profiles is preserved. In Fig. 5.3, we have shown the results of resonant photoemission (5.1) calculations with a $5p$ hole in the final state. Thus, these results emphasize that the spectral asymmetry of $^3P_1$ and $^3D_1$ resonances is not due to interference of the direct and resonant photoemission channels.

In agreement with our results, Mishra *et al.* [75] has reported that the interference of these two processes does not occur at the lanthanides $4d$ pre-edges due to the absence of phase coherence. Namely, the Coster-Kronig decay of the weak core excited pre-resonances is much slower than the fast direct photoemission process, leading to a violation of the temporal match requirement for channel interference.

In order to inquire into the reasons for the asymmetrical lineshape of the pre-resonances, we recall here the results of Hartree-Fock calculations. We found that $^3P_1$ and $^3D_1$ core excited states are not pure $^{2S+1}L_J$ states but are mixed at different percentage with the dipole allowed $^1P_1$ state. Accordingly, the $^3D_1$ state consist of pure $^3D_1$ and $^1P_1$ symmetry contribution. Therefore, the resonant photoemission scattering amplitudes of these two contributions (pure $^3D_1$ symmetry and pure $^1P_1$ symmetry) will interfere. Note that although the symmetry contribution of the $^1P_1$ state at the $^3D_1$ and $^3P_1$ resonances is very small (4.3% and 1.5%, respectively), the scattering amplitudes of both processes become comparable due to the strong dipole allowed $^1P_1$ state. As a consequence there is a strong interference of both resonant photoemission processes, that leads to a non-exponential nonradiative decay exhibited with an asymmetrical spectral shape of the electron yield.

5.4 Radiative decay processes of the $^3D_1$ and $^3P_1$ resonances

Next, we raise the question: What about interference effects in the fluorescence yield? Why don't we observe its fingerprint: asymmetrical spectral profile?

To answer these questions we performed resonant X-ray scattering (RXS) experiments with highly selective resonant and detuned excitation across the $^3D_1$ and $^3P_1$ resonances and monitored the concomitant radiative decay over a large energy loss range from ∼25 eV to 0 eV. This includes the $4d4f$ (valence band) resonant elastic X-ray scattering (REXS) and the 4d5p resonant inelastic X-ray scattering (RIXS). In Fig. 5.4 (panel 2), we show the experimental 4d5p RIXS spectra beside the excited energy along the resonances. Detuning along the $^3D_1$ resonance, we observe an extreme resonant behavior of the $^3D_1$-$^3D_2$ emission peak, while for the $^3F_2$ and $^1D_2$ emission lines we do not observe it. (Note that our X-ray spectrometer could not resolve the $^3D_1$ and $^3D_2$ emission lines.) Being more precise, the $^3F_2$ emission line reaches its maximum at the low energy flank of the $^3D_1$ resonance and the $^1D_2$ emission line reaches its maximum at the high energy flank of the $^3D_1$ resonance. This peak intensity behavior across the $^3D_1$ resonance recalls for interference effects between the radiative decay channels and we used again the Kramers-Heisenberg formalism to calculate the amplitudes and the intensities of the different radiative channels.

The observed RIXS emission lines in the experimental data are due to the

$$4d^9 5p^6 4f^1 \xrightarrow{V_r} 4d^{10} 5p^5 4f^1$$

radiative transitions, where V_r stands for radiative transitions. RIXS processes are assisted by dipole selection rules that dictate the symmetries of the final ionic states. The main final states reached for the three core excited intermediate states are:

$$\mathbf{^3P_1} \xrightarrow{V_r} \mathbf{^3D_2}, \mathbf{^3D_1}$$
$$\mathbf{^3D_1} \xrightarrow{V_r} \mathbf{^1D_2}, \mathbf{^3F_2}, \mathbf{^3D_2}, \mathbf{^3D_1}$$
$$\mathbf{^1P_1} \xrightarrow{V_r} \mathbf{^1D_2}, \mathbf{^3F_2}$$

The calculated energies and the intensities of the upper transitions are given in Table 5.4 and Table 5.5, respectively. It can be seen from the tables that $^1D_2$ and $^3F_2$ final states have both less than 1% of the overall transition strength for the $^3P_1$ core excited state and $^3D_2$ and $^3D_1$ final states have less than 0.5% transition strength for the $^1P_1$ state. Thus, the energy coherence is broken for some of the radiative decay channels because not all final states are reached from each intermediate core excited state. As a consequence, we will have less interfering channels in the radiative decay compared to the nonradiative decay. Accordingly, both $^3D_1$ and $^1P_1$ intermediate states decay to the $^1D_2$ and $^3F_2$ final states. This implies that the coherent radiative scattering from the $^3D_1$ and $^1P_1$ symmetry contributions of the correlated $^3D_1$ state (mixed of pure $^3D_1$ and $^1P_1$ symmetries) to the $^1D_2$ final state will interfere. The same is valid for the $^3F_2$ final state.

Table 5.3: The calculated Slater-Condon parameters and spin-orbit coupling of La^{3+} $4d^{10}5p^5 4f^1$ core ionic final states.

Slater-Condon parameters (eV)				Spin-Orbit coupling (eV)		$E_{average}$
	G_2	G_4	F_2	$(l \cdot s)_{5p}$	$(l \cdot s)_{4f}$	
$4d^{10}5p^5 4f^1$	3.028	2.262	4.925	1.543	0.065	20.519

From Kramers-Heisenberg RIXS calculations results that at the $^3D_1$ resonance, the amplitudes of the $^1D_2$ scattering channels have opposite signs, while the amplitudes of the $^3F_2$ scattering channels have the same sign. This implies that the $^1D_2$ emission line have destructive interference below the $^3D_1$ resonance

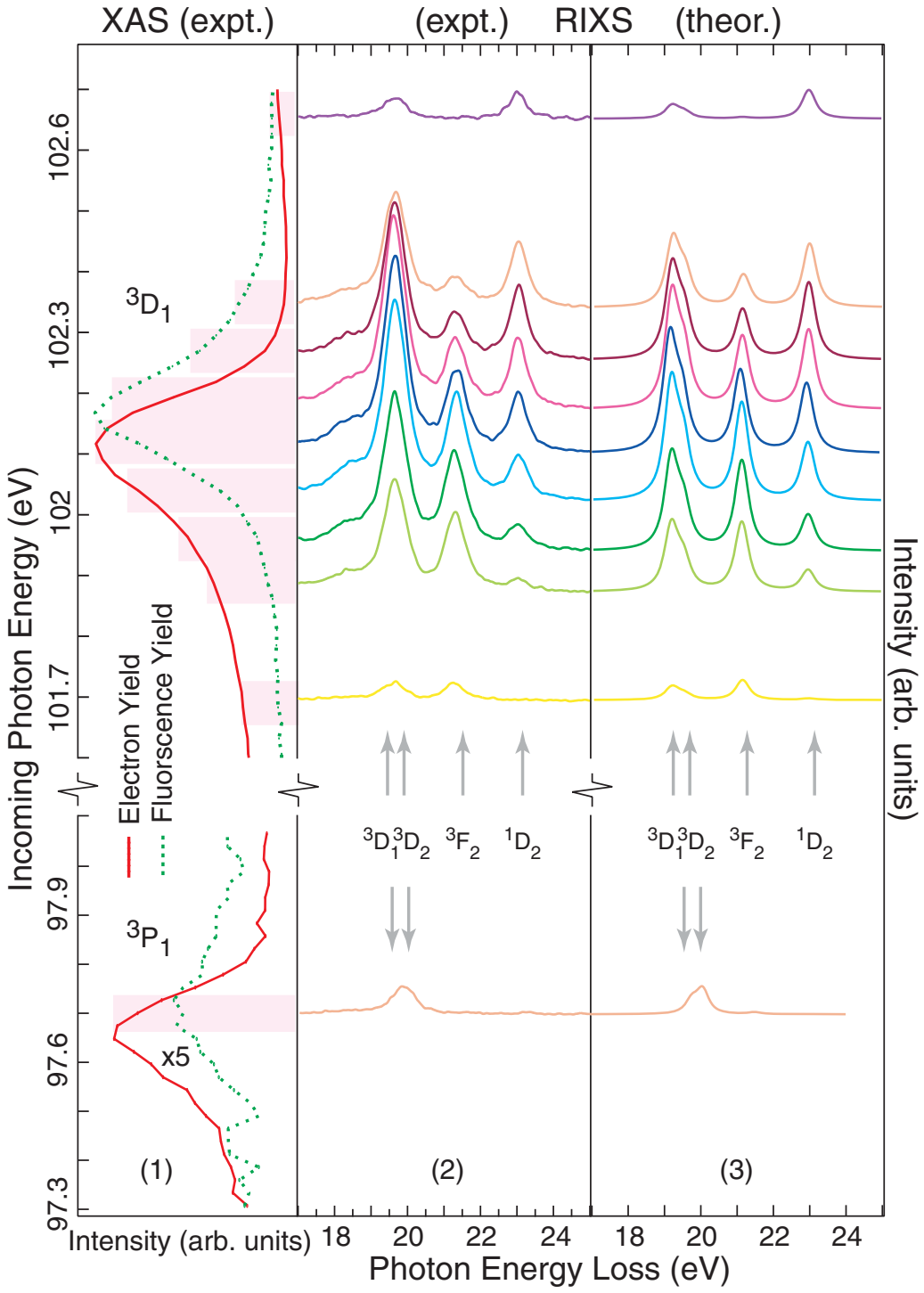

Figure 5.4: A series of experimental and theoretical RIXS spectra across the $^3D_1$ and $^3P_1$ resonances. 1) Total electron and fluorescence yield of the resonances. XAS spectrum of the $^3P_1$ resonance is enlarged by a factor five. 2) As measured RIXS spectra 3) Calculated RIXS spectra

Table 5.4: The calculated energies and purities of La^{3+} $4d^{10}5p^54f^1$ RIXS final states.

State Symmetry	Purity in LS scheme	Energy (eV)
$^3D_1$	1.00	18.628
$^3D_2$	0.92	18.968
$^3F_2$	0.51	20.739
$^1D_2$	0.51	22.671

Table 5.5: The calculated intensities of La^{3+} $4d^94f^1 \rightarrow 4d^{10}5p^54f^1$ transitions.

Intermediate states	Final RIXS states			
	$^3D_1$	$^3D_2$	$^3F_2$	$^1D_2$
$^3P_1$	0.2382	0.3547	0.0002	0.0067
$^3D_1$	0.2115	0.0992	0.1545	0.1346
$^1P_1$	0.0002	0.0027	0.2648	0.3321

while the $^3F_2$ emission line have constructive interference. In panel 3 of Fig 5.4 the calculated RIXS spectra are shown beside the measured one. They resemble well the on resonance peak intensity behavior of the $^1D_2$ and $^3F_2$ emission lines. Note here that the calculated emission spectra are shifted with 0.48 eV to correspond with the measured one.

So far, we conclude that there are interfering scattering channels in the radiative decay of the $^3D_1$ resonance. But, we still do not know why the total fluorescence yield has a completely symmetric Lorenzian profile?

To answer this question we calculated the partial fluorescence yield of each radiative channel of the $^3D_1$ resonance, shown separately in Fig. 5.5. As can be seen from the figure, each $^1D_2$ and $^3F_2$ radiative channel show a very distorted line profile, but of positive and negative asymmetry parameter, respectively. Most notably, the sum of these two partial yields gives a very symmetric Lorentzian profile (displayed in panel 5 of Fig. 5.5). This sum rule is explained by the fact that these two final states are much less pure $^{2S+1}L_J$ states than the other $J = 2$ states. They are both only 51% pure and in addition, each $^1D_2$ and $^3F_2$ final state is given as a linear combination of the pure $^3F_2$ + $^1D_2$ symmetries.[2]

As a consequence, the radiative decay transition strength of the $^3D_1$ resonance it is shared equally to these two final states and because these two transitions have opposite symmetry parameters, the sum of their partial yields gives a fully symmetric Lorentzian.

The next radiative decay channels of the $^3D_1$ core excited resonance are the scattering to the $^3D_2$ and $^3D_1$ valence ionic final states. The same final states are reached also via resonant scattering from the low lying $^3P_1$ resonance. The RIXS calculations (please refer to Fig 5.5) showed that the coherent scattering to these two $^3D_2$ and $^3D_1$ final states does not show any interference effect. That is due to the fact that the energetic separation between these two final states (0.3 eV) it is smaller than their spectral lifetime broadening (FWHM of 0.4 eV), which follow that the interference effects can not be resolved.

[2]In the pure LS coupling scheme (disregarding the spin-orbit interaction) according to the dipole selection rules ($\Delta L = 1$), the $^3D_1$ core excited state will decay only to the $^3F_2$ state, while the $^1P_1$ state will decay only to the $^1D_2$ state. Due to the small spin-orbit interaction of the $5p$ hole these two states are completely mixed, thus that each state is given as a linear combination of the pure $^3F_2$ +^{1} D_2 symmetries.

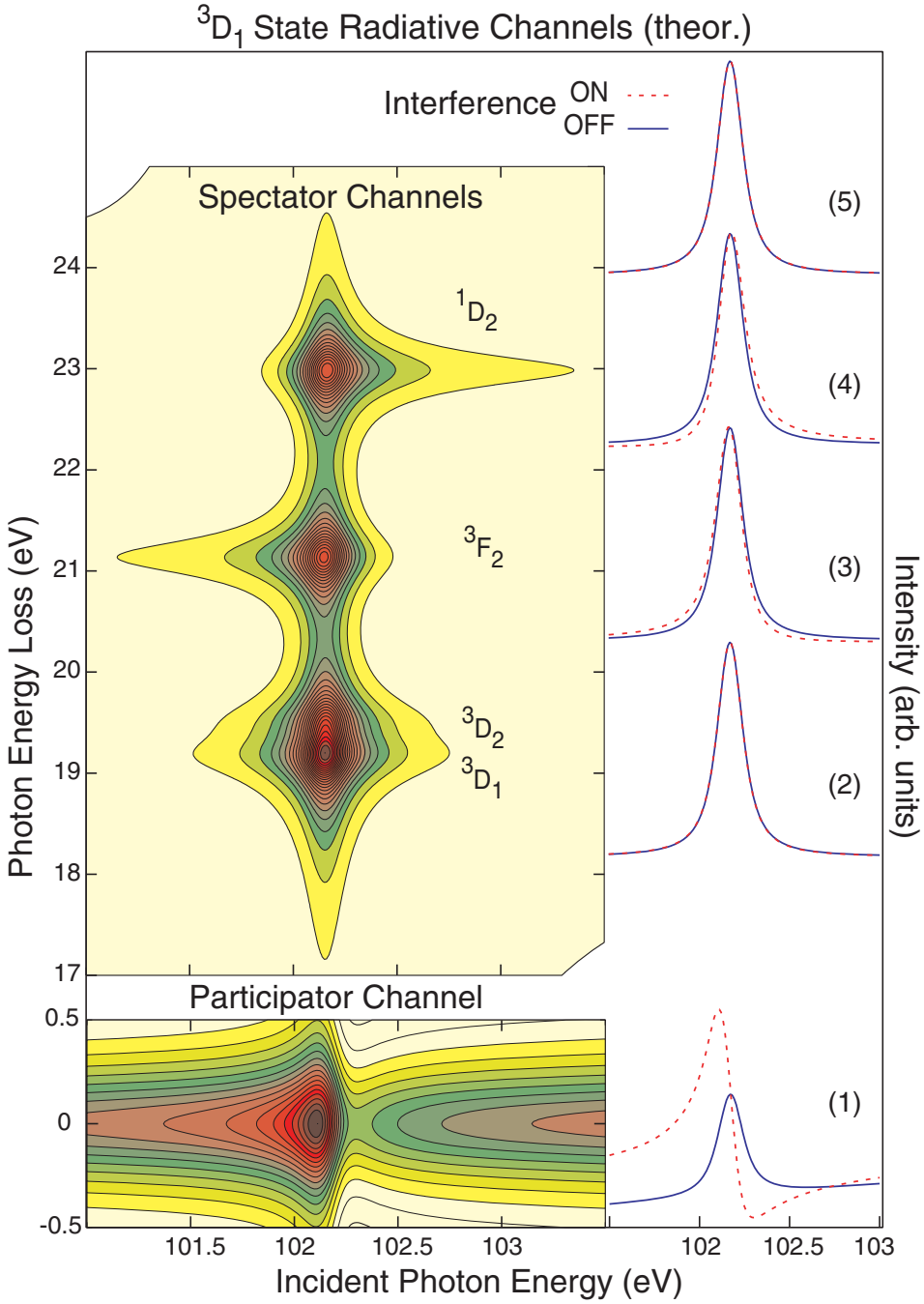

Figure 5.5: Partial fluorescence yield calculations of each decay channel of $^3D_1$ resonance. On the left side are shown the partial yield calculations where the resonant scattering processes are treated as coherent processes. On the right side, the solid curves are the integrated partial yields of each scattering channel. The dotted curves are the integrated partial yields where the resonant scattering processes are treated as independent processes (interference terms are excluded). Panel (5) shows the sum of $^1D_2$ and $^3F_2$ partial yields.

Participator decay channel

Another radiative decay channel of the $^3D_1$ resonance is the 4d4f participator channel, also referred as resonant elastic X-ray scattering (REXS) process:

$$4d^9 4f^1 \xrightarrow{V_r} 4d^{10} 4f_0$$

All the three intermediate core excited states will decay to this final state:

$$\mathbf{^3P_1, ^3D_1, ^1P_1} \xrightarrow{V_r} \mathbf{^1S_0}$$

As a consequence, the strongly correlated $^3D_1$ and $^1P_1$ intermediate states are coupled to the same scattering channel which leads to substantial interference. The dipole selection rule strengthen the contribution from the $^1P_1$ symmetry (please refer to the corresponding calculated intensities in Table 5.6) that leads to similar amplitudes of both interfering channels. In addition, the whole oscillator strength of the participator process goes to one single final state (similar to the electron yield). For all these reasons, the strength of the interference in the participator channel is quite profound, and leads to a very asymmetrical profile of the partial yield as it is evident from our calculations shown in panel (1) of Fig. 5.5.

Although the participator channel manifest a remarkable asymmetrical profile, its contribution to the total fluorescence yield is very small and almost undistinguishable. The sum of all the radiative decay contributions (spectator and participator channels) gives an almost symmetrical fluorescence yield profile and it is displayed in Fig. 5.9. This is due to the much stronger 4d5p (spectator) decay with respect to the 4d4f (participator) decay, prompted by the dipole selection rule. From our calculations results that the overall 4d5p spectator decay has a transition strength 100 times bigger than the participator decay.

Table 5.6: The calculated parameters of $4d^{10}4f^0$ ($\mathbf{^1S_0}$) final state and the radiation decay transition intensities ($4d^9 4f^1 \rightarrow 4d^{10}4f^0$) to this final state.

Final state			Transition Intensity		
Symmetry	Purity	Energy (eV)	$^3P_1$	$^3D_1$	$^1P_1$
$^1S_0$	1.0	0.0	0.00065	0.0057	1.9935

5.4.1 $^3P_1$ intermediate state

Similar results with that of $^3D_1$ resonance are found also for the $^3P_1$ intermediate state. The partial spectator yield and partial participator yield calculations of the $^3P_1$ resonance are shown in Fig. 5.6.

The radiative spectator decay of the $^3P_1$ intermediate state reaches mainly the $^3D_1$ and $^3D_2$ final states. The $^1D_2$ and $^3F_2$ final states have both less than 1% of the overall transition strength for the $^3P_1$ core excited state.

The same $^3D_1$ and $^3D_2$ final states are reached also from the $^3D_1$ resonance. Hence, the coherent scattering from both $^3P_1$ and $^3D_1$ symmetry contributions to these final states should lead to channel interference. (We recall here the results of the section 5.2, that the $^3P_1$ state is an entangled state consisting of 95% of $^3P_1$ symmetry contribution, 1.5% of $^1P_1$ symmetry contribution and 3.5% of $^3D_1$ symmetry contribution.) Our calculations do not resolve this interference. The integrated partial yields, calculated by considering the resonant scattering processes as coherent processes and as independent processes, displayed in panel (2) of Fig. 5.6, show both the same symmetrical spectral profile. As we specified for the $^3D_1$ resonance, this is due to the small energetic separation of these two $^3D_1$ and $^3D_2$ final states. Their energetic separation (0.3 eV) is smaller than their lifetime broadening (0.4 eV), and the two peaks are overlapped together giving a broad emission line, observed in the experimental RIXS data (panel (2)) and calculated spectra (panel (3)) of Fig. 5.4.

The 4d4f participator decay channel of the $^3P_1$ intermediate state exhibits a profound asymmetrical partial yield, similar to the $^3D_1$ resonance. Again, the asymmetry is due to the interference of coherent elastic scattering from both $^3P_1$, $^3D_1$ and $^1P_1$ symmetry contributions of the correlated $^3P_1$ intermediate state. Because the transition strength of the participator decay channel for the $^3P_1$ state is much smaller than the $^3D_1$ state[3], the intensity of this transition is much smaller than the 4d5p spectator one. Thus, the overall sum of both spectator and participator decay channels yield a symmetrical fluorescence profile, shown in panel (3) of Fig. 5.6, and is in accordance with the measured fluorescence yield profile. The measured and calculated total fluorescence yields are shown in Fig. 5.9.

[3]Due to the small $^1P_1$ symmetry contribution

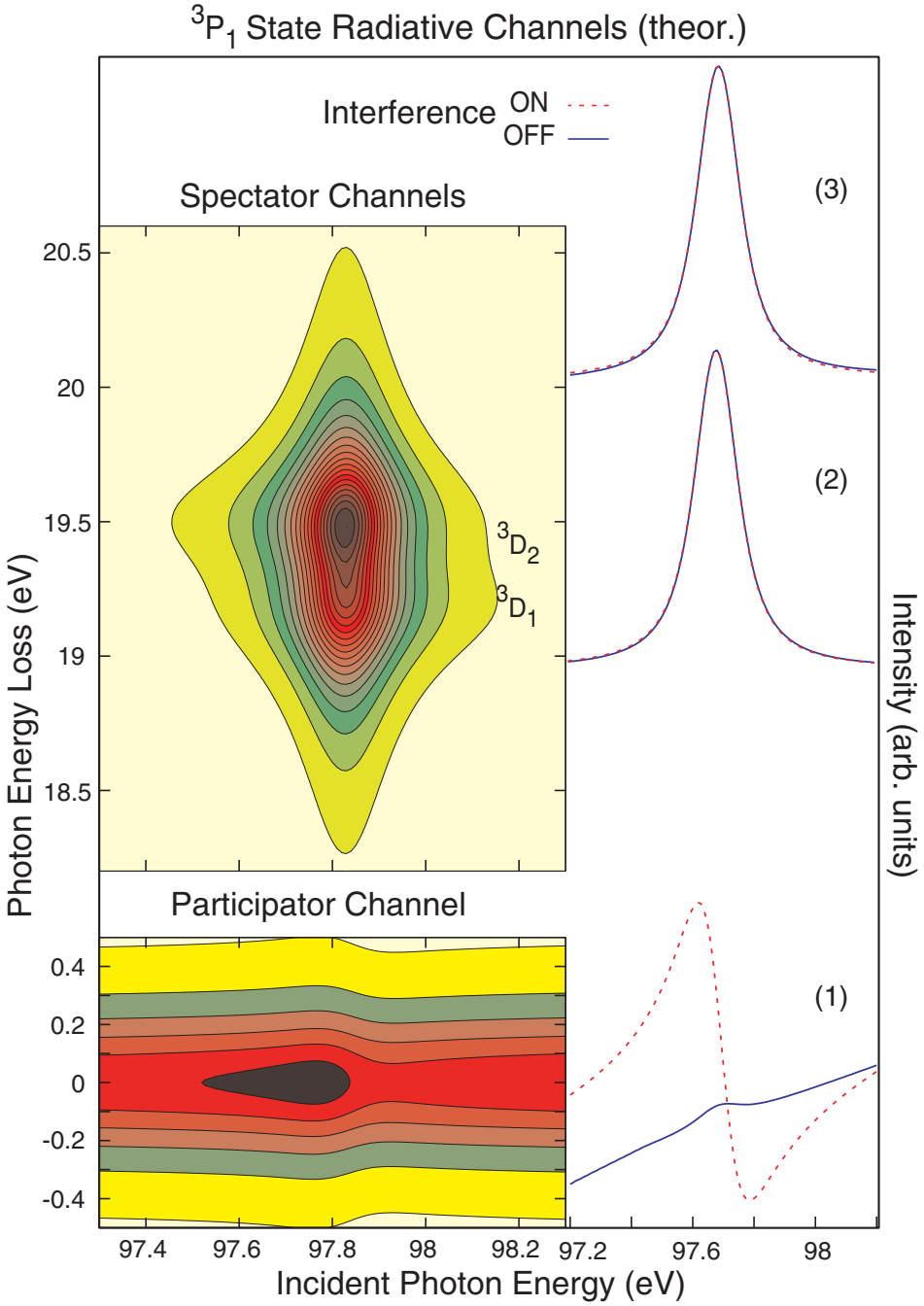

Figure 5.6: Partial fluorescence yield calculations of the participator and spectator decay channels of $^3P_1$ resonance. On the left side are shown the partial yield calculations where the resonant scattering processes are treated as coherent processes. On the right side, the solid curves are the integrated partial yields of each scattering channel. The dotted curves are the integrated partial yields where the resonant scattering processes are treated as independent processes (interference terms are excluded). Panel (3) shows the sum of both participator and spectator partial yields.

5.4.2 Intermediate state lifetime interference

Until here, we elaborated the correlation of physical states, and its influence in the spectral distribution of the oscillator strength. We determined that the weak spin-orbit interaction activates coherent scattering of different channels, that leads to channel interference, which is the critical argument behind the asymmetrical line profiles of the $4d$ XAS spectra.

In this section, we would like to investigate the influence of the large lifetime broadening of the giant $^1P_1$ resonance in the interfering channels and consequently in the spectral profiles. The broad and strong $^1P_1$ giant resonance, as discussed in section 5.2, is of atomic origin[4] [79, 80]. Due to the strong direct and exchange Coulomb interaction of the $4d$ core hole with the $4f$ excited electron, the $^1P_1$ state is pushed above the $4d$ ionization threshold. Thus, the coupling of $^1P_1$ discrete state to the continuum states contributes a broadening to the XAS line width beyond the core hole lifetime broadening.

The XAS line width of $^1P_1$ state in the free La^{3+} ions, which in their ground state are essentially unperturbed by their metallic environment, is reported [81] to be only 2.3 eV. Whereas, the line width of $^1P_1$ state in LaF_3 is much broader [82, 83], and in free La atoms is $\sim$ 10eV [84]. It was shown by Köble *et al.* [81] that the energetic position and the width of $^1P_1$ giant resonance in its solid state is influenced albeit moderately by the environment, which causes the resonance to be broadened and shifted by 1.3eV toward lower energies. It is mainly the autoionization of the $4d^9 4f^1\ {}^1P_1$ state to the $4d^9 4f^0 \varepsilon_f$ continuum states that causes the additional broadening. In our XAS experimental spectra, the width of the $^1P_1$ resonance in $LaPO_4$ nanoparticles exhibited a large lifetime broadening of $\sim$ 9eV.

Because the energetic spacing between the $^1P_1$ and $^3D_1$ resonances is of the same scale as the $^1P_1$ lifetime width, the mixing of the $^1P_1$ resonance's spectral tail with the $^3D_1$ resonance could lead to a change in spectral distribution of the oscillator strength, accompanied with a change of scattering amplitudes. The later one is exhibited in a less or stronger interference effects (in a less or stronger asymmetric profiles).

In order to investigate the leverage of broad $^1P_1$ lifetime width in the spectral profiles, we performed two types of radiative scattering calculations.

[4]The precise interpretation of giant resonances is done in terms of strongly damped collective resonances involving coherent motion of all electrons in the $4d^{10}$ shell [76, 77], but it is qualitatively understood in terms of independent electron approximation [78].

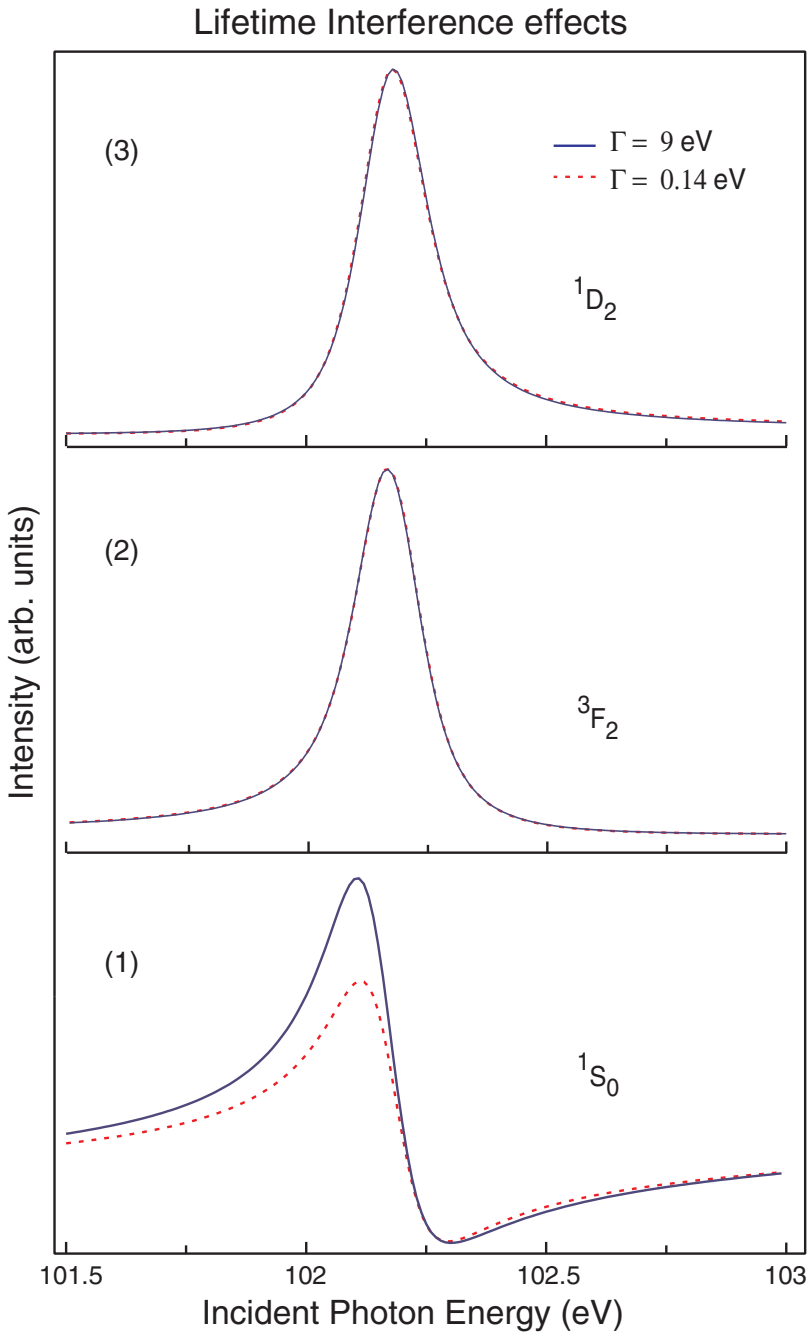

Figure 5.7: The calculated partial fluorescence yields for different decay channels of $^3D_1$ resonance. The blue solid curves are the calculated spectra where the interference due to the intermediate states lifetime broadening is considered. The red dotted curves comprises only the interference effects due to the correlated intermediate states and excludes the lifetime interference.

In the first calculation, we excluded the possibility for lifetime interference by assuming the three $^3P_1$, $^3D_1$, and $^1P_1$ resonances of the $4d \rightarrow 4f$ transitions to have the same lifetime width of 0.14eV. Indeed, the experimental spectra showed for both $^3P_1$ and $^3D_1$ resonances to have a width of $\Gamma = 0.14$eV. In addition, we assumed a "virtual" lifetime width of $\Gamma = 0.14$eV also for the $^1P_1$ resonance (to partly counteract the broadening of the resonance due to the 4d continuum states). This is not very close to the real lifetime width ($\sim 2.3eV$) of the $^1P_1$ giant resonance measured at free La^{3+} ions [81], but it is good in the framework of a model to exclude the possibility for intermediate state interference.

In the second calculations we accounted for the lifetime broadening due to the solid state effects and used for the $^1P_1$ state the experimental lifetime width $\Gamma = 9$eV. Note that in all the calculations presented in section 5.4, we have used as lifetime width the values revealed from the experimental XAS spectra.

The results of both calculations for the $^3D_1$ resonance are presented in Fig. 5.7. As it can be seen from the spectra, the broad lifetime width of the $^1P_1$ state increases the asymmetry of the participator radiative channel, but it does not alter at all the asymmetry parameter for the two spectator decay channels. This is explained by the fact that the two final states ($^1D_2$ and $^3F_2$) reached by the spectator decay are completely mixed states. Thus any additional oscillator strength pumped from the intermediate resonance will be equally shared to both final states. As a result no additional asymmetry is induced to the fluorescence partial yield of these decay channels.

In contrast to these results, the participator channel does show an increased asymmetrical profile. We recall here that the $^1S_0$ final state is a 100% pure state. Thus, the additional oscillator strength coming from the higher percentage of $^1P_1$ symmetry at the $^3D_1$ threshold, due to mixing of $^3D_1$ core excited state with the spectral tail of the $^1P_1$ intermediate state, will increase the radiative decay of the $^1P_1$ symmetry at the $^3D_1$ resonance. This will cause an increase of the scattering amplitude of this channel compared to the scattering from the $^3D_1$ symmetry. As a consequence, the interference of these two coherent scattering channels will change the asymmetry of the spectral profile.

Because the contribution of the participator channel to the fluorescence yield is very small than the spectator channel, we conclude that the asymmetry in the spectral shape of the 4d XAS spectrum is mainly due to correlation effects.

5.5 Conclusion

In this work we have conducted highly resolved X-ray absorption and resonant inelastic X-ray scattering experiments and theoretical calculations to unravel many body aspects of the strong Coulomb electron-electron interaction in lanthanum ions. The strong overlap of the localized $4d$ and $4f$ wavefunctions gives rise to strong direct and exchange Coulomb interaction of the $4d$ hole and excited $4f$ electron. The coupling of the excited electron with the remaining core hole creates new final states which do not exist within the single electron approximation. These states are highly correlated discrete states entangled by different symmetry contributions. Thus, resonant excitation of these states leads to coherent scattering from all symmetry contributions and concomitantly to interference of different scattering channels. This explains the highly asymmetrical profile of the total electron yield spectrum, which is, in fact, the X-ray absorption spectral shape. The fluorescence yield detected spectrum becomes symmetric due to the breaking of coherence in some of the decay channels. The symmetry aspect of the dipole transition in the radiative decay together with the highly correlated final ionic states are the reason for breaking the coherence in some of the scattering channels. In Fig. 5.8 the different scattering channels of the nonradiative and radiative decay that have a $5p$ hole in the final states are depicted.

In addition, the influence of lifetime interference in the scattering channels due to the very broad giant resonance was thoroughly investigated. The calculations showed that the asymmetry induced from lifetime interference in the spectral profile is very small compared to the one induced from symmetry entangled intermediate states. The calculated electron and fluorescence yield spectra considering the interference from both constituents revealed the same spectral profile as the experiment. In Fig. 5.9 are displayed both, the measured and calculated spectra.

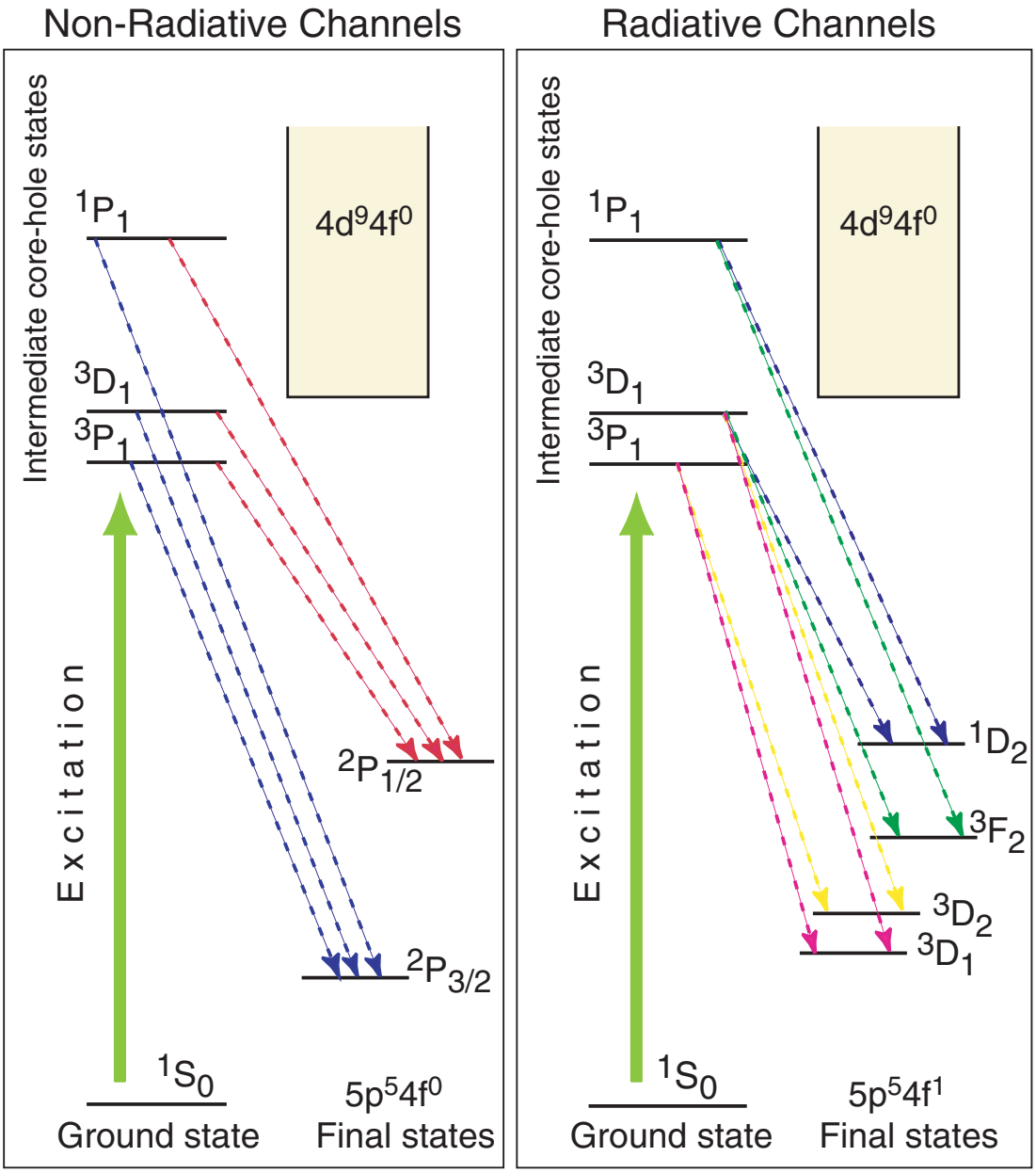

Figure 5.8: Schematic of radiative and nonradiative decay channels of each resonance that have a $5p$ hole in the final state. The scattering channels shown with the same color interfere due to the correlated intermediate state. The breaking of energy coherence in the final states of radiative decays due to the symmetry selection rule decreases the number of interfering channels.

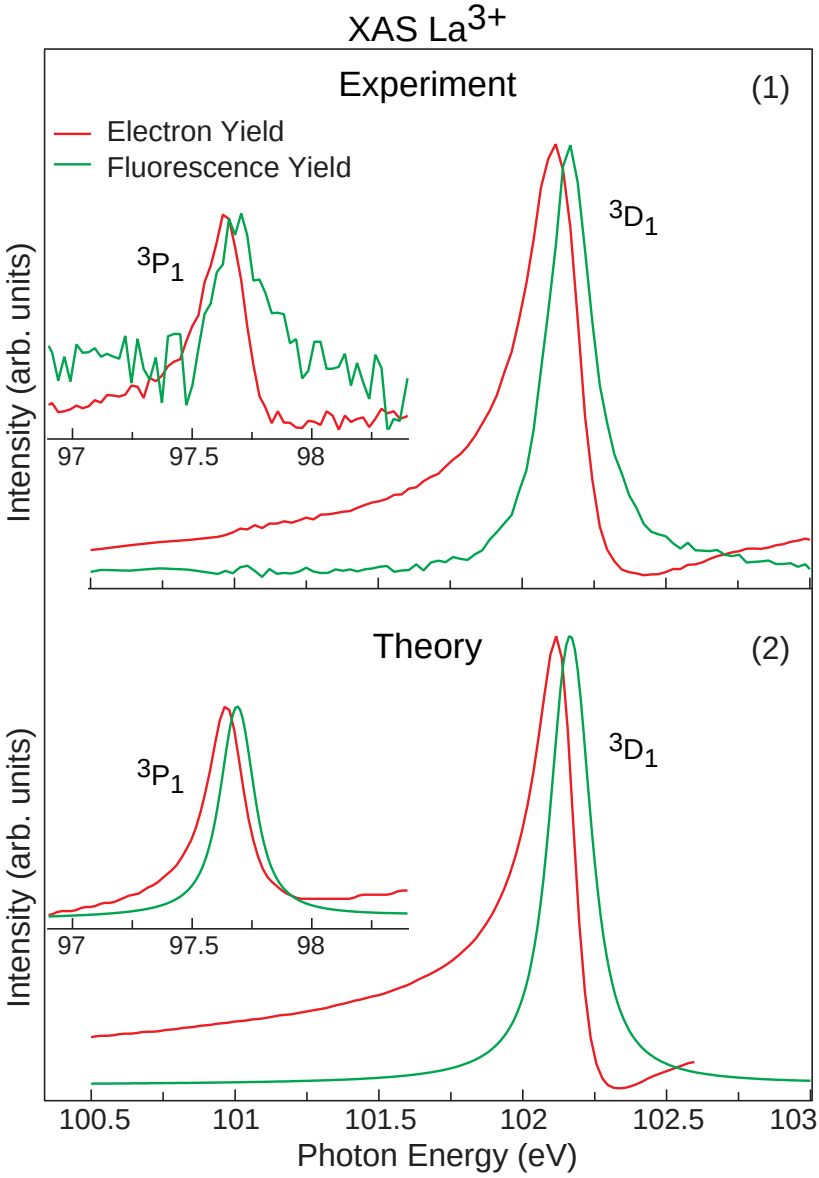

Figure 5.9: Measured and calculated La $N_{IV,V}$ XAS spectra. 1) $^3P_1$ and $^3D_1$ resonances of La $N_{IV,V}$ XAS spectrum measured in $LaPO_4$ nanoparticles. 2) Calculated partial electron yield and TFY spectra at the $^3P_1$ and $^3D_1$ resonances. They reveal the same spectral profiles as the experiment. The measured spectra are normalized to the photon flux and subsequently to the peak maximum. The intensities of the $^3P_1$ resonance in both measured and calculated spectra are enlarged by a factor three.

Chapter 6

Trends in lanthanide systems: from simple to complex

Starting from Lanthanum (atomic configuration $4f^0$) and going through the lanthanide series, an electron is added successively in the $4f$ shell. In the $N_{4,5}$-edge X-ray absorption process, the increased number of electrons in the $4f$ shell results in a much stronger direct and exchange Coulomb interaction between the core hole and the 4f electrons. Thus, the total multiplet structure becomes very complex, and the X-ray absorption spectra consist of several sharp peaks (pre-resonances) followed by dipole allowed giant resonances. Again here, the small core hole spin-orbit interaction mixes pure LS states, and cause the pre-resonances to be symmetry entangled states.

The calculated total number of energetic levels in the intermediate coupling scheme ($\Delta J = 0, \pm 1$) reached in the $N_{4,5}$ absorption process, increases from 3 in Lanthanum to 53 in Cerium, to 200 in Praseodymium and to 1077 in Gadolinium. In the late lanthanides, where the number of holes in the $4f$ shell start reducing, the number of energetic levels falls again to 4 in Thulium and 1 in Ytterbium. In addition, the screening of the core hole potential from the $4f$ electrons give rise to a smaller direct Coulomb interaction in the heavier lanthanides. Nevertheless, it is not possible to resolve all the multiplet lines in the $N_{4,5}$ XAS spectra except for Lanthanum, Thulium and Ytterbium.

6.1 Light Lanthanides

X-ray absorption spectra of Cerium and Praseodymium

In the previous chapter the thorough investigation of different scattering channels and interference effects that led to different line profiles of La^{3+} $N_{4,5}$-edge electron and fluorescence yields was elaborated. $N_{4,5}$ X-ray absorption spectra of Ce^{3+} and Pr^{3+} measured in lanthanide phosphate nanoparticles reveal the same line profile behavior: Electron yield pre-edges show asymmetrical line profiles with a spectral tail in the low energy ranges of the peaks, while the fluorescence yield pre-edges show more symmetrical lineshapes. The measured absorption spectra for cerium and praseodymium triply ionized ions hosted in phosphate nanoparticles are shown in Fig. 6.1, and Fig. 6.2, respectively. Some of the pre-resonances are shown in an enlarged scale in order to highlight their spectral shapes.

Cerium and praseodymium triply ionized ions have one and two electrons in their $4f$ shell, respectively. Because the electrons in the $4f$ shell are quite localized, the promotion of the $4d$ electron in the $4f$ shell (during the XAS process) give rise to a stronger core hole - $4f$ electrons Coulomb interaction and to a stronger wavefunction overlap (exchange interaction). Thus, due to this strong multiplet splitting, the oscillator strength of the $4d \rightarrow 4f$ transition is distributed over many resonances, and hence, the absorption spectrum contain many sharp pre-resonances followed by the dipole allowed giant resonances. In the framework of La model, we would expect the localized core excited states in cerium and praseodymium to be highly correlated states consisting of different symmetry contributions. This again would lead to coherent scattering from these different symmetry contributions and would result to channel interference and concomitant asymmetrical profiles of electron yield spectra. In the radiative decay, symmetry selection rule could cause breaking of coherence in some of the scattering channels, that could result in less interfering channels and hence in more symmetrical profiles. In addition, correlation of the final states of RIXS process ($5p$ hole final states) is expected to play an important role, as in the case of lanthanum.

Detailed calculation of X-ray absorption spectra and analysis of their spectral profiles is an ongoing project beyond this thesis.

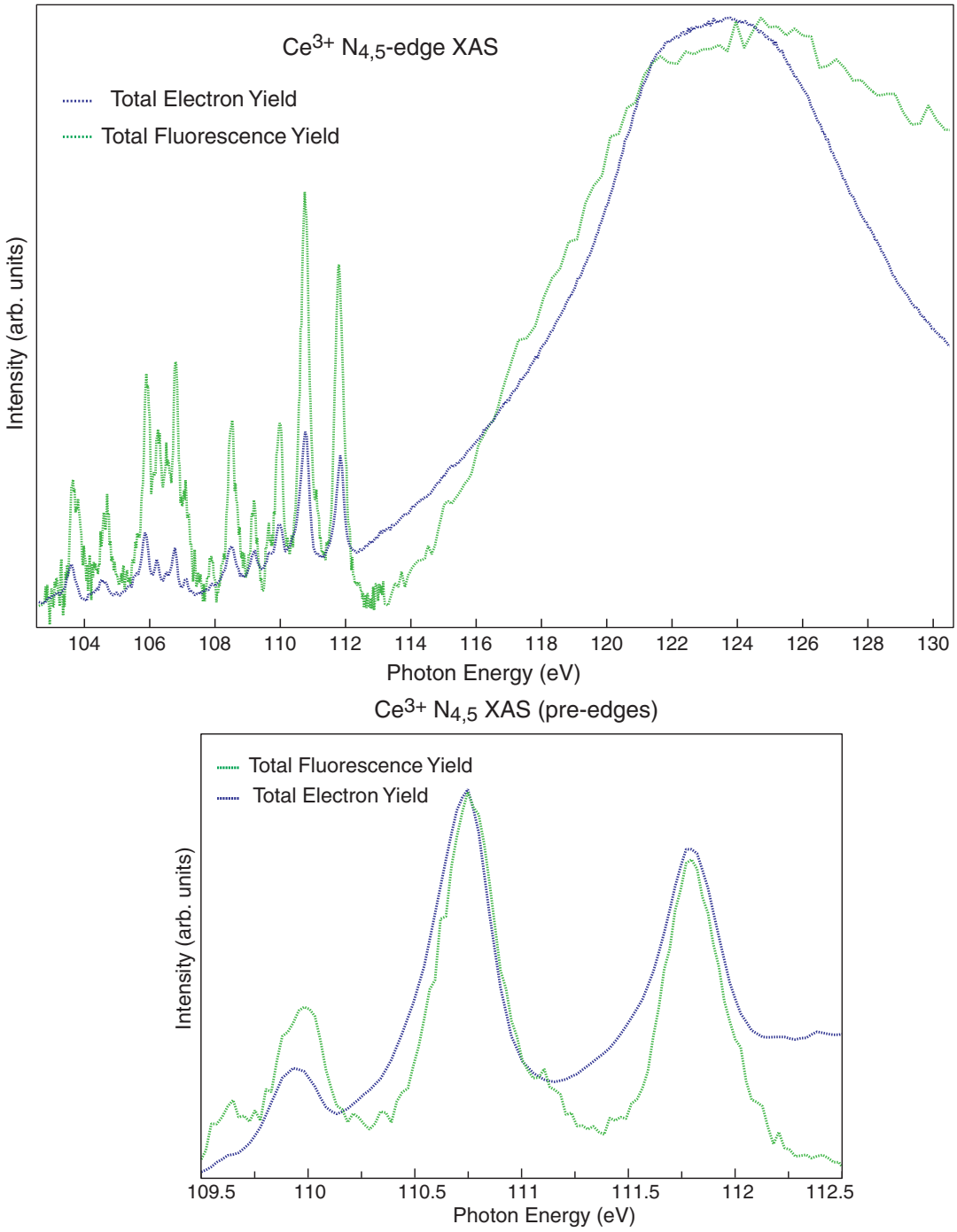

Figure 6.1: Experimental $N_{4,5}$-edge XAS of Ce^{3+} ions in $CePO_4$ nanoparticles measured in electron and fluorescence yield. Bottom: Pre-edge area is enlarged to highlight peak asymmetrical profile of electron yield towards symmetrical fluorescence yield profiles.

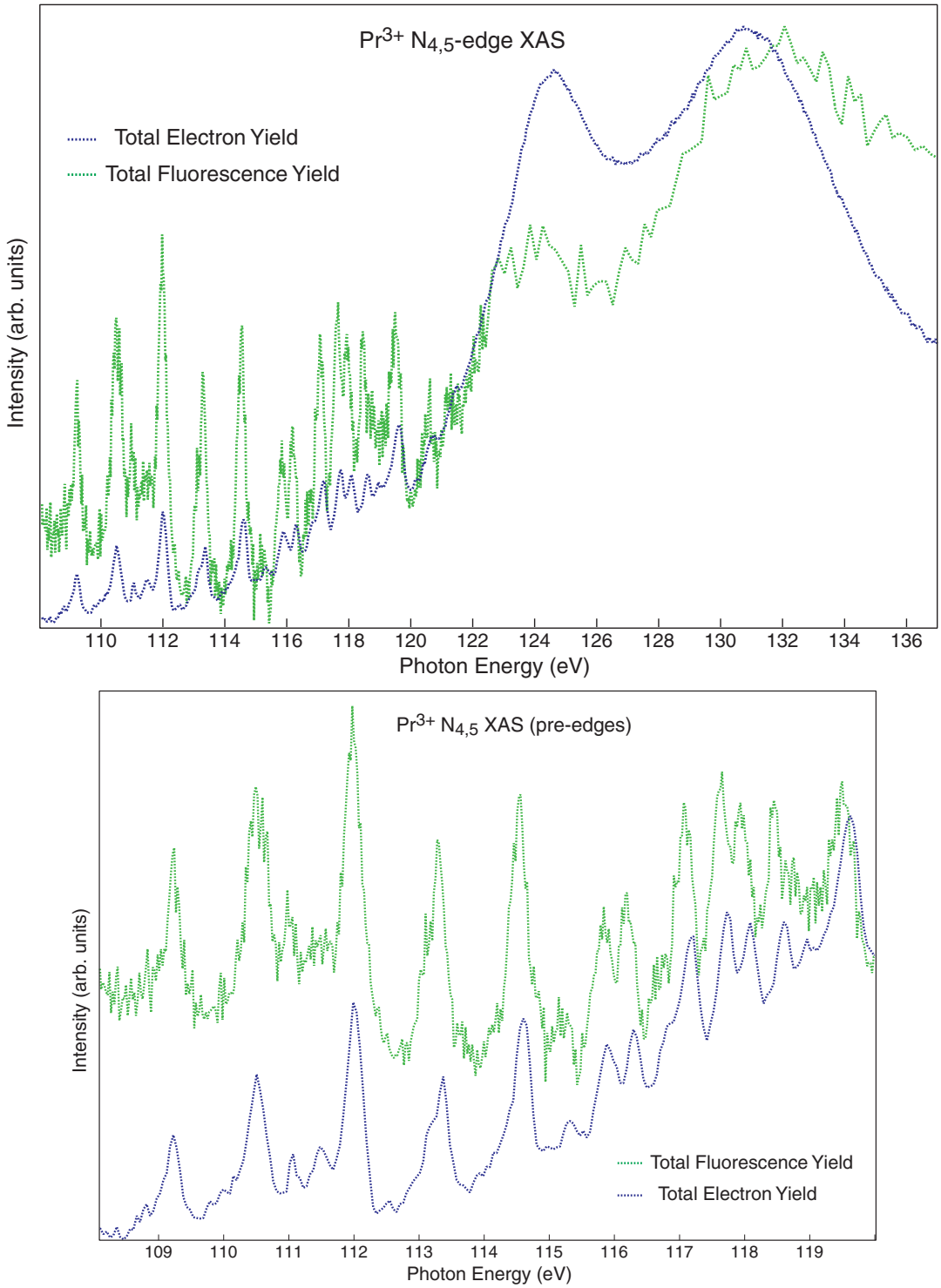

Figure 6.2: Experimental $N_{4,5}$-edge XAS of Pr^{3+} ions in $PrPO_4$ nanoparticles measured in electron and fluorescence yield. Bottom: Pre-edge area is enlarged to highlight peak asymmetrical profile of electron yield towards symmetrical fluorescence yield profiles.

Radiative decay at the $^1P_1$ giant resonance of La

The resonant inelastic X-ray scattering (RIXS) spectra measured at the $^3D_1$ and $^3P_1$ localized pre-resonances of the $N_{4,5}$ absorption edge, and presented in section 5.4, showed a linear dispersion behavior with incoming photon energy manifesting coherence of excitation-deexcitation processes. Differently, at the $^1P_1$ giant resonance, the measured RIXS spectra, shown in Fig. 6.3, manifest both linear dispersed lines as well as constant photon energy features. The situation is far more complicated here, because the $^1P_1$ discrete state lays above the $4d$ ionization threshold and is directly coupled to the $4d$ continuum states. Hence, the dipole allowed $^1P_1$ discrete state is not only coupled to the lower laying $^3D_1$ and $^3P_1$ discrete states via core hole spin orbit interaction and its broad lifetime width, but in addition is also coupled to the $4d^9\varepsilon f$ continuum states via configuration interaction mixing [30]. As a consequence, radiative scattering experiments across the $^1P_1$ resonance reflect the strength of the different couplings across the resonance.

From the experimental data of La^{3+} giant resonance, presented in Fig. 6.3, one can observe that the coupling of $^1P_1$ state to the entangled $^3D_1$ and $^3P_1$ states dominates the scattering channels. The broad emission features at constant photon energies $75 - 83$ eV are due to

$$4d^9 5p^6 4f^1(\mathbf{^1P_1}) \Rightarrow 4d^9 5p^6 4f^1(\mathbf{^3D_1},\mathbf{^3P_1}) \Rightarrow 4d^{10} 5p^5 4f^1(\mathbf{^1D_2},\mathbf{^3F_2},\mathbf{^3D_2},\mathbf{^3D_1})$$

transitions. These scattering channels demonstrate that the core excited electron at the $^1P_1$ state decays within the $4d$ core hole lifetime to the localized $^3D_1$ and $^3P_1$ states and then the core hole decays through $4d5p$ channel.

The $^3D_1$ and $^3P_1$ states decay also, through a very small channel indicated with the dotted lines in Fig. 6.3, directly to the ground initial state:

$$4d^9 5p^6 4f^1(\mathbf{^1P_1}) \Rightarrow 4d^9 5p^6 4f^1(\mathbf{^3D_1},\mathbf{^3P_1}) \Rightarrow 4d^{10} 5p^6 4f^0(\mathbf{^1S_0})$$

resulting in constant energy emission lines at 97.5 eV and 101.9 eV. As discussed in the previous chapter, the small intensity of these two emission lines is due to the small crossection of these two partly allowed transitions.

Coupling of the $^1P_1$ giant resonance state to the continuum $4d\varepsilon f$ states manifests itself in the relatively strong constant energy emission line centered at 85 eV. The radiative decay is due to the two step processes:

$$4d^9 5p^6 4f^1(\mathbf{^1P_1}) \Rightarrow 4d^9 5p^6 4f^0 \varepsilon f \Rightarrow 4d^{10} 5p^5 4f^0$$

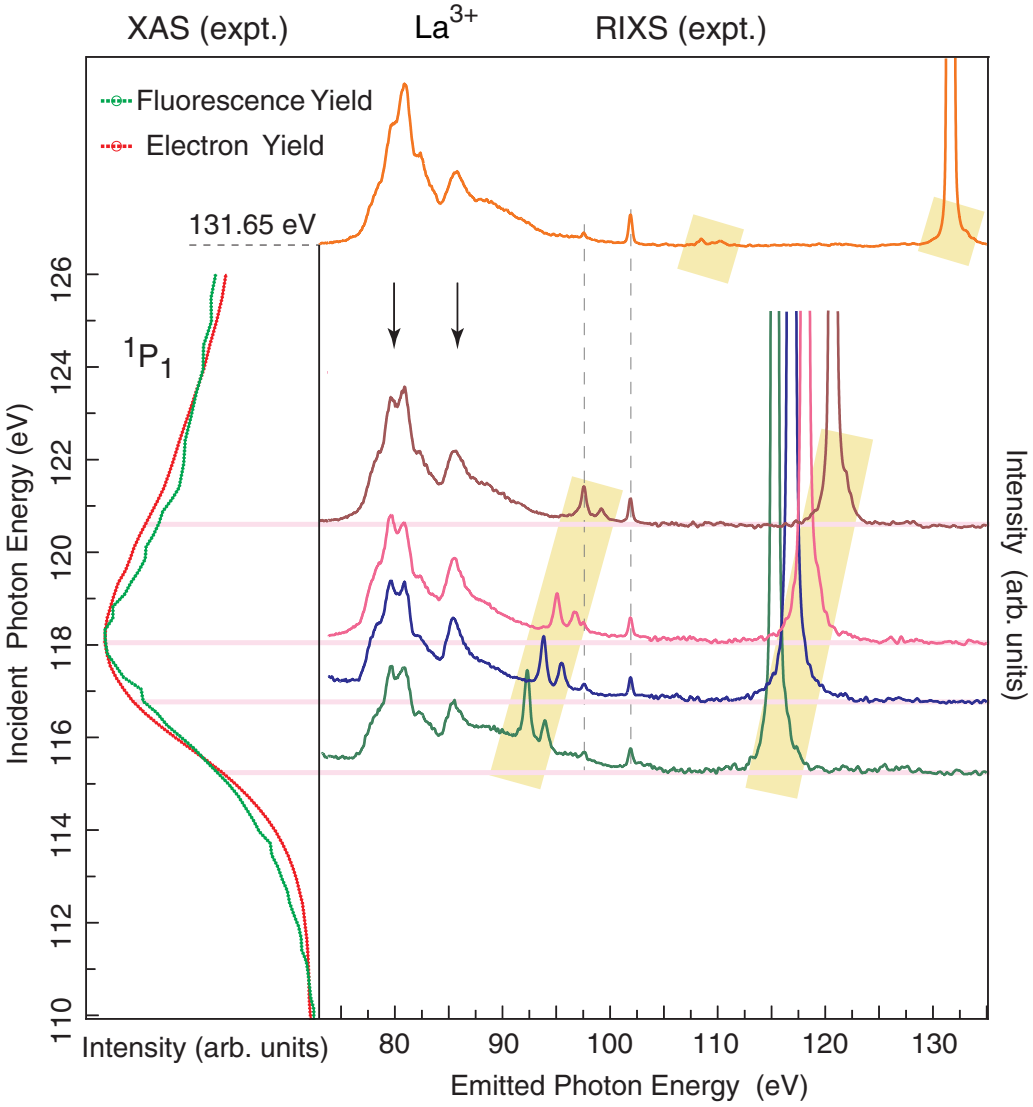

Figure 6.3: A series of experimental RIXS spectra measured across $^1P_1$ giant resonance of La^{3+} in $LaPO_4$ nanoparticles. Emission lines at constant photon energies $75-83$ eV, 97.5 eV and 101.9 eV are due to the decay of $^1P_1$ state to the more localized $^3D_1$ and $^3P_1$ states that further decay to $4d^95p^64f^1(^3D_1,^3P_1) \rightarrow 4d^{10}5p^54f^1$; $4d^95p^64f^1(^3P_1) \rightarrow 4d^{10}5p^64f^0$; and $4d^95p^64f^1(^3D_1) \rightarrow 4d^{10}5p^64f^0$, respectively. Emission line centered at 85.5 eV is due to $4d^95p^64f^0 \rightarrow 4d^{10}5p^54f^0$ transition from the quadruply ionized La^{4+} ion. Here radiative decay occurs as a two step process; first the excited electron ionizes into continuum then the core hole decays. Linearly dispersed lines started at $\sim$ 95 eV (yellow highlighted) are due to coherent excitation-deexcitation process: $4d^95p^64f^1(^1P_1) \rightarrow 4d^{10}5p^54f^1(^1D_2,^3F_2)$. Linearly dispersed line started at $\sim$ 115 eV (yellow highlighted) is due to elastic scattering.

where the excited $4f$ electron delocalizes in continuum prior to the decay of the $4d$ core hole.

Nevertheless, the coherent excitation-deexcitation channel of the $^1P_1$ giant resonance to the final $^1D_2$ and $^3F_2$ states via the decay process:

$$4d^9 5p^6 4f^1(\mathbf{^1P_1}) \Rightarrow 4d^{10} 5p^5 4f^1(\mathbf{^1D_2}, \mathbf{^3F_2})$$

it is observed in the experimental measurements, the yellow highlighted linearly dispersed lines started at 95 eV, although at a smaller cross section.

All the different radiative decay processes of the $^1P_1$ giant resonance mentioned above emphasize for a strong mixing of discrete and continuum states. The detailed analysis of intensity variation of different scattering channels across the $^1P_1$ giant resonance can give information on relaxation dynamics within the core hole life time, known as core hole clock method [85, 86]. Moreover, the comparison of time scale relaxation dynamics within lanthanides can give comprehensive information on localization/delocalization character of giant resonance's wave functions. The analysis of the experimental RIXS data (measured at $N_{4,5}$ absorption edge of La^{3+}, Ce^{3+}, and Pr^{3+}) are subject of ongoing investigations beyond this thesis.

6.2 Heavy Lanthanides

With increasing Z among the lanthanides, the $4f$ wavefunction becomes more localized and the dipole allowed giant resonances are located closer the $4d$ ionization threshold [87]. Due to this wavefunction localization, the competition between continuum transitions $4d^{10} \rightarrow 4d^9 \epsilon f$ and discrete transitions $4d^{10}4f^n \rightarrow 4d^9 4f^{n+1}$ at the giant resonances takes place [87–89].

For heavier elements of the lanthanide series, the $4f$ wavefunction collapses inside the centrifugal barrier and transitions to the discrete states $4d^{10}4f^n \rightarrow 4d^9 4f^{n+1}$ dominate [88, 89] the $N_{4,5}$ absorption process. Because the number of holes in the ground state configuration of the $4f$ shell is only one for Yb^{3+}, two for Tm^{3+} and three for Er^{3+}, the number of reached final states in the X-ray absorption process is small. This facilitates the detailed analysis of multiplet structures in the XAS spectra.

In our research we have performed XAS and RIXS experiments in Yb^{3+}, Tm^{3+} and Er^{3+} ions hosted in $LaPO_4$ nanoparticles. The experimental data are shown in Fig. 6.4, 6.5, and 6.6. From the spectra one can observe that the

radiative decay of the core excited states is dominated by the coherent excitation-deexcitation process: The emission lines linearly disperse with excitation photon energy. A very small radiative decay channel is observed at constant emitted photon energies, which is due to the delocalization of the excited electron in the final state of the XAS process, i.e., the charge transfer channel. This channel is yellow highlighted in the figures and its intensity becomes smaller going from Yb^{3+} to Er^{3+} (please refer to figures 6.4, 6.5, and 6.6).

The loss features in the RIXS spectra at the energy interval $0 - 10$ eV, are shown in Fig. 6.7 for Yb^{3+}, in Fig. 6.8 for Tm^{3+} and in Fig. 6.9 for Er^{3+}. They are due to reconfigurations within the $4f$ shell (f-f transitions):

$$4d^{10}4f^n \Rightarrow 4d^9 4f^{n+1} \Rightarrow 4d^{10}4f^n$$

Thus, the core excited $4d^9 4f^{n+1}$ states do not decay only to the ground $4d^{10}4f^n$ state but also to the higher lying $4f^n$ states. Yb^{3+} is a very simple case, because it has only one single hole in the ground state $^2F_{7/2}$, and its absorption spectrum consist of only one single peak due to the transition $4d^{10}4f^{13}(\mathbf{^2F_{7/2}}) \Rightarrow 4d^9 4f^{14}(\mathbf{^2D_{5/2}})$. The $^2D_{5/2}$ core excited state can decay either to the ground state $4f^{13}(\mathbf{^2F_{7/2}})$ that corresponds to the energy loss feature located at 0eV, or to the $4f^{13}(\mathbf{^2F_{5/2}})$- the loss feature at $\sim$ 1eV (please refer to Fig. 6.7).

In case of Tm^{3+} (Fig.6.8) and Er^{3+} (Fig. 6.9) there are observed more loss features due to the more available free f states (two- and three- holes, respectively, in the ground configurations). The different loss features are assigned to different f-f excitation states, based on the $4f$ energy level schemes taken from references [90] and [91].

In addition to the low energy loss features, also emission lines at rather higher energy losses ($\sim$ 15–35eV) are observed. The experimental data are shown for Yb^{3+} in Fig. 6.7, for Tm^{3+} in Fig. 6.10, and for Er^{3+} in Fig. 6.11. These loss features are due to the $4d5p$ transitions:

$$4d^{10}5p^6 4f^n \Rightarrow 4d^9 5p^6 4f^{n+1} \Rightarrow 4d^{10}5p^5 4f^{n+1}$$

with a $5p$ hole in the final state.

Detailed analysis and theoretical calculations of RIXS spectra are an ongoing project beyond this thesis.

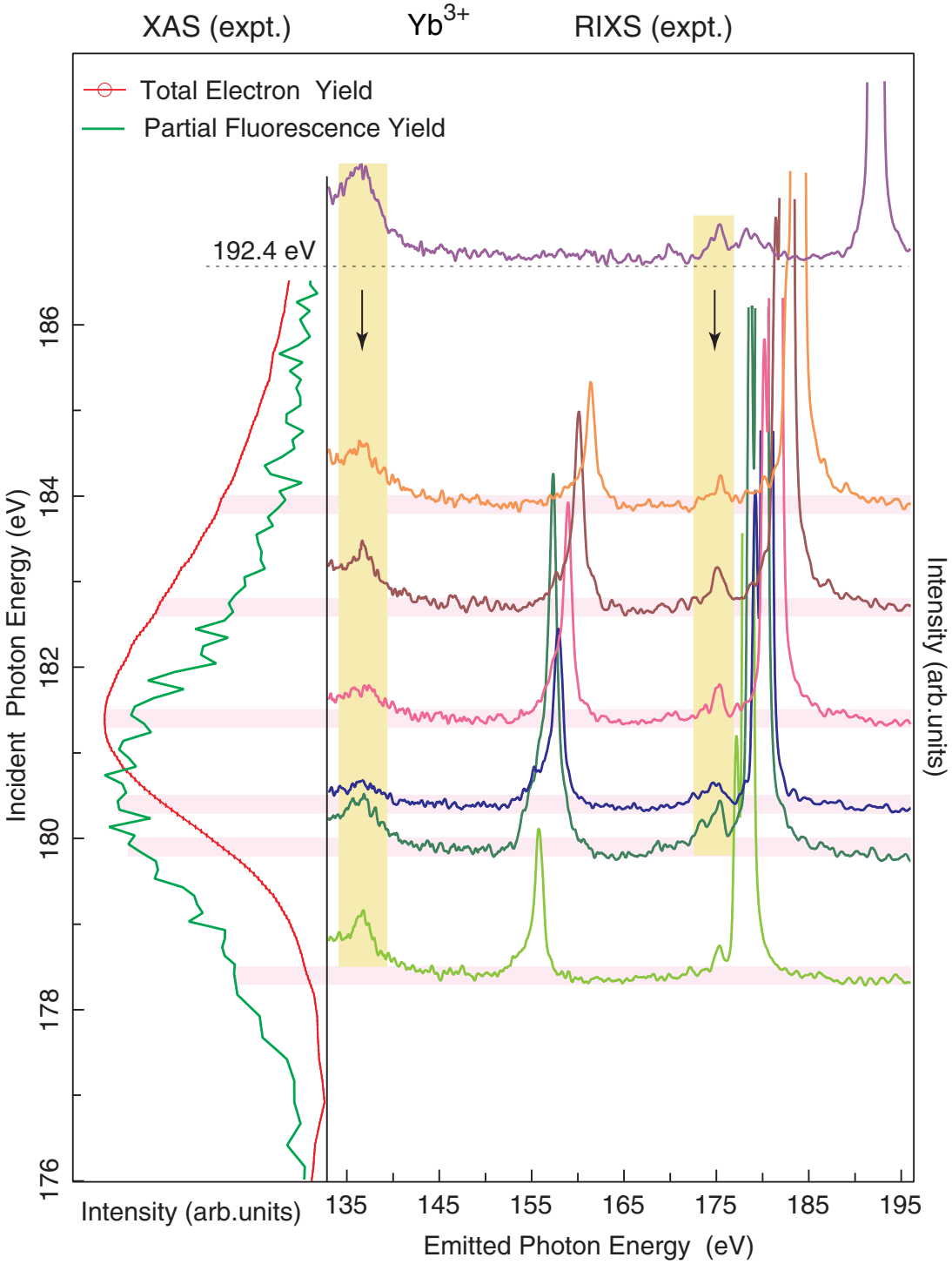

Figure 6.4: A series of experimental RIXS spectra measured at $N_{4,5}$ edge of Yb^{3+} in $YbPO_4$ nanoparticles. Yellow highlighted are the charge transfer transitions due to $4d^95p^64f^{14} \rightarrow 4d^95p^64f^{13}\varepsilon f \rightarrow 4d^{10}5p^54f^{13}$ and $4d^95p^64f^{14} \rightarrow 4d^95p^64f^{13}\varepsilon f \rightarrow 4d^{10}5p^64f^{12}$

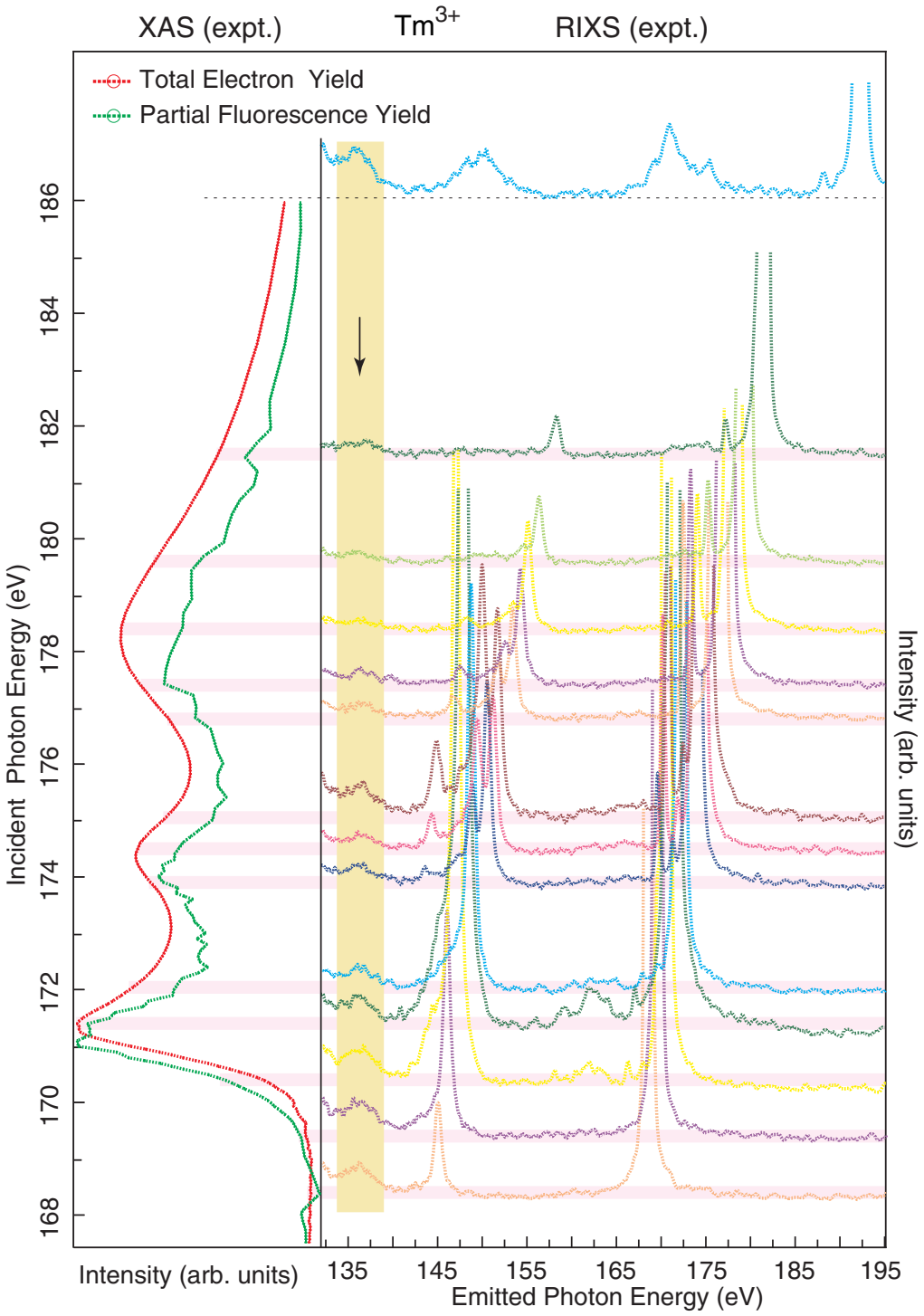

Figure 6.5: A series of experimental RIXS spectra measured at $N_{4,5}$ edge of Tm^{3+} in $TmPO_4$ nanoparticles. Yellow highlighted is the charge transfer transition due to $4d^9 5p^6 4f^{13} \rightarrow 4d^9 5p^6 4f^{12} \varepsilon f \rightarrow 4d^{10} 5p^5 4f^{12}$. Intensity of this channel is smaller than in Yb^{3+}.

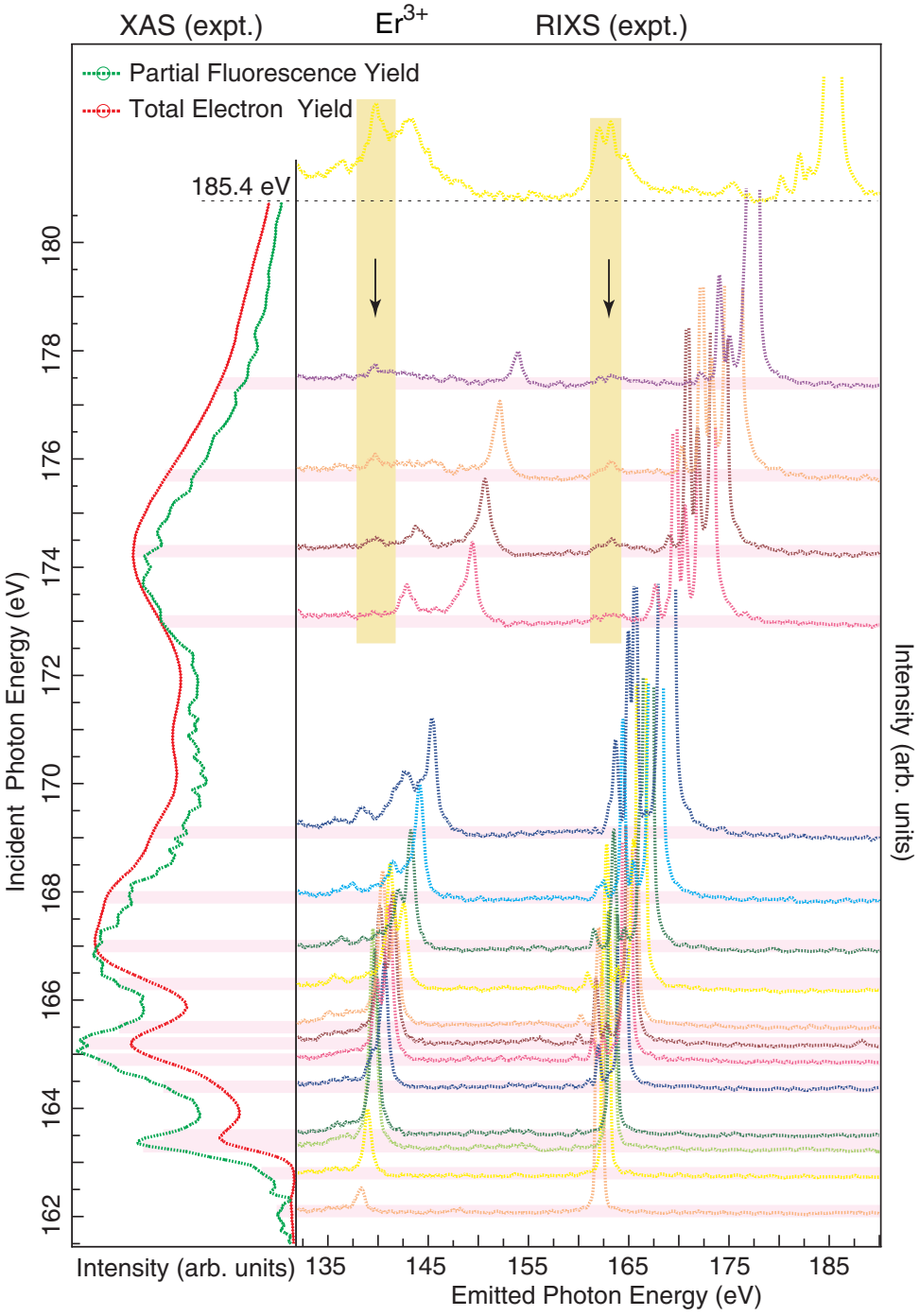

Figure 6.6: A series of experimental RIXS spectra measured at $N_{4,5}$ edge of Er^{3+} in $ErPO_4$ nanoparticles. Yellow highlighted are the charge transfer transitions due to $4d^95p^64f^{12} \rightarrow 4d^95p^64f^{11}\varepsilon f \rightarrow 4d^{10}5p^54f^{11}$ and $4d^95p^64f^{12} \rightarrow 4d^95p^64f^{11}\varepsilon f \rightarrow 4d^{10}5p^64f^{10}$. Intensities of these channels are very small, addressing for a localized character of the $4f$ wavefunction.

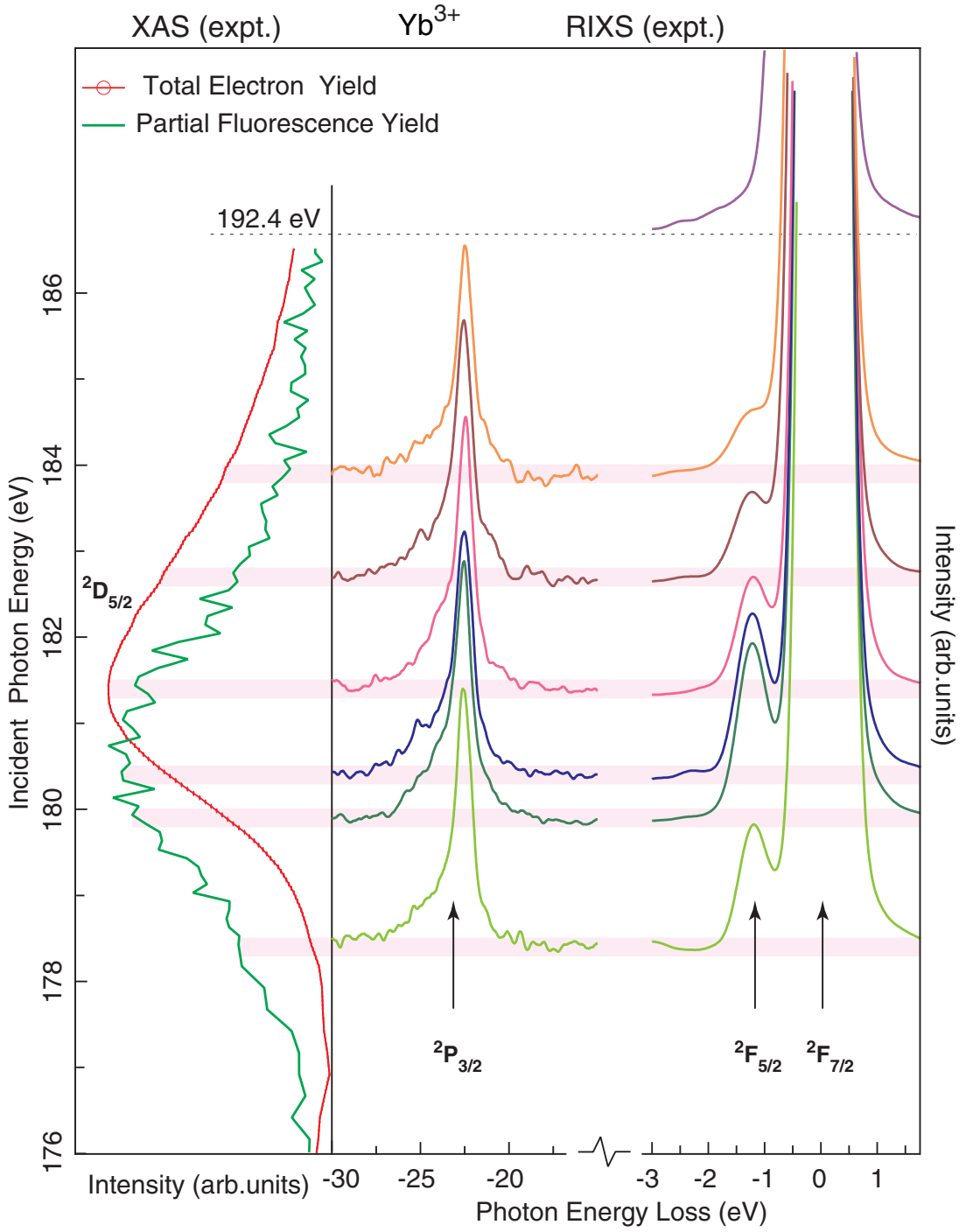

Figure 6.7: RIXS experimental spectra of Yb^{3+} at $N_{4,5}$ resonance. Emission lines at small energy losses are due to $4d^9 5p^6 4f^{14} \rightarrow 4d^{10} 5p^6 4f^{13}$ transitions and at larger energy losses are due to $4d^9 5p^6 4f^{14} \rightarrow 4d^{10} 5p^5 4f^{14}$ transitions.

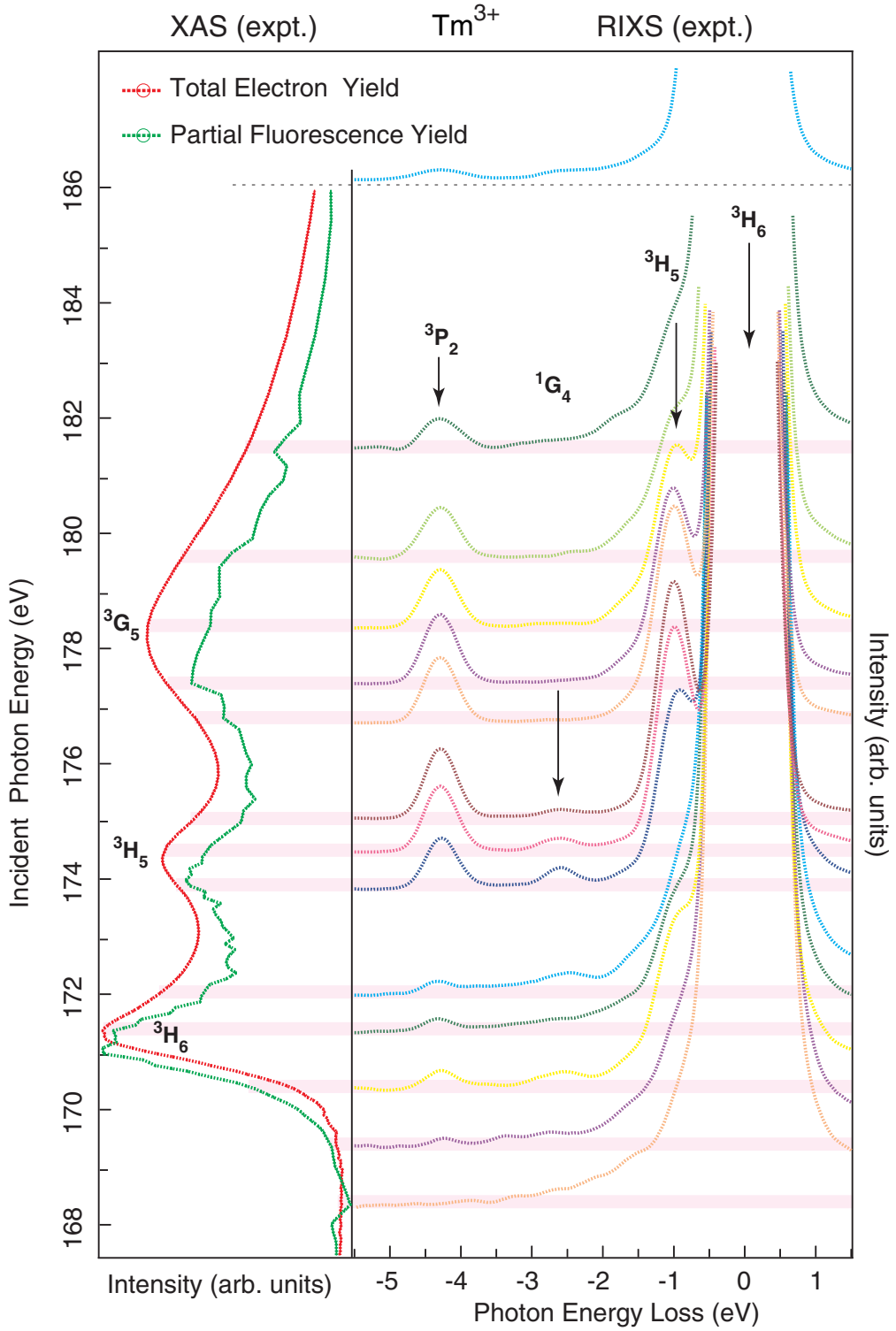

Figure 6.8: RIXS experimental spectra of Tm^{3+} at $N_{4,5}$ threshold. Photon loss features are due to scattering at different final states of $4d^{10}5p^64f^{12}$ configuration due to $4d^95p^64f^{13} \rightarrow 4d^{10}5p^64f^{12}$ transitions.

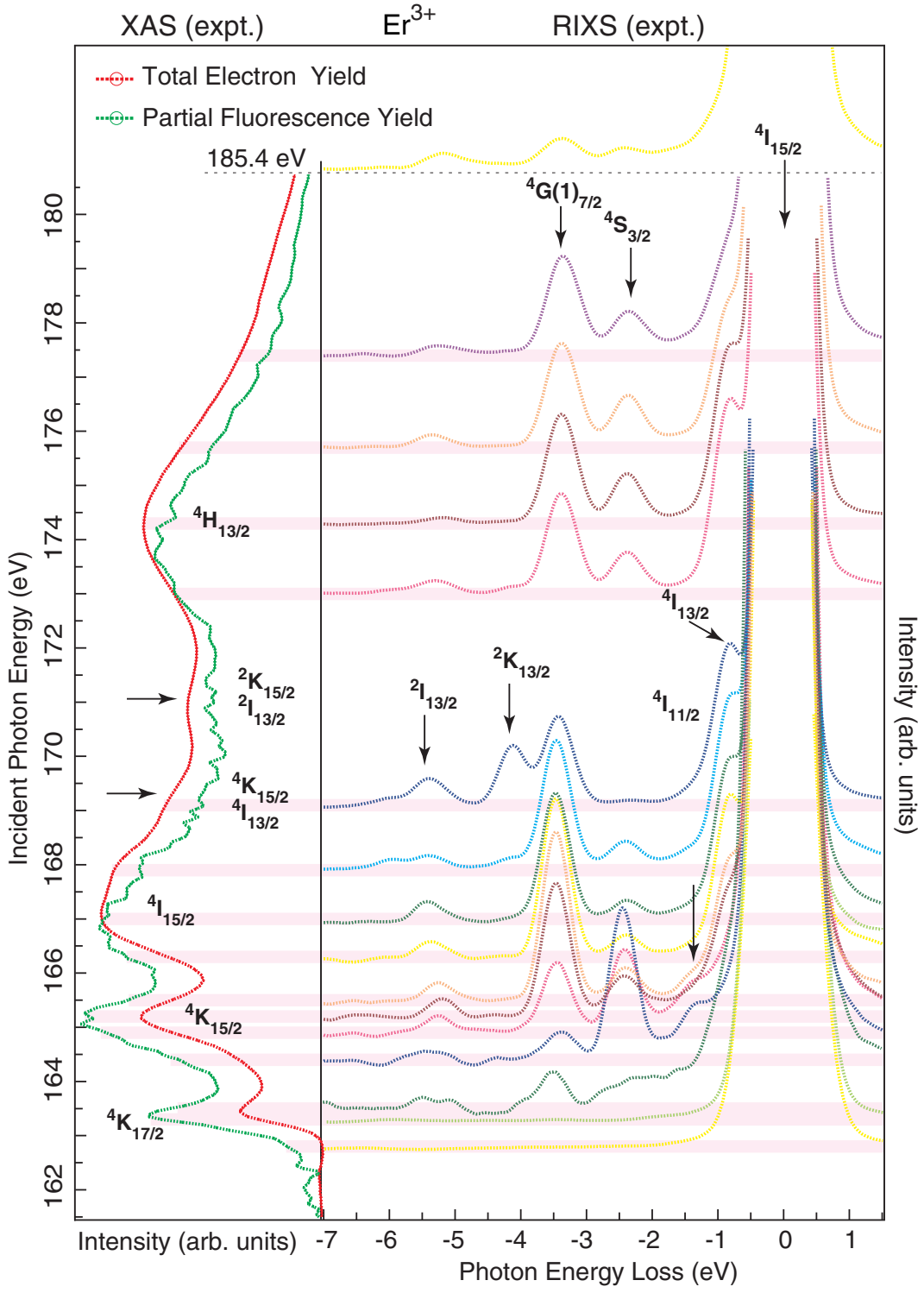

Figure 6.9: RIXS experimental spectra of Er^{3+} at $N_{4,5}$ threshold. Photon loss features are due to scattering at different final states of $4d^{10}5p^64f^{11}$ configuration due to $4d^95p^64f^{12} \rightarrow 4d^{10}5p^64f^{11}$ transitions.

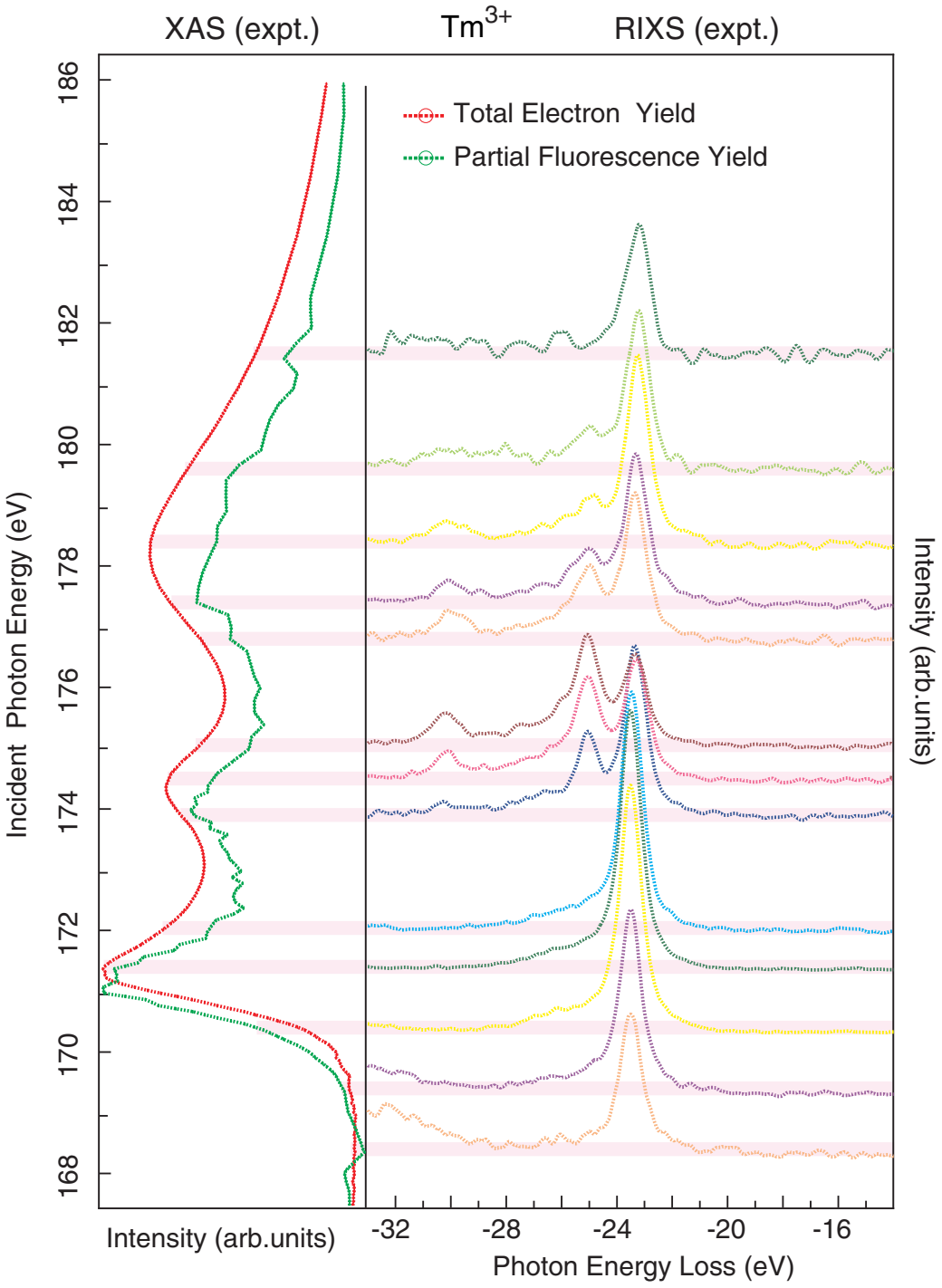

Figure 6.10: RIXS experimental spectra of Tm^{3+} at $N_{4,5}$ threshold. Photon loss features are due to scattering at different final states of $4d^{10}5p^5 4f^{13}$ configuration due to $4d^9 5p^6 4f^{13} \rightarrow 4d^{10}5p^5 4f^{13}$ transitions.

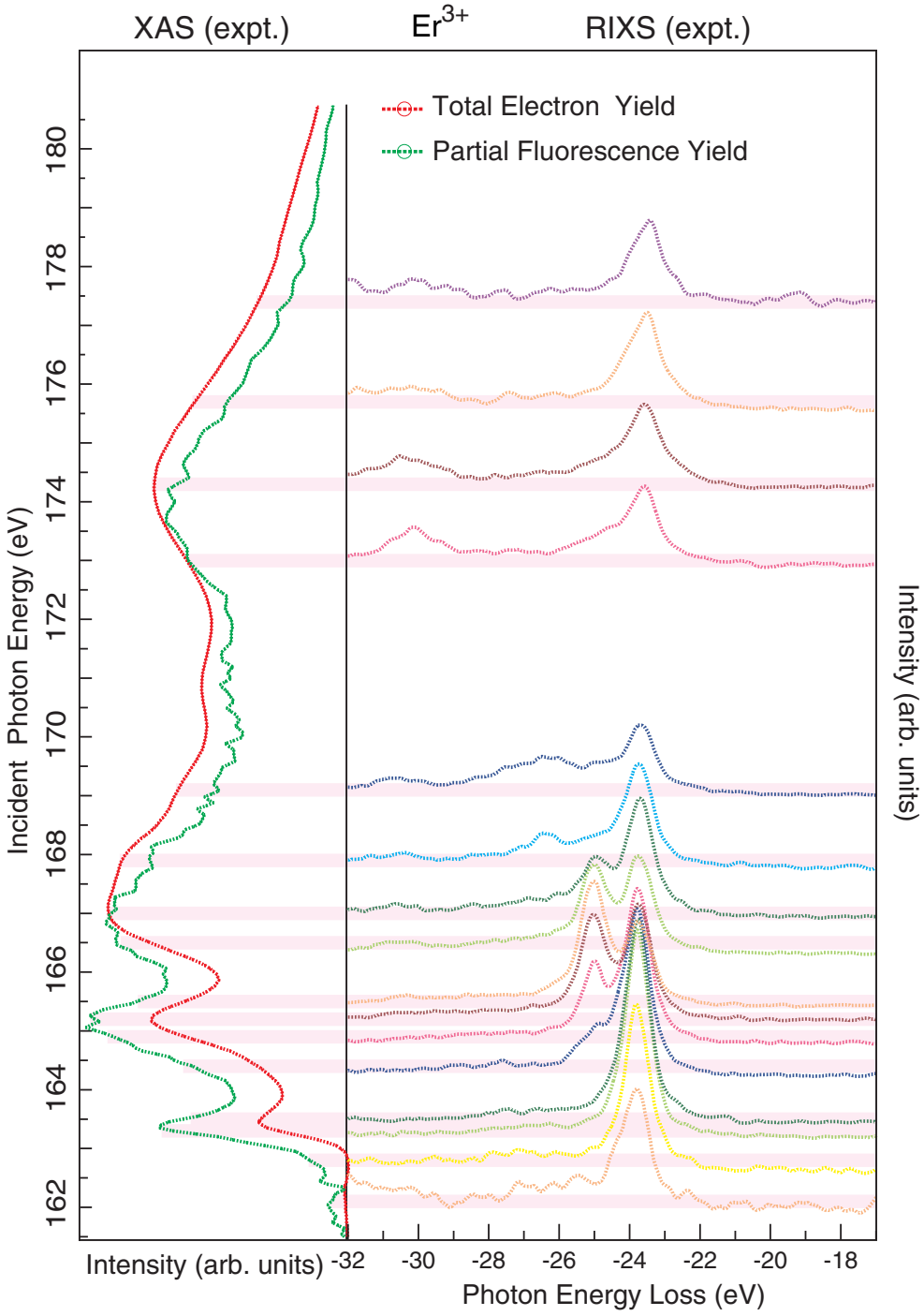

Figure 6.11: RIXS experimental spectra of Er^{3+} at $N_{4,5}$ threshold. Photon loss features are due to scattering at different final states of $4d^{10}5p^5 4f^{12}$ due to $4d^9 5p^6 4f^{12} \rightarrow 4d^{10}5p^5 4f^{12}$ transitions.

Chapter 7

Conclusion and Outlook

The influence of dimensionality of small lanthanide phosphate nanoparticles in their geometric and electronic structure was systematically investigated. The size and morphology of the whole lanthanide nanoparticle series was determined using several methods. A thin film preparation method was established to detect both electrons and photons emitted from the samples, avoiding sample charging on these wide band gap insulators and reducing the self absorption process.

Investigations showed that the clusters possess a long-range order in the geometrical structure proving that they consist of a rigid crystal of nanometer scale. In addition, an absence of short-range order of the atomic arrangements associated with a mixed phase crystal structure in the very small nanoparticles was revealed to be due to their large surface contribution and their ionic radii. Covalency within the phosphate group and lanthanide ion, and the chemical state of each lanthanide ion accessed through oxygen K-edge and M-edge near edge X-ray absorption was systematically investigated. The missing of local order induced spectral broadening, indicating multiple oxygen and lanthanide sites.

We used the well characterized lanthanide nanoparticles to conduct fundamental investigation of strongly electron correlated lanthanide ions. The ideal technique for these studies was chosen resonant inelastic X-ray scattering because it provides atom specific investigations and have an additional degree of selectivity due to stringent symmetry selection rule. We used highly monochromatized incident light of sub-natural width resolution and monitored intensity variation and linear dispersion of RIXS emission lines across the resonances.

In lanthanum ions embedded in phosphate nanoparticles, we carried out detailed studies of many body effects induced from strong electron electron interaction at the $N_{4,5}$ edge. Lanthanum provides the simple case of lanthanides consisting of only two localized resonances and the broad autoionized discrete

state known as giant resonance. The measured $N_{4,5}$ edge X-ray absorption spectra of La displayed different spectral profiles of the pre-resonances in electron and fluorescence yield mode: Electron yield profile was very asymmetric toward a Lorentzian profile of the fluorescence yield. Theoretical calculations revealed the localized pre-resonances to be entangled quantum states due to different symmetry contributions. This activated coherent scattering of different nonradiative decay channels leading to interference effects and strong asymmetrical profiles of electron yield. In the radiative decay, symmetry aspects of dipole transition caused braking of coherence in some of the decay channels that was associated with less interfering channels. In addition, highly symmetry entangled ionic final states played an important role in radiative scattering. All these effects led to a symmetric fluorescence yield profile.

Within the simple case of lanthanum ion we could separate the leverage strength of highly correlated core excited states and the broad giant resonance to interference effects. The calculations showed that the asymmetry induced from lifetime interference (due to broad spectral width of giant resonance) in the spectral profile is very small compared to the one induced from symmetry entangled intermediate states. In the framework of La model the electron correlation in more complex cases of cerium and praseodymium systems was evoked.

Coexistence of linearly dispersed and constant photon energy emission lines upon excitation across giant resonances evidenced configuration interaction of discrete core excited state and continuum states. The application of the core-hole-clock method [85, 86] based on intrinsic time scale; the lifetime of the core excited state, in the photon-in photon-out experiments would give us information on relaxation dynamics and electron transfer times at the giant resonance. This would reveal in addition, the coupling strength of core excited state to the continuum. The track of electron transfer times within the lanthanides would give information on the degree of localization/delocalization of giant resonances across the series. In addition, theoretical calculations of RIXS processes would give information of final ionic states reached, the different competing scattering channels and their coherence across the resonances.

Theoretical calculations have shown that the coupling of discrete autoionized state to the continuum is strongly influenced from the strength of radiation intensity and from the interaction time with the strong radiation field [92]. The ongoing development of Free Electron Laser (FEL) sources of high brilliance and ultra short radiation pulses (20–200fs) provides excellent conditions for these experimental studies. Thus, investigation of coupling degree of giant resonances to

the continuum as a function of radiation field strength and interaction time with resonant inelastic X-ray scattering technique would be the next milestone.

Comments on my contribution

This thesis comprehend a combination of experimental and theoretical work. Both, experimental and theoretical work was performed in a research team with my substantial contribution. Synthesis and characterization of the nanoparticles were carried out, with my participation and Kerstin Rücker, at Inorganic chemistry department, Osnabrück University and at Physical chemistry department, Hamburg University. The thin film preparation method was established by Annette Pietzsch. The load lock sample exchange system, to keep nanoparticle samples in vacuum and transfer them to experimental chamber was designed and constructed by me. I have played a central role in preparation and realization of XAS and RIXS experiments presented here. The XAS and RIXS calculations were done by me in close cooperation with Inorganic chemistry department at Utrecht University. RPES calculations were performed by Frank de Groot. I have only included papers in this thesis where I have contributed essentially in the experimental work, analysis, interpretation and writing.

Acknowledgments

The PhD work is an evolution process of personal and scientific skills influenced by many people. I would like to thank everyone who contributed to this process and made my time as a doctoral student worth remembering. Two of them I would like to thank prominently:

Wilfried Wurth who accepted me to join his research group under his supervision and gave me the opportunity to work at excellent research facilities. I am grateful for his continuous scientific support during my PhD work and his admirable patience.

Alexander Föhlisch who has been the closer advisor of my scientific work. I am very grateful to have had the chance to work closely with him and profit from his knowledge, experience and innovative ideas.

I would also like to thank our external collaborators Markus Haase and Frank de Groot for their scientific engagement in my research project: Markus for offering me the chance to use his lab facilities and give me insights on chemical synthesis of nanoparticles. Frank for encouraging and helping me with atomic calculations. Without his contribution this thesis would have looked differently.

I would like to thank Michael Martins for the innumerable discussions on atomic physics and Bernd Sonntag for his contribution on unraveling the different aspects of electron correlation in lanthanides.

I am very grateful to the former and present members of the Wurth-group. With many of them I had the pleasure to work together and exchange ideas: Annette, Mitsuru, Franz, Vijayalakshmi, Martin B., Martin D., Bill, Torben, Flo and Urs. Especially, I thank Annette Pietzsch and Mitsuru Nagasono for sharing together innumerable beam shifts at synchrotron facilities.

I thank Holger and Sven for their assistance in the various vacuum technical problems with HIXSS machine.

I thank all the other group members Greta, Michael, Leif, Steffen, Paolo, Jon and Sebastian for the pleasant time I had at lunch discussions and at our group parties.

Special thanks goes to Marlies Fölck “the heart of the Wurth-group” for being so nice, kind and always helpful to me.

Finally, I would like to thank my parents, Dritan, Eri, Ilir, Riku for their ongoing support during my life abroad, and my close friends, Olga, Eszty, Leo, Liza, Alexa, Isa, Melanie, Shiraz, Joana, Ana Maria and Julia, for making so pleasant my life in Hamburg.

Edlira Suljoti, Hamburg, October 2008

List of papers

Strong electron correlation involves the decay processes of La 4d resonances.
E. Suljoti, A. Föhlisch, F.M.F. de Groot, M. Nagasono, P. Glatzel, F. Hennies, M. Deppe, A. Pietzsch, and W. Wurth.
to be submitted to Phys. Rev. Lett.

Geometric and electronic structure of lanthanide orthophosphate nanoparticles determined with X-rays.
E. Suljoti, M. Nagasono, A. Pietzch, K. Hickmann, M. Haase, W. Wurth, and A. Föhlisch.
Journal of Chem. Phys, **127**, 134706, (2008).

Measurement of shell thickness in CdSe/CdS nanoparticles with X-ray absorption spectroscopy.
A. Pietzsch, E. Suljoti, M. Nagasono, A. Föhlisch, W. Wurth.
J. Electron. Spectrosc. Relat. Phenom., **166-167**, 81, (2008).

Correlation and many body aspects of electron dynamics.
E. Suljoti, A. Föhlisch, F.M.F. de Groot, M. Nagasono, and W. Wurth.
in manuscript.

Towards time resolved core level photoelectron spectroscopy with femtosecond X-ray free-electron lasers.
A. Pietzsch, A. Föhlisch, M. Beye, M. Deppe, F. Hennies, M. Nagasono, E. Suljoti, and W. Wurth.
New J. Phys. **10**, 033004, (2008).

Resonant two-photon absorption of extreme-ultraviolet free-electron-laser radiation in helium.
M. Nagasono, E. Suljoti, A. Pietzch, F. Hennies, M. Wellhöfer, J.T. Hoeft, M. Martins, W. Wurth, R. Treusch, J. Feldhaus, J. Schneider, and A. Föhlisch.
Phys. Rev. A Rapid Communications, **75**, 051406(R), (2007).

High-brilliance free-electron-laser photoionization of N2: Ground-state depletion and radiation-field-induced modifications.
A. Föhlisch, M. Nagasono, M. Deppe, E. Suljoti, F. Hennies, A. Pietzch, and W. Wurth.
Phys. Rev. A, **76**, 013411 (2007).

VUV spectroscopy of rare earth doped complex fluoride crystals. M. Kirm, H. Lichtenberg, E. Negodin, E. Suljoti, M. True, G. Zimmerer, V.N. Makhov, N.M. Khaidukov, T.V. Ouvarova.
203rd Electrochemical Society Meeting, Vol. 2003-01.

Inter- and intra-configurational luminescence of Er3+ ions in BaY2F8 under VUV excitation.
M.Kirm, H. Lichtenberg, V. Makhov, E. Negodin, T. Ouvarova, E. Suljoti, M. True and G. Zimmerer.
Radiat. Effects and Defects in Solids, **157**, 911, (2002).

Bibliography

[1] S. Huefner. *Photoelectron Spectroscopy.* Springer, Berlin, 1995.

[2] Joachim Stöhr. *NEXAFS Spectroscopy.* Springer-Verlag, 1992.

[3] C.R. Brundle. The application of electron spectroscopy to surface studies. *J. Vac. Sci. Technol.*, 11(1):212, 1974.

[4] S. Hagström, C. Nordling, and K. Siegbahn. Electron spectroscopy for chemical analysis. *Phys. Lett.*, 9(3):235, 1964.

[5] K. Siegbahn, C. Nordling, A. Fahlman, R. Nordberg, K. Hamrin, J. Hedman, G. Johansson, T. Bergmark, S. Karlsson, I. Lindgren, and B. Lindberg. *ESCA-Atomic, Molecular and Solid State Structure Studied by means of Electron Spectroscopy.* Nort-Holland, Amsterdam, 1966.

[6] K. Siegbahn, C. Nordling, G. Johansson, J. Hedman, P.F. Heden, K. Hamrin, U. Gelius, T. Bergmark, L.O. Werme, R. Manne, and Y. Baer. *ESCA Applied to Free Molecules.* Nort-Holland, Amsterdam, 1969.

[7] John C. Vickerman, editor. *Surface Analysis - The Principal Techniques.* John Wiley and Sons, 1997.

[8] Akio Kotani and Haruhiko Ogasawara. Theory of core-level spectroscopy of rare-earth oxides. *J. Electron Spectrosc. Relat. Phenom.*, 60:257, 1992.

[9] Pierre Auger. Sur l'effet photoelélectrique composé. *J.Phys. Radium*, 6:205, 1925.

[10] G Bradley Armen, Helena Aksela, Teijo Åberg, and Seppo Aksela. The resonant auger effect. *J. Phys. B*, 33:R49, 2000.

[11] Pieter Kuiper, J.H. Guo, Conny Såthe, L.C. Duda, Joseph Nordgren, J.J.M. Pothuizen, F.M.F. de Groot, and G.A. Sawatzky. Resonant x-ray raman spectra of cu dd excitations in $sr_2cuo_2cl_2$. *Phys. Rev. Lett.*, 80(23):5204, 1998.

[12] S.M. Butorin, D.C. Mancini, J.H. Guo, N. Wassdahl, J. Nordgren, M. Nakazava, S. Tanaka, T. Uozumi, A. Kotani, Y. Ma, K.E. Myano, B.A. Karlin, and D.K. Shuh. Resonant x-ray fluorescence spectroscopy of correlated systems: A probe of charge-transfer excitations. *Phys. Rev. Lett.*, 77(3):574, 1996.

[13] J. Kawai. *Absorption techniques in X-ray spectrometry in Encyclopedia of Analytical Chemistry.* Wiley, Chichester, 2000.

[14] Heike Meyssamy and Karsten Riwotzki. Wet-chemical synthesis of doped colloidal nanomaterials: particles and fibers of $lapo_4$:eu, $lapo_4$:ce and $lapo_4$:ce,tb. *Adv. Mater.*, 11(10):840, 1999.

[15] K. Riwotzki, H. Meyssamy, A. Kornowski, and M. Haase. Liquid-phase synthesis of doped nanoparticles: Colloids of luminescing $lapo_4 : eu$ and $cepo_{4:Tb}$ particles with a narrow particle size distribution. *J.Phys. Chem. B*, 104:2824, 2000.

[16] O. Lehmann, H. Meyssamy, K. Kömpe, H. Schnablegger, and M. Haase. Synthesis, growth and er^{3+} luminescence of lanthanide phosphate nanoparticles. *J.Phys. Chem. B*, 107:7449, 2003.

[17] J.M.C. Thornton and R.H. Williams. An s/xps study of hydrogen terminated, ordered silicon (100) and (111) surfaces prepared by chemical etching. *Physica Scripta*, 41:1047, 1990.

[18] P. Dumas, Y.J. Chabal, and P. Jakob. Morphology of hydrogen-terminated si(111) and si(100) surfaces upon etching in hf and buffered-hfsolutions. *Surface Science*, 269/270:867, 1992.

[19] Robert D. Cowan. *The theory of atomic structure and spectra.* University of California Press, 1981.

[20] F.M.F. de Groot. X-ray absorption and dichroism of transition metals and their compounds. *J. Electron Spectrosc. Relat. Phenom.*, 67:529, 1994.

[21] B. T. Thole, R. D. Cowan, G. A. Sawatzky, J. Fink, and J. C. Fuggle. New probe for the electronic state ground-structure of narrow-band and impurity systems. *Phys. Rev. B*, 31(10):6856, 1985.

[22] Frank M.F. de Groot. Ligand and metal x-ray absorption in transition metal complexes. *Inorg. Chim. Acta*, 361:850, 2008.

[23] R. Manne and T. Aberg. Koopmans' theorem for inner-shell ionization. *Chem. Phys. Lett.*, 7(2):282, 1970.

[24] Frank de Groot. Multiplet effects in x-ray spectroscopy. *Coord. Chem. Rev.*, 249: 31, 2005.

[25] Ulf von Barth and Günter Grossmann. Dynamical effects in x-ray spectra and the final state rule. *Phys. Rev. B*, 25(8):5150, 1982.

[26] P. Hohenberg and W. Kohn. Inhomogeneous electron gas. *Phys. Rev.*, 136(3): B864, 1964.

[27] W. Kohn and L.J. Sham. Self-consistent equations including exchange and correlation effects. *Phys. Rev.*, 140(4).

[28] Frank de Groot and Akio Kotani. *Core level spectroscopy of solids*. Taylor, Francis, 2008.

[29] Frank de Groot. High-resolution x-ray emission and x-ray absorption spectroscopy. 101(6):1779, 2001.

[30] U. Fano. Effects of configuration interaction on intensities and phase shifts. *Phys. Rev.*, 124(6):1866, 1961.

[31] Faris Gel'mukhanov and Hans Ågren. Resonant x-ray raman scattering. *Phys. Rep.*, 312:87, 1999.

[32] Jan-Erik Rubensson. Rixs dynamics for beginners. *J. Electron Spectrosc. Relat. Phenom.*, 110-111:135, 2000.

[33] Frederick H. Mies. Configuration interaction theory. effects of overlapping resonances. *Phys. Rev.*, 175(1):164, 1968.

[34] Philip Moriarty. Nanostructured materials. *Rep. Prog. Phys.*, 64:297, 2001.

[35] A. P. Alivisatos. Semiconducter clusters, nanocrystals, and quantum dots. *Science*, 271:933, 1996.

[36] Stephan Heer, Olaf Lehmann, Markus Haase, and Hans-Ulrich Güdel. Blue, green and red upconversion emission from lanthanide-doped $lupo_4$ and $ybpo_4$ nanocrystals in a transparent colloidal solution. *Angw. Chem. International Edition*, 42(27):3179, 2003.

[37] Gerald A. Hebbink, Jan W. Stouwdam, David N. Reinhoudt, and Frank C.J.M. van Veggel. Lanthanide (iii)-doped nanoparticles that emit in the near-infrared. *Adv. Mater.*, 14(16):1147, 2002.

[38] Yan Ruoxue, Sun Xiaoming, Wang Xun, Peng Qing, and Li Yadong. Crystal structures, anisotropic growth, and optical properties: Controlled synthesis of lanthanide orthophosphate one-dimensional nanomaterials. *Chemistry Eur. J.*, 11:2183, 2005.

[39] Yue-Ping Fang, An-Wu Xu, Rui-Qi Song, Hua-Xin Zhang und Li-Ping You, Jimmy C. Yu, and Han-Qin Liu. Systematic synthesis and characterization of single-crystal lanthanide orthophosphate nanowires. *J. Am. Chem. Soc.*, 125: 16025, 2003.

[40] J.C. Nipko, C.-K. Loong, M. Loewenhaupt, M. Braden, W. Reichardt, and L. A. Boatner. Lattice dynamics of xenotime: The phonon dispersion relations and density of states of $lupo_4$. *Phys. Rev. B*, 56:11584, 1997.

[41] Xiaogang Peng, Liberato Manna, Weidong Yang, Juanita Wickham, Erik Scher, Andreas Kadavanich, and A.P. Alivisatos. Shape control of cdse nanocrystals. *Nature (London)*, 404:59, 2000.

[42] Ya-Wen Zhang, Zheng-Guang Yan, Li-Ping You, Rui Si, and Chun-Hua Yan. General synthesis and characterization of monocrystalline lanthanide orthophosphates nanowires. *Eur. J. Inorg. Chem*, 2003:4099, 2003.

[43] G. Stryganyuk, D.M. Trots, A. Voloshinovski, T. Shalapska, V. Zakordonskiy, V. Vistovskyy, M. Pidzyrailo, and G. Zimmerer. Luminescence of ce^{3+} doped $lapo_4$ nanophosphors upon ce^{3+} 4f-5d and band-to-band excitation. *J. Lumin.*, 128(3), 2008.

[44] Olaf Lehman, Karsten Kömpe, and Markus Haase. Synthesis of eu^{3+}-doped core and core/shell nanoparticles and direct spectroscopic identification of dopant sites at the surface and in the interior of the particles. *J. Am. Chem. Soc.*, 126: 14935, 2004.

[45] Karsten Kömpe, Olaf Lehmann, and Markus Haase. Spectroscopic distinction of surface and volume ions in ceriumm(iii)- and terbium(iii)-containing core and core/shell nanoparticles. *Chem. Mater.*, 18:4442, 2006.

[46] I.M. Lifshitz and V.V. Slyozov. The kinetics of precipitation from supersaturated solid solutions. *J. Phys. Chem. Solids*, 19:35, 1961.

[47] C.B. Murray, D.J. Norris, and M.G.Bawendi. Synthesis and characterization of nearly monodisperse cde (e=s, se, te) semiconducter nanocrystallites. *J. Am. Chem. Soc.*, 115:8706, 1993.

[48] Michael Knapp, Carsten Baehtz, Helmut Ehrenberg, and Hartmut Fuess. The synchrotron powder diffractometer at beamline b2 at hasylab/desy: status and capabilities. *J. Synchrotron Rad.*, 11:328, 2004.

[49] T. Roisnel and J. Rodriquez-Carvajal. A windows tool for powder diffraction pattern analysis. *Mater. Sci. Forum*, 378/381:118, 2001.

[50] P. Sherrer. *Nachr. Ges. Wiss. Gottingen, Math.-Phys. Kl.*, 2:96, 1918.

[51] S.A. Howard and K.D. Preston. *Modern Powder Diffraction*, volume 20. Mineralogical Society of America, 1989.

[52] Yunxiang Ni, John M. Hughes, and Anthony N. Mariano. Crystal chemistry of the monazite and xenotime structures. *American Mineralogist*, 80:21, 1995.

[53] B. T. Thole, G. van der Laan, J. C. Fuggle, G. A. Sawatzky, R. C. Karnatak, and J.-M.Esteva. $3d$ x-ray-absorption lines and the $3d^9 4f^{n+1}$ multiplets of the lanthanides. *Phys. Rev. B*, 32:5107, 1985.

[54] G. Kaindl, G. Kalkovski, W. D. Brewer, B. Perscheid, and F. Holtzberg. M-edge x-ray absorption spectroscopy of 4f instabilities in rare-earth systems (invited). *J. Appl. Phys.*, 55:1910, 1984.

[55] B. T. Thole and G. van der Laan. Systematics of the relation between spin-orbit splitting in the valence band and the branching ratio in x-ray absorption spectra. *Europhysics Letters*, 4(9):1083, 1987.

[56] B. T. Thole. Branching ratio in x-ray absorption spectroscopy. *Phys. Rev. B*, 38: 3158, 1988.

[57] S.O. Kucheyev, C. Bostedt, T. van Buuren, T.M. Willey, T.A. Land, L.J. Terminello, T.E. Felter, A.V. Hamza, and S.G. Demos. Electronic structure of $kd_{2x}h_{2(1-x)}po_4$ studied by soft x-ray absorption and emission spectrocopies. *Phys. Rev. B*, 70:245106, 2004.

[58] Zheshuai Lin, Zhizhong Wang, Chungtian Chen, and Ming-Hsein Lee. Mechanism of linear and nonlinear optical effects of kdp and urea crystals. *J. Chem. Phys.*, 118(5):2349, 2003.

[59] M.G. Willinger, D.S. Su, and R. Schlögl. Electronic structure of $\beta - vopo_4$. *Phys. Rev. B*, 71:15518, 2005.

[60] M. Grioni, M.T. Czyzyk, F.M.F. de Groot, J.C. Fuggle, and B.E. Watts. Unoccupied electronic states of cuo: An oxygen 1s x-ray absorption spectroscopy investigation. *Phys. Rev. B*, 39(3):4886, 1989.

[61] F.M.F. de Groot, M. Grioni, J.C. Fuggle, J. Ghijsen, G.A. Sawatzky, and H. Petersen. Oxygen 1*s* x-ray absorption edges of transition-metal oxides. *Phys. Rev. B*, 40(8):5715, 1989.

[62] Ziyu Wu, E. Paris, F. Langenhorst, and F. Seifert. Oxygen-metal bonding in ti-bearing compounds and ab initio full-multiple scattering calculations. *J. Synchrotron Rad.*, 9:394, 2002.

[63] Z.Y. Wu, S. Gota, F. Jollet, M. Pollak, M. Gautier-Soyer, and C.R. Natoli. Characterization of iron oxides by x-ray absorption at the oxygen k edge using a full multiple-scattering approach. *Phys. Rev. B*, 55:2570, 1997.

[64] U. Fano and J.W. Cooper. Line profiles in the far-uv absorption spectra of rare gases. *Phys. Rev. A*, 137(5):1364, 1965.

[65] U. Fano and J.W. Cooper. Spectral distribution of atomic oscillator strength. *Rev. Mod. Phys.*, 40(3):441, 1968.

[66] V. Schmidt. Photoionizations of atoms using synchrotron radiation. *Rep. Prog. Phys.*, 55:1483, 1992.

[67] E.W.B. Dias, H.S. Chakraborty, P.C. Deshmukh, S.T. Manson, O. Hemmers, P. Glans, D.L. Hansen, H. Wang, S.B. Whitfield, D.W. Lindle, R.Wehlitz, J.C. Levin, I.A. Sellin, and R.C.C. Perera. Breakdown of the independent particle approximation in high-energy photoionization. *Phys. Rev. Lett.*, 78(24):4553, 1997.

[68] M.Ya. Amusia, N.B. Avdonina, E.G. Drukarev, S.T. Manson, and R.H. Pratt. Qualitative modification of the high energy atomic photoionization cross section. *Phys. Rev. Lett.*, 85(22):4703, 2000.

[69] M.Ya. Amusia, L.V. Chernysheva, S.T. Manson, A.M. Msezane, and V. Radojevic. Strong electron correlation in phottoionization of spin-orbit doublets. *Phys. Rev. Lett.*, 88(9):093002, 2002.

[70] M.Ya. Amusia, A.S. Baltenkov, L.V. Chernysheva, Z. Felfli, S.T. Manson, and A.M. Msezane. Effects of spin-orbit activated interchannel coupling on dipole photoelectron angular distribution asymmetry parameters. *J. Phys. B*, 37:937, 2004.

[71] E. Suljoti, M. Nagasono, A. Pietzsch, K. Hickmann, M. Haase, W. Wurth, and A. Föhlisch. Geometric and electronic structure of lanthanide orthophosphate nanoparticles determined with x-rays. *J. Chem. Phys.*, 128:134706, 2008.

[72] M. Aono, T. C. Chiang, J. A. Knapp, T. Tanaka, and D. E. Eastman. Direct recombination and auger deexcitation of la $4d \rightarrow 4f$ resonant excitation in lab_6. *Phys. Rev. B*, 21(7):2661, 1980.

[73] Kouichi Ichikawa, Osamu Aita, and Katsuhito Aoki. Nonradiative decay processes of 4d hole states in csf, baf_2, and laf_3. *Phys. Rev. B*, 45(7):3221, 1992.

[74] H. Ogasawara, A. Kotani, B. T. Thole, K. Ichikawa, O. Aita, and M. Kamada. La $5p$ core photoemission spectra at the $4d \rightarrow 4f$ resonance in laf_3. *Solid State Communications*, 81(8):645, 1992.

[75] S. R. Mishra, T. R. Cummins, G. D. Waddill, W. J. Gammon, G. van der Laan, K. W. Goodman, and J. G. Tobin. Nature of resonant photoemission in gd. *Phys. Rev. Lett.*, 81(6):1306, 1998.

[76] Göran Wendin. Giant dipole resonance in 4d photoabsorption of atomic barium. *Phys. Lett. A*, 46(2):119, 1973.

[77] M.Ya. Amusia and S.I. Sheftel. Calculation of the photoionization cross section of the $4d^{10}$ subshell of the la atom. *Phys. Rev. A*, 55(8):469, 1976.

[78] Jean-Patrick Connerade. *Highly excited atoms*. Cambridge University Press, 1998.

[79] J. L. Dehmer, A. F. Starace, U. Fano, J. Sugar, and J. W. Cooper. Raising of discrete levels into the far continuum. *Phys. Rev. Lett.*, 26(25):1521, 1971.

[80] Jack Sugar. Potential-barrier effects in photoabsorption. ii. interpretation of photoabsorption resonances in lanthanide metals at the $4d$-electron threshold. *Phys. Rev. B*, 5(5):1785, 1972.

[81] U. Köble, L. Kiernan, J.T. Costello, J-P. Mosnier, E.T. Kennedy, V.K. Ivanov, V.A. Kupchenko, and M.S. Shendrik. $4f(^1p)$ giant dipole resonance in la^{3+}. *Phys. Rev. Lett.*, 74(12).

[82] C. G. Olson and D.W. Lynch. Rare-earth $4d$ absorption spectra in rare-earth trifluorides. *J. Opt. Soc. Am.*, 71(1):88, 1982.

[83] Shoji Suzuki, Takehiko Ishii, and Takasi Sagawa. 4d-shell photoabsorption spectra of lanthanum-and cerium-halides. *J. Phys. Soc. Jpn.*, 38(1), 1975.

[84] M. Richter, M. Meyer, M. Pahler, T. Prescher, E.v. Raven, B. Sonntag, and H.E. Wetzel. Experimental study of atomic $4d$ giant resonances by photoabsorption and photoelectron spectroscopy: Ba, la and ce. *Phys. Rev. A*, 39(11):5666, 1989.

[85] O. Björneholm, A. Nilsson, A. Sandell, B. Hernnäs, and N. Martensson. Determination of time scales for charge transfer screening in physisorbed molecules. *Phys. Rev. Lett.*, 68(12):1892, 1992.

[86] P.A. Brühwiler, O. Karis, and N. Martensson. Charge-transfer dynamics studied using resonant core spectroscopies. *Rev. Mod. Phys.*, 74:703, 2002.

[87] M. Richter, M. Meyer, M. Pahler, T. Prescher, E.v. Raven, B. Sonntag, and H.E. Wetzel. Experimental study of atomic $4d$ giant resonances by photoabsorption and photoelectron spectroscopy: Sm, eu and gd. *Phys. Rev. A*, 40(12):7007, 1989.

[88] Ch. Dzionk, W. Fiedler, M.v. Lucke, and P. Zimmerman. Photoion spectroscopy in the $4d$ giant resonances of the lanthanides. *Phys. Rev. Lett.*, 62:878, 1989.

[89] Haruhiko Ogasawara and Akio Kotani. Calculation of rare-earth 4d giant absorption spectra with multiplet effects and decay processes. *J. Synchrotron Rad.*, 8:220, 2001.

[90] Edlira Suljoti. Electronic relaxation of er^{3+} $5d$ excitations in different fluoride matrices. Master's thesis, Hamburg University, 2002.

[91] Markus True. *Fine structure in $d-f$ and $f-f$ transitions of Tm^{3+} and systematic investigations of $3d^5-3d^4 4s$ absorption of Mn^{2+} doped fluorides.* PhD thesis, Hamburg University, 2004.

[92] P. Lambropoulos and P. Zoller. Autoionizing states in strong laser fields. *Phys. Rev. A*, 24(1):24, 1981.